Probabilistic approach for the separation of the acoustic and aerodynamic wall pressure fluctuations

Alice Dinsenmeyer

N°d'ordre NNT : 2020LYSEI087

THESE de DOCTORAT DE L'UNIVERSITE DE LYON
opérée au sein de
l'Institut National des Sciences Appliquées de Lyon

Ecole Doctorale N° 162
Mécanique, énergétique, Génie Civil, Acoustique

Spécialité : Acoustique

Soutenue publiquement le 12/10/2020, par:
Alice Dinsenmeyer

Probabilistic approach for the separation of the acoustic and aerodynamic wall pressure fluctuations

---

Devant le jury composé de :

Gabart, Gwénaël	Professeur, Le Mans Université	Président
Valeau, Vincent	Professeur, Université de Poitiers	Rapporteur
Pézerat, Charles	Professeur, Le Mans Université	Rapporteur
Lopez Arteaga, Ines	Professeur, Eindhoven University of Technology	Examinatrice
Piot, Estelle	HdR, ONERA	Examinatrice
Gabart, Gwénaël	Professeur, Le Mans Université	Examinateur
Antoni, Jérôme	Professeur, INSA Lyon	Directeur de thèse
Bailly, Christophe	Professeur, École Centrale de Lyon	Co-encadrant
Leclère, Quentin	Maître de Conférences HdR, INSA Lyon	Co-encadrant
Julliard, Emmanuel	Docteur, Airbus	Invité
Sijtsma, Pieter	Docteur, PSA3	Invité
Picard, Christophe	Docteur, MicrodB	Invité

Printed on December 17, 2020

Département FEDORA – INSA Lyon - Ecoles Doctorales – Quinquennal 2016-2020

SIGLE	ECOLE DOCTORALE	NOM ET COORDONNEES DU RESPONSABLE
CHIMIE	**CHIMIE DE LYON** http://www.edchimie-lyon.fr Sec. : Renée EL MELHEM Bât. Blaise PASCAL, 3e étage secretariat@edchimie-lyon.fr INSA : R. GOURDON	**M. Stéphane DANIELE** Institut de recherches sur la catalyse et l'environnement de Lyon IRCELYON-UMR 5256 Équipe CDFA 2 Avenue Albert EINSTEIN 69 626 Villeurbanne CEDEX directeur@edchimie-lyon.fr
E.E.A.	**ÉLECTRONIQUE, ÉLECTROTECHNIQUE, AUTOMATIQUE** http://edeea.ec-lyon.fr Sec. : M.C. HAVGOUDOUKIAN ecole-doctorale.eea@ec-lyon.fr	**M. Gérard SCORLETTI** École Centrale de Lyon 36 Avenue Guy DE COLLONGUE 69 134 Écully Tél : 04.72.18.60.97 Fax 04.78.43.37.17 gerard.scorletti@ec-lyon.fr
E2M2	**ÉVOLUTION, ÉCOSYSTÈME, MICROBIOLOGIE, MODÉLISATION** http://e2m2.universite-lyon.fr Sec. : Sylvie ROBERJOT Bât. Atrium, UCB Lyon 1 Tél : 04.72.44.83.62 INSA : H. CHARLES secretariat.e2m2@univ-lyon1.fr	**M. Philippe NORMAND** UMR 5557 Lab. d'Ecologie Microbienne Université Claude Bernard Lyon 1 Bâtiment Mendel 43, boulevard du 11 Novembre 1918 69 622 Villeurbanne CEDEX philippe.normand@univ-lyon1.fr
EDISS	**INTERDISCIPLINAIRE SCIENCES-SANTÉ** http://www.ediss-lyon.fr Sec. : Sylvie ROBERJOT Bât. Atrium, UCB Lyon 1 Tél : 04.72.44.83.62 INSA : M. LAGARDE secretariat.ediss@univ-lyon1.fr	**Mme Sylvie RICARD-BLUM** Institut de Chimie et Biochimie Moléculaires et Supramoléculaires (ICBMS) - UMR 5246 CNRS - Université Lyon 1 Bâtiment Curien - 3ème étage Nord 43 Boulevard du 11 novembre 1918 69622 Villeurbanne Cedex Tel : +33(0)4 72 44 82 32 sylvie.ricard-blum@univ-lyon1.fr
INFOMATHS	**INFORMATIQUE ET MATHÉMATIQUES** http://edinfomaths.universite-lyon.fr Sec. : Renée EL MELHEM Bât. Blaise PASCAL, 3e étage Tél : 04.72.43.80.46 infomaths@univ-lyon1.fr	**M. Hamamache KHEDDOUCI** Bât. Nautibus 43, Boulevard du 11 novembre 1918 69 622 Villeurbanne Cedex France Tel : 04.72.44.83.69 hamamache.kheddouci@univ-lyon1.fr
Matériaux	**MATÉRIAUX DE LYON** http://ed34.universite-lyon.fr Sec. : Stéphanie CAUVIN Tél : 04.72.43.71.70 Bât. Direction ed.materiaux@insa-lyon.fr	**M. Jean-Yves BUFFIÈRE** INSA de Lyon MATEIS - Bât. Saint-Exupéry 7 Avenue Jean CAPELLE 69 621 Villeurbanne CEDEX Tél : 04.72.43.71.70 Fax : 04.72.43.85.28 jean-yves.buffiere@insa-lyon.fr
MEGA	**MÉCANIQUE, ÉNERGÉTIQUE, GÉNIE CIVIL, ACOUSTIQUE** http://edmega.universite-lyon.fr Sec. : Stéphanie CAUVIN Tél : 04.72.43.71.70 Bât. Direction mega@insa-lyon.fr	**M. Jocelyn BONJOUR** INSA de Lyon Laboratoire CETHIL Bâtiment Sadi-Carnot 9, rue de la Physique 69 621 Villeurbanne CEDEX jocelyn.bonjour@insa-lyon.fr
ScSo	**ScSo*** http://ed483.univ-lyon2.fr Sec. : Véronique GUICHARD INSA : J.Y. TOUSSAINT Tél : 04.78.69.72.76 veronique.cervantes@univ-lyon2.fr	**M. Christian MONTES** Université Lyon 2 86 Rue Pasteur 69 365 Lyon CEDEX 07 christian.montes@univ-lyon2.fr

*ScSo : Histoire, Géographie, Aménagement, Urbanisme, Archéologie, Science politique, Sociologie, Anthropologie

Remerciements

Cette thèse s'est déroulée de juillet 2017 à juillet 2020, au sein du Laboratoire Vibrations et Acoustique de l'INSA de Lyon et du groupe Acoustique du Laboratoire de Mécanique des Fluides et d'Acoustique de l'École Centrale de Lyon.

Je souhaite en premier lieu remercier mes directeur et encadrants Jérôme Antoni, Quentin Leclère et Christophe Bailly pour m'avoir patiemment guidée au cours de ce long travail. Ce fut un plaisir de pouvoir bénéficier de leur expertise et de leur rigueur.

Je remercie également les rapporteurs et examinateurs qui ont évalué ce travail.

J'ai eu la chance d'évoluer au sein du projet ADAPT, dont les membres ont contribué à enrichir cette thèse. Je remercie particulièrement Christophe Picard pour la coordination du projet et nos divers échanges, Pieter Sijtsma pour son regard critique, Edouard Salze pour son aide lors des mesures en soufflerie effectuées au LMFA, Emmanuel Julliard pour son éclairage sur la réalité industrielle, ainsi que Thibaut Le Magueresse, Simon Bouley et Arthur Finez qui ont également suivi ce projet avec attention.

Je remercie tous les permanents, doctorants, post-doctorants et stagiaires avec qui j'ai pu partager la vie de labo, aussi bien au LVA qu'au LMFA.

Enfin, je remercie mes proches, amis et famille, en particulier Thomas, qui m'a soutenue de puis nos débuts en acoustique jusqu'à cette longue période de rédaction si particulière dite du "Premier Confinement de Printemps 2020".

Abstract

With the emergence of MEMS and the overall decrease in the cost of sensors, the acquisitions multichannel are becoming more widespread, particularly in the field of acoustic source identification. The quality of source localization and quantification can be degraded by the presence of ambient or electronic noise. In particular, in the case of in flow measurements, the turbulent boundary layer that develops over the measuring system can induce pressure fluctuations that are much greater than those of acoustic sources. It then becomes necessary to process the acquisitions to extract each component of the measured field. For this purpose, it is proposed in this thesis to decompose the measured spectral matrix into the sum of a matrix associated with the acoustic contribution and a matrix for aerodynamic noise. This decomposition exploits the statistical properties of each pressure field. Assuming that the acoustic contribution is highly correlated on the sensors, the rank of the corresponding cross-spectral matrix is limited to the number of equivalent uncorrelated sources. Concerning the aerodynamic noise matrix, two statistical models are proposed. A first model assumes a totally uncorrelated field on the sensors, and a second is based on a pre-existing physical model. This separation problem is solved by a Bayesian optimization approach, which takes into account the uncertainties on each component of the model. The performance of this method is first evaluated on wind tunnel measurements and then on particularly noisy industrial measurement, coming from microphones flushmounted on the fuselage of an inflight large aircraft.

Résumé

Avec l'apparition des MEMS et la diminution globale du coût des capteurs, les acquisitions multivoies se généralisent, notamment dans le domaine de l'identification de sources acoustiques. La qualité de la localisation et de la quantification des sources peut être dégradée par la présence de bruit de mesure ambiant ou induit par le système d'acquisition. En particulier, dans le cas de mesures en présence d'un écoulement, la couche limite turbulente qui se développe sur le système de mesure peut induire des fluctuations de pression de niveau bien supérieur à celles des sources acoustiques. Il devient alors nécessaire de traiter les acquisitions pour extraire chaque composante du champ mesuré. Pour cela, on propose de décomposer la matrice spectrale mesurée en la somme d'une matrice associée à la contribution acoustique et d'une matrice pour le bruit aérodynamique. Cette décomposition exploite les propriétés statistiques de chaque champ de pression. En supposant que la contribution acoustique est fortement corrélée sur les capteurs, le rang de la matrice interspectrale associée se limite au nombre de sources décorrélées équivalentes. Concernant la matrice du bruit aérodynamique, deux modèles statistiques sont proposés. Un premier modèle fait l'hypothèse d'un champ totalement décorrélé sur les capteurs, et un second repose sur un modèle physique préexistant. Ce problème de séparation est résolu par une approche d'optimisation bayésienne, qui permet de prendre en compte les incertitudes sur chaque composante du modèle. Les performances de cette méthode sont d'abord évaluées sur des mesures en soufflerie puis sur des données industrielles particulièrement bruitées, provenant de mesures microphoniques effectuées sur le fuselage d'un avion de ligne en vol.

Résumé étendu en français

Financement du projet de thèse

Cette thèse est financée pour moitié par le laboratoire d'excellence Centre Lyonnais d'Acoustique (CeLyA), financé lui-même par le ministère de la recherche français. L'autre moitié du financement provient du projet européen ADvanced Aeroacoustic Processing Techniques (ADAPT), dans le cadre du projet Clean Sky 2. L'objectif général du projet ADAPT est d'améliorer la compréhension des mécanismes de génération du bruit dans le domaine de l'aéronautique, dans un objectif de réduction du bruit émis par les avions.

Introduction

Contexte

L'objectif de ce travail de thèse est de développer des outils de traitement destinés aux mesures multivoies microphoniques pour la caractérisation de sources acoustiques en présence d'écoulement, ce qui peut être le cas pour des mesures en extérieur venté, en milieu sous-marin, en soufflerie ou encore sur des véhicules en mouvement. À la mesure des sources acoustiques s'ajoutent alors les fluctuations des pressions induites par l'écoulement.

On s'intéresse en particulier aux mesures réalisées avec des microphones montés sur panneau rigide, sur lequel une Couche Limite Turbulente (CLT) induite par l'écoulement se développe alors. Le champ de pression induit par les structures tourbillonnaires de la CLT peut être décrit statistiquement et sa description physique est généralement basée sur des hypothèses de stationnarité et d'homogénéité (correspondant à des invariances statistiques en temps et espace), ce qui permet de faire du moyennage temporel et d'étudier les longueurs de corrélation mises en jeu. La longueur de corrélation de la CLT est connue pour décroître rapidement dans l'espace, contrairement à la corrélation du champ acoustique. Cela implique que, pour des antennes dimensionnées pour la localisation de sources, les espacements inter-microphoniques – qui sont de l'ordre de grandeur de la longueur d'onde du champ acoustique – sont bien supérieurs à la longueur de corrélation du champ de la CLT, et ce sur une large gamme fréquentielle.

Par conséquent, ces différences de corrélation peuvent être exploitées pour réaliser une séparation des deux champs. C'est cette approche qui est suivie dans le présent travail, de façon à répondre à l'un des objectifs du projet ADAPT, qui est le

développement d'outils de traitement du signal pour la séparation des contributions acoustique et aérodynamique.

Enjeux de la séparation

L'objectif de la séparation des deux composantes du champ mesuré est double. D'une part, l'étude du champ de la CLT seule est nécessaire pour les études vibro-acoustiques, telles que la prédiction de chargement de structure, du rayonnement à l'intérieur des véhicules ou encore du bruit émis par les canalisations.
D'une autre part, une élimination du bruit de la CLT sur des mesures acoustiques est nécessaire pour une localisation et une quantification correcte des sources. En particulier, dans le domaine de l'aéronautique, il est nécessaire de connaître précisément le niveau de bruit émis par chaque élément d'un avion aux différentes phases de vol, afin de mettre en place des stratégies de réduction de bruit. Ces sources de bruits sont très variées, tonales ou large-bandes, couvrant l'ensemble du domaine fréquentiel de l'audible.

Organisation du manuscrit

Dans ce contexte, il existe déjà quelques stratégies de séparation du champ acoustique et de la contribution CLT. Le premier chapitre du manuscrit présente un état de l'art de ces méthodes de séparation. Pour palier les limites des ces méthodes, une nouvelle méthode de post-traitement est proposée dans le deuxième chapitre, basée sur une hypothèse de bruit CLT décorrélé. Dans le troisième chapitre, la méthode est étendue à une hypothèse de bruit CLT corrélé et enfin, des applications expérimentales des méthodes développées sont proposées dans le quatrième chapitre.

Chapitre 1 : État de l'art sur la séparation du signal et du bruit

Pour les applications d'imagerie acoustique, il est commun de vouloir séparer le signal d'intérêt, qui est celui des sources acoustiques étudiées, et le bruit, constitué de toutes les autres fluctuations de pression. Cette séparation peut être mise en place en amont de la mesure, par des dispositif expérimentaux limitant la présence de bruit. En particulier, quand le bruit est généré par la CLT sur l'antenne de mesure, il est possible de déporter les microphones derrière des cavités ou des tubes, ou bien de les protéger par des écrans. Cependant, ces installations se heurtent à diverses contraintes techniques et ne peuvent pas toujours être mises en place,

par exemple dans le cadre des mesures en vol. De plus, la réduction du bruit CLT qu'elles offrent n'est pas toujours suffisante.

D'autres approches de la littérature proposent un post-traitement des signaux mesurés. Une approche historique est le filtrage en nombres d'ondes, basé sur l'hypothèse que la contribution acoustique et CLT possède un contenu en nombres d'ondes distinct. Cependant, cette méthode nécessite un échantillonnage spatial important et elle montre des limites en basses fréquences ou les contenus en nombres d'ondes se superposent. Les autres méthodes de post-traitement se basent principalement sur une hypothèse de bruit additif totalement décorrélé sur les microphones. Dans ce cas, le bruit est concentré sur les éléments diagonaux de la matrice interspectrale (MI) des mesures. Cette diagonale peut simplement être supprimée, mais cela induit une perte d'information sur l'amplitude des sources acoustiques. Trois méthodes de reconstruction de diagonale sont également décrites dans ce chapitre, mais leurs performances sont limitées, en particulier quand le nombre de sources acoustiques augmente. D'autres méthodes de décomposition matricielle sont également présentées, à savoir l'Analyse en Composantes Principales Robuste (ACPR) ainsi que l'Analyse Canonique des Corrélations (ACC). La limite de l'ACPR est le réglage d'un paramètre de régularisation qui dépend fortement du problème. L'ACC ne permet pas d'identifier une nombre de composantes acoustiques supérieur à la moitié du nombre de microphones. Les performances de ces méthodes sont comparées à celles des méthodes proposées dans les chapitres suivants.

Chapitre 2 : Décomposition de la MI par Analyse Factorielle, pour un bruit décorrélé

Dans ce chapitre, une méthode basée sur une Analyse Factorielle (AF) et sur une hypothèse de bruit totalement décorrélé sur les microphones est proposée. Une adaptation du problème d'AF original est faite pour traiter des données sous la forme d'une MI. Ce problème de décomposition matricielle est posé dans un cadre probabiliste et deux algorithmes de résolution sont proposés. Le premier est l'algorithme d'Espérance-Maximisation, qui est rapide et facile d'implémentation, mais qui présente la limite de ne fournir qu'un optimum local. En effet, des simulations montrent une forte dépendance des résultats à l'initialisation et au choix du nombre de facteurs dans le modèle. Un second algorithme d'optimisation globale est donc proposé, reposant sur un formalisme bayésien. Des distributions *a priori* sont choisies pour chaque inconnue du modèle d'AF. Assez classiquement,

chaque paramètre est modélisé par une gaussienne dont la variance suit elle-même une loi inverse-gamma.

La parcimonie du modèle est renforcée pour permettre une meilleure régularisation du problème inverse. Pour cela, les facteurs sont pondérés à l'aide de coefficient distribués selon une loi de Bernoulli, souvent utilisé pour forcer la parcimonie des solutions. Le problème est ensuite résolu à l'aide d'un échantillonneur de Gibbs (une méthode de Monte Carlo par chaine de Markov, MCMC) et une accélération par la marginalisation des facteurs lors de l'échantillonnage des poids. Diverses illustrations sur un cas numérique sont données, montrant des niveaux de spectres acoustiques reconstruits par l'AF résolu avec les MCMC meilleurs que ceux fournit par les méthodes de la littérature. Les contraintes de cette méthode MCMC sont les développements mathématiques des postérieures de chaque paramètre, ainsi que les temps de calcul nécessaires.

Chapitre 3 : Identification d'une contribution CLT corrélée

Le problème d'AF est ensuite étendu pour prendre en compte un bruit de CLT corrélé, afin de réaliser une séparation satisfaisante dans les basses fréquences où l'hypothèse de CLT décorrélée n'est plus respectée. Le modèle de corrélation utilisé est une décroissance exponentielle comme proposé par G. M. Corcos en 1963. Ce modèle de CLT comprend trois paramètres (vitesse de convection et taux de décroissance longitudinal et transversal). Ces paramètres peuvent être déterminés par régression sur les données avant d'appliquer l'algorithme de séparation. Une autre approche est également proposée, où ces paramètres sont inférés au sein du processus de séparation. Pour cela, un algorithme de Metropolis-Hastings est intégré à l'échantillonneur de Gibbs. Des validations sur simulations numériques sont menées pour vérifier la bonne convergence de la méthode. Ces simulations montrent aussi que la prise en compte de la corrélation de la partie CLT est nécessaire pour une bonne identification du champ acoustique.

Chapitre 4 : Applications expérimentales

Le quatrième chapitre présente des applications des méthodes de séparation développées au cours de cette thèse, sur deux types de mesures.

Les premières mesures sont réalisées dans le cadre du projet ADAPT, dans des conditions contrôlées pour la validation des méthodes. Elles sont effectuées en

soufflerie, en présence de deux sources acoustiques et d'un écoulement uniforme à 30 m/s. Les mesures sont réalisées dans trois configurations :

- les sources acoustiques émettent seules, sans écoulement – c'est la mesure de la partie acoustique de référence,
- l'écoulement à 30 m/s est mesuré seul, sans source – c'est la mesure de la contribution CLT de référence,
- les sources acoustiques émettent en présence de l'écoulement à 30 m/s.

L'objectif est d'appliquer les algorithmes de séparation sur cette dernière mesure et de comparer les résultats aux mesures de référence. L'application de l'AF basée sur une CLT décorrélée permet une bonne reconstruction des autospectres. La corrélation de la CLT est ensuite prise en compte, ce qui permet d'améliorer la reconstruction des autospectres acoustiques en basses fréquences. Les performances de séparation des composantes sont également étudiées via des cartes de décompositions en nombres d'ondes, par comparaison avec celle des mesures de référence. Chaque contribution est correctement identifiée, sauf en très basse fréquence où les nombres d'ondes acoustiques sont sous-estimés. Il est montré que les paramètres de CLT identifiés au sein de l'algorithme de séparation sont très proches de ceux obtenus par régression sur les données. Le coût d'une régression étant plus faible que celle de l'identification bayésienne, on recommande alors de simplifier l'algorithme de séparation en utilisant directement les paramètres de la régression dans le modèle bayésien.

La deuxième application est réalisée sur des données fournies par Airbus, acquises par une antenne de 25 microphones collés sur le fuselage d'un avion de ligne en vol. Les sources acoustiques sont principalement le bord de fuite de l'aile et le moteur situés à proximité de l'antenne. La vitesse d'écoulement est de l'ordre de Mach 0.85 et la CLT n'est plus uniforme sur l'antenne. Les résultats de séparation sont comparés à une approche d'extraction de la partie acoustique basée sur des mesures effectuées dans la cabine de l'avion, réputées être décorrélées de la CLT, grâce au filtrage mécanique induit par le fuselage (débruitage référencé). Les paramètres de la CLT sont initialisés par une régression sur les données, puis inférés sein du processus de séparation, ce qui permet une légère correction des paramètres en basses fréquences.

Concernant la reconstruction des éléments diagonaux, l'approche AF basée sur une hypothèse de bruit CLT décorrélé offre une très forte réduction de la contribution de la CLT, mais l'AF prenant en compte la corrélation de la CLT offre une meilleure réduction et une reconstruction des autospectres très proches de ceux fournis par le débruitage référencé. Les performances de séparation sont ensuite comparées en termes de cartographies fréquence-nombres d'ondes. L'AF avec le modèle de CLT corrélée offre une séparation des composantes qui semble

meilleure que le débruitage référencé, avec des résidus faibles qui montrent une bonne adéquation du modèle aux données.

Conclusion et perspectives

Les méthodes de séparations développées pendant cette thèse se placent dans un cadre très général où les sources à l'origine du champ acoustique ne sont pas connues (en termes de localisation, nombre et nature de la propagation) et où très peu d'information de la CLT sont connues *a priori*. L'approche bayésienne permet une régularisation intuitive du problème, et l'échantillonneur de Gibbs, choisit pour la résolution numérique du problème inverse est robuste et facile d'implémentation. Cette approche étant très flexible, plusieurs stratégies pour améliorer la convergence et la régularisation du problème (via un renforcement de la parcimonie de la décomposition) ont pu être implémentées.
En perspectives de ce travail, d'autres méthodes de résolutions du problème inverse pourraient être testées, de façon à améliorer la convergence et réduire les temps de calculs en vue d'un traitement d'un volume de données plus important. Le modèle pourrait être enrichi pour prendre en compte d'autre paramètres incertains de la CLT ou bien exploiter des résultats de simulations numériques souvent menées en compléments des mesures dans le domaine de l'aviation. Différents modèles de sources pourraient également être intégrés à la méthode de séparation proposée.

Enfin, l'étude pourrait être complétée par des identifications de sources réalisées sur les résultats de séparation de façon à évaluer l'apport de la séparation en termes de localisation, quantification, directivité des sources reconstruites. Étudier des cartes d'imagerie acoustiques réalisées sur les résultats de séparation permettrait aussi, par une analyse physique des sources, de compléter la validation des méthodes, notamment pour les cas où les sources ne sont pas connues, telles que pour les mesures en vol.

Contents

Nomenclature

Superscripts and indices

$\cdot^*$	Conjugate
$\cdot^H$	Conjugate transpose (Hermitian)
$\cdot^T$	Transpose
$\cdot_j$	j$^{\text{th}}$ snapshot

Notations and operators

$[u \mid \infty]$	Conditional probability of x given all the other variable
$[u \mid v]$	Conditional probability of x given v
$[u, v]$	Joint probability of x and v
$\lceil \boldsymbol{u} \rfloor$	Diagonal matrix with diagonal elements given by vector $\boldsymbol{u}$
$\hat{\cdot}$	Estimated quantity
$\|\boldsymbol{X}\|_*$	Nuclear norm of $\boldsymbol{X}$ (sum of the eigenvalues)
$\|\boldsymbol{X}\|_1$	$= \sum_{ij} \|\boldsymbol{X}_{ij}\|$, ℓ_1 norm of the matrix (or vector) $\boldsymbol{X}$
$\|\boldsymbol{x}\|_2$	$= (\sum_i \boldsymbol{x}_i^2)^{1/2}$, ℓ_2 norm of the vector $\boldsymbol{x}$
$\|\boldsymbol{X}\|_F$	$= \left(\sum_{ij} \boldsymbol{X}_{ij}^2\right)^{1/2}$, Frobenius norm of $\boldsymbol{X}$
$\otimes$	Kronecker product
$\propto$	"proportional to"
$\sim$	"has the following probability distribution"
$\mathcal{B}ern$	Bernoulli distribution
$\mathcal{B}eta(a, b)$	Beta distribution with shape parameters a and b
$\det(\boldsymbol{A})$	Determinant of the matrix $\boldsymbol{A}$
$\text{diag}(\boldsymbol{A})$	Vector of the diagonal elements of the matrix $\boldsymbol{A}$
$\mathbb{E}\{\cdot\}$	Expected value
$\mathcal{E}$	Exponential distribution
$\boldsymbol{I}_N$	Identity matrix of dimension N
$\imath$	Imaginary unit
$\mathcal{IG}(a, b)$	Inverse-Gamma distribution with shape and scale parameters a and b
$\mathcal{N}_{\mathbb{C}}(a, b)$	Complex normal (multivariate) distribution with mean a and (co)variance b
$\mathcal{N}_{\mathbb{R}}(a, b)$	Real normal (multivariate) distribution with mean a and (co)variance b
$\Re$	Real part operator
$\boldsymbol{S}_{uv}$	CSM of signals $\boldsymbol{u}$ and $\boldsymbol{v}$
$\text{tr}(\boldsymbol{A})$	Trace operator of the matrix $\boldsymbol{A}$

Variables

$\boldsymbol{\epsilon}$	$(M \times 1)$ Small microphone self-noise
$\boldsymbol{a}$	$(M \times 1)$ Measured pressure from the acoustical sources of interest
$\boldsymbol{c}$	$(K \times 1)$ Factors
$\boldsymbol{L}$	$(M \times K)$ Mixing matrix
$\boldsymbol{n}$	$(M \times 1)$ Unwanted noise
$\boldsymbol{q}$	$(K \times 1)$ Factor loading
$\boldsymbol{s}$	$(\kappa \times 1)$ Vector of scaling parameters
$\boldsymbol{y}$	$(M \times 1)$ Total measured pressure
$\mu_\theta, \sigma_\theta^2$	Mean and variance or covariance of the Gaussian distribution associated to a parameter θ
a_θ, b_θ	Hyperparameters associated with a parameter θ
K	Real number of equivalent sources
l	Sparsity parameter
L_q	Number of non-zeros entries of $\boldsymbol{q}$
M	Number of microphones
N_{run}	Number of iteration for the Gibbs sampler
N_s	Number of snapshots for the CSM estimate
p	Amplitude of the TBL contribution
$\lceil \boldsymbol{\gamma}^2 \rfloor$	Covariance of the factors
$\lceil \boldsymbol{\sigma}_n^2 \rfloor$, $\lceil \boldsymbol{\sigma}_\epsilon^2 \rfloor$	Diagonal noise covariance matrices
κ	Number of factors in the PFA model
$\boldsymbol{\nu}$	$(M \times 1)$ Normalized TBL field
$\boldsymbol{\Omega}_\theta$	Posterior covariance matrix of a parameter θ
$\boldsymbol{\theta}$	(3×1) Corcos' parameters

Acronyms and abbreviations

ADAPT ADvanced Aeroacoustic Processing Techniques.

BBSAN BroadBand Shock-Associated Noise.

CCA Canonical Coherence Analysis.

CSM Cross-Spectral Matrix.

DRec Diagonal Reconstruction.

EM Expectation-Maximization.

EVD EigenValue Decomposition.

FA Factor Analysis.

FA-Corr Factor Analysis with Correlated noise model.

LMFA Fluid Mechanics and Acoustics Laboratory.

LVA Laboratory of Vibration and Acoustics.

MCMC Markov Chain Monte Carlo.

MEMS Microelectromechanical systems.

MH Metropolis–Hastings.

MuSiC Multiple Signal Classification.

NLLS Non-Linear Least Squares.

PCA Principal Component Analysis.

PDF Probability Density Function.

RMSE Root Mean Square Error.

RPCA Robust Principal Component Analysis.

SNR Signal-to-Noise Ratio.

SSI Sub-Space Identification.

SVD Singular Value Decomposition.

TBL Turbulent Boundary Layer.

Funding of the research project

One half of this thesis work was funded by the "Centre Lyonnais d'Acoustique" (CeLyA), which itself is funded by the French Ministry of Research as a "Laboratoire d'Excellence". CeLyA brings together 10 laboratories from Lyon and Saint-Étienne.

The other half of the thesis is funded by the European project ADvanced Aeroacoustic Processing Techniques (ADAPT), within the framework of the Clean Sky 2 Joint Undertaking. The ADAPT consortium is composed of two academical research laboratories, the Laboratory of Vibration and Acoustics (LVA)[1] and the Fluid Mechanics and Acoustics Laboratory (LMFA)[2], and two SME, MicrodB[3] and PSA3[4].

Objectives of the ADAPT project

The ADAPT project aims at improving the understanding of noise emission in the aviation field and providing the various actors in the aeronautics industry with tools that allow them to reduce the global noise emission of the aircrafts.

Especially, Airbus conducted in 2018 and before several experimental studies, with microphones mounted on the fuselage of an inflight large aircraft. The objectives of these tests are to study the flight effect on the generation of the acoustic sources associated to the different components of the aircraft, such as the engine or the airfoil. However, the microphones are located behind a turbulent boundary layer, which induces some pressure fluctuations which add to the measurement of the pressure field coming from the acoustic sources of interest. Several tools are aimed to be developed within the ADAPT project, in order to separate the contribution of the turbulent boundary layer from the acoustic sources, applied to inflight measurements, as well as wind tunnel measurements. These tools are based on:

- the cyclostationarity for the separation of the rotating component of the engine,
- the Bayesian imaging to better understand the mechanisms of source generation and also study the ability of performing the separation through a back propagation of the identified sources,
- the use of accelerometer array,
- stochastic models within a Bayesian approach.

The latter point is the object of the present thesis work.

[1] lva.insa-lyon.fr
[2] lmfa.ec-lyon.fr/
[3] www.microdb.vibratecgroup.com
[4] www.psa3.nl

Introduction

Context

The main motivation of the present work is the post-processing of the multichannel measurements performed for the characterization of acoustic sources. This type of measurements is widely conducted in many areas which require source localization, such as ultrasonic non-destructive testing, geophysical exploration, medical imaging, transport design, ... But in some cases, in addition to the measurements of the acoustic sources of interest, some other contributions may be measured simultaneously, such as ambient or electronic noise.

In particular, for the measurements of acoustic sources in presence of a flow, a contribution that is measured incidentally is the pressure fluctuations induced by the flow itself. Indeed, in the case of measurements performed outdoor, underwater, in wind-tunnel or on moving vehicles, it is not always possible to place the sensors away from the flow –for example when a measurement has to be performed close to an aeroacoustic source or in a closed tunnel.

In this case, the flow along the rigid measuring device induces a velocity gradient which causes strong pressure fluctuations. For strut-mounted microphones, the turbulences are induced by the sensor itself or its stand, whereas for wall-mounted microphones, a turbulent boundary layer develops over the flat surface. These pressure fluctuations are measured in addition to those induced by the acoustic sources, sometimes leading to very low signal-to-noise ratios.

The vortex structures in the Turbulent Boundary Layer (TBL) produce a random pressure field, which can be described statistically. The physical description of this field is often based on the assumptions of stationary and homogeneity (*i.e.* statistically invariant in time and space), which allows the time averaging of the measured signals, and also the study of the involved correlation lengths. The study of the statistical characteristics of the TBL has given rise to many models, in which the correlation lengths are described with a steep decrease. This implies that over a wide frequency range, the acoustic and TBL fields have very different correlation lengths (see Fig. 1). Especially, the microphone spacings involved for acoustic source localization (which are of the order of magnitude of the wavelength of the acoustic field) are generally greater than the correlation length of the TBL.

Even though the frequency contents of the two fields overlap, making frequency filtering impossible, the difference of correlation can be exploited to perform a post-processing separation of the two fields, which is proposed in this work. Specifically,

the present thesis is focused on one of the objectives of the ADAPT project, which is the development of advanced signal processing tools to perform the separation of the aerodynamic and acoustic contributions, and a particularly targeted application is the measurements carried out in the aviation industry.

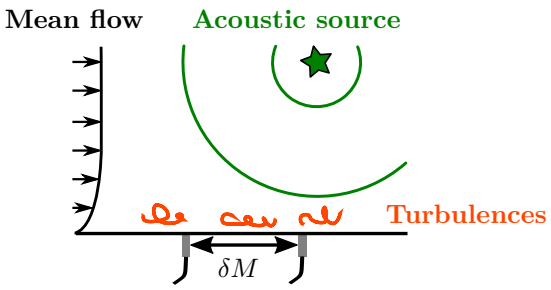

Figure 1: Illustration of the wall pressure fluctuations.

Issues of the separation

The benefits of an efficient separation are twofold. On the one hand, the characterization of the TBL part allows a better understanding of the vibro-acoustic excitation. In a general context, the characterization of the wall-pressure field beneath a turbulent boundary layer has been initiated in the late 1950s. From then and until now, the understanding of the TBL has been a challenge for several applications, such as the control of the fatigue loading on structures like aircraft, the reduction of the vehicle interior noise or the noise generated by piping systems with internal turbulent flow. In the aerospace field, the TBL noise of interest depends on the measurement setup. The microphone array can be mounted on the walls of a closed test section, on the outer fuselage of an aircraft, or on a stand in open test section or outdoor, depending on the part of the aircraft one wants to study the noise emission from.

On the other hand, a correct estimation of the acoustic part is required for an appropriate quantification and localization of the aeroacoustic sources. Especially, in the civil aviation industry, it is important to know the noise level produced by each constituent element of an aircraft in order to improve its design and reduce the global noise emitted at each flight phase (climb, cruise and descend). Smith (1989) describes a very large number of aircraft noise sources. They can be classified into two categories: the airframe and the engine noise. The aircraft having a large surface area, the amount of airframe noise is significant, especially in take-off and

approach configurations, which implies the use of high-lift devices and landing gears. The airframe noise is generated by elements of different size (from centimeters for window surrounds, to many meters for the fuselage), which implies many scales of turbulence and thus a broadband noise in the far-field. The engine noises are of different kinds. They can be tonal or cyclostationary for all the rotating elements and they can also be broadband from random pressure fluctuations, caused by the turbulence in the inlet stream, the boundary layers or blade wakes. Finally, another main source of broadband noise is the high-velocity jet exhaust (Tam, 1995). Consequently, a wide variety of sources are of interest, that can be spatially extended or compact, and that cover the whole audible domain.

Overview of the thesis

In this context, several strategies already exist to perform the separation of the acoustic field from the TBL contribution. These methods from the literature are detailed in the **first chapter**. However, these experimental and post-processing techniques, show some limitations or unsatisfying performances.

Therefore, in the **second chapter**, a post-processing technique for the separation is proposed, based on the assumption of a TBL noise totally uncorrelated over the microphones. The separation is performed through a matrix decomposition of the measurement Cross-Spectral Matrix (CSM). The inverse problem is first addressed with a probabilistic point of view, solved with an Expectation-Maximization (EM) algorithm. Then, it is developed in a Bayesian framework, in order to design a more complex model that enforces the sparsity of the solution, which makes the inversion more robust. The proposed approach is also benchmarked against the methods from the literature, on a numerical case. The results obtained for an uncorrelated noise are encouraging and the Bayesian framework offers the opportunity to extend the model to a correlated noise model.

Therefore, in the **third chapter**, a CSM decomposition incorporating a correlated noise model is developed, based on a physical boundary layer model. This Bayesian framework offers the possibility to infer the parameters of the TBL, taking into account their prior uncertainties.

Finally, in the **fourth chapter**, some experimental applications are proposed, first on closed wind tunnel measurements with controlled sources, then on measurements acquired from an array mounted on the fuselage of an inflight aircraft. The performance of the denoising is evaluated by analysis of autospectra, wave number decomposition and by comparison with denoising performed using noise-free reference channels.

1

Literature survey on the noise and signal decomposition

Contents

1.1 Introduction

The use of multi-channel acquisition system is widespread for acoustic imaging application. In this context, the signal of interest is the contribution of the acoustic sources to the antenna, and the extraction of the other contributions is then called "denoising". Noise reduction is a key issue for the improvement of acoustic imaging

performance, particularly in the field of aeroacoustics where the dominant noise often comes from the Turbulent Boundary Layer (TBL).

1.1.1 Experimental mitigation of the TBL contribution

Some way to optimize the microphone implementation has been investigated to reduce the effect of TBL noise especially for measurements in closed test sections using flush mounted microphones. The microphones are for example recessed in pinholes (Farabee and Casarella, 1986) or in tubes (Arguillat et al., 2010). They can also be covered with wired mesh (Jaeger et al., 2000; Fleury et al., 2012). However, these last experimental strategies are recent and still in development since they have to fulfill a lot of crucial criteria: have a good mechanical resistance to the flow, do not induce additive noise and do not filter out the acoustic contribution.

For in-flight measurements, where the microphones are flush-mounted on the fuselage of the aircraft, the covering is not feasible and the microphone recession can be performed only on the windows such as in Palumbo (2012) or Haxter and Spehr (2017). Therefore, other experimental approaches are used to mitigate the effect of the TBL . For example, the use of microphones with large membranes (Blake and Chase, 1970) allows filtering out the high wavenumbers through spatial averaging. Analogously, similar devices are used in the hydroacoustic field, with the use of large hydrophones, embedded behind an elastomer layer (Ko and Schloemer, 1991).

Another way to filter out the high wavenumbers experimentally is to exploit accelerometers mounted on a thin plate submitted to the TBL . This kind of apparatus can be used in place of a microphone array (Lecoq et al., 2014; Leclère et al., 2015), but also on the side of a microphone array, to be used as noise-free references for a post-processing denoising based on the coherence (Leclère et al., 2021; Dinsenmeyer et al., 2019). The first method requires to solve an inverse problem, whereas the second one needs extra measurement points and is limited by the difficulty of choosing the number of references that describes optimally the acoustic field.

Some experimental reductions of the microphone self-noise are also inverstigated concerning strut-mounted microphones. For example, the membrane can be protected from the flow impact by microphone forebodies that are aerodynamically optimized (Allen and Soderman, 1993) or by windscreens and foams balls, which can, however, create wake noise (Mueller (2002), chap. 1).

1.1.2 On the use of a background noise measurement

In practical situations, it is sometimes possible to measure separately the contaminating background noise by either simply "switching off" the sources of interest or by performing measurements without the mock-up in wind tunnel, for instance. This background measurement can be used to advantage to remove its influence when the total noise field is actually measured. This can be done through post-processing approach such as a direct subtraction (Berouti et al., 1979; Boll, 1979; Huber et al., 2009; Blacodon and Bulté, 2014) or subspace identification described in Sec. 1.4.3. But the main limit of these approaches is that a representative background noise measurement (*i.e.* without the source of interest) is not always available since the sources themselves can influence the noise properties.

1.1.3 Statement of the post-processing problem

Besides from the experimental approaches, there exist many post-processing tools that have been developed to identify the acoustic contribution in the measurements. The M pressure measurements at each microphone point can be stored into a complex vector $\boldsymbol{y}$, which results from the sum of an acoustic contribution $\boldsymbol{a}$ and noise vector $\boldsymbol{n}$, that contains mainly the TBL contribution but also all the additive sources of noise and errors. At one frequency in the Fourier domain, this sum reads:

$$\boldsymbol{y} = \boldsymbol{a} + \boldsymbol{n}. \tag{1.1.1}$$

It is common in the field of aeroacoustics to store the measurements in a Cross-Spectral Matrix (CSM)[1], which is defined by the covariance matrix of the Fourier coefficients of the measurements. Theoretically, the CSM is defined as follows:

$$\boldsymbol{S}_{yy} = \mathbb{E}\{\boldsymbol{y}\boldsymbol{y}^H\}, \tag{1.1.2}$$

where the superscript H indicates the complex conjugate transpose (or Hermitian) operator. Since the measurement are performed on a finite duration time, this quantity has to be estimated by averaging over N_s successive overlapping windowed time signal segments (hereafter called *snapshots*), following Welch's periodogram method:

$$\hat{\boldsymbol{S}}_{yy} = \frac{1}{N_s}\sum_{j=1}^{N_s} \boldsymbol{y}_j \boldsymbol{y}_j^H, \quad j = 1, \ldots, N_s, \tag{1.1.3}$$

where $\hat{\cdot}$ is used to indicate an estimated quantity.

[1] Also called Population Covariance Matrix (theoretical quantity) or Sample Covariance Matrix (estimated quantity) in the signal processing field.

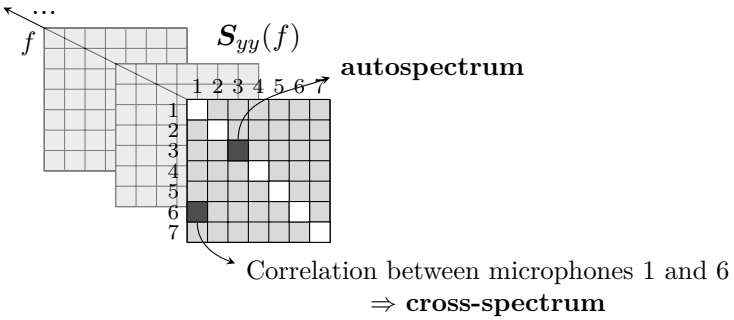

Figure 1.1: Representation of the CSM for an array of $M = 7$ sensors. At each frequency f, the CSM is a $M \times M$ Hermitian matrix.

This quadratic representation of the measurements reduces the size of the stored data through averaging, while retaining the sufficient statistic – provided that the signals are stationary – that contains all the required information for spectral analysis or perform imaging. In addition, this representation highlights the correlation structure of the data (and thus indirectly the coherence[2]), for each microphone pair (see Fig. 1.1).

Replacing $\boldsymbol{y}_j$ in Eq. (1.1.2) by the sum of Eq. (1.1.1), leads to

$$\boldsymbol{S}_{yy} = \boldsymbol{S}_{aa} + \boldsymbol{S}_{nn} + \boldsymbol{S}_{an} + \boldsymbol{S}_{na}. \tag{1.1.4}$$

Assuming that the noise and the acoustic contributions are uncorrelated implies that the cross-terms $\boldsymbol{S}_{an}$ and $\boldsymbol{S}_{na}$ converges to zero when the number of snapshots N_s tends to infinity. Then, the CSM of the measurements can be approximated as follows:

$$\hat{\boldsymbol{S}}_{yy} \approx \boldsymbol{S}_{aa} + \boldsymbol{S}_{nn}. \tag{1.1.5}$$

From this, the identification of the acoustic contribution in the measurements, namely the denoising problem is the following:

Problem 1 *Given an estimate of the CSM $\hat{\boldsymbol{S}}_{yy} \approx \boldsymbol{S}_{aa} + \boldsymbol{S}_{nn}$, where $\boldsymbol{S}_{aa}$ and $\boldsymbol{S}_{nn}$ are both unknown, recover $\boldsymbol{S}_{aa}$.*

It is noteworthy that the noise power is allowed to vary between different microphones and to be much higher than the acoustic source power. The present chapter is dedicated to the presentation of the methods from the literature that aims at solving Prob. 1 or try to minimize the contribution of the noise $\boldsymbol{S}_{nn}$.

[2]The coherence between the microphone k and l is defined by

$$\gamma_{kl} = \frac{|\boldsymbol{S}_{yy_{kl}}|^2}{\boldsymbol{S}_{yy_{kk}} \boldsymbol{S}_{yy_{ll}}}.$$

In order to solve Prob. 1, the methods outlined in this chapter exploit the correlation difference between the signal from the TBL and measurement noises and the signal coming from the acoustic sources. In the case where the sensor array is designed for the characterization of the acoustic sources, in the audible range, with microphone interspacings ranging from centimeters to meters, the acoustic field is strongly correlated on the antenna (see illustration in Fig. 1).

On the other hand, the correlation of the TBL noise is related to the structure of the vortices, which depends on the TBL thickness, which in turn depends on the mean flow profile. In the low-frequency range, the wall pressure excitation is mainly induced by the large turbulent structures, whereas in the high-frequency range, it is the small turbulent structures, located in the inner TBL that contribute to the wall pressure field. Typical layer thicknesses generally go from the millimeter to few centimeters, depending on the flow characteristics, and so is the typical spatial correlation lengths. Moreover, the streamwise and transversal[3] correlations generally decrease exponentially with the frequency (Farabee and Casarella, 1991; Bull, 1996). Therefore, the correlation of the TBL field over the antenna is much lower than the correlation of the acoustic field, as long as the turbulence structures are smaller than the acoustic wavelength.

For these reasons, many methods for noise suppression in the literature consider the TBL noise to be totally uncorrelated over the microphones. This is also the case for all the other sources of noise, that can be ambient or electronic for example. Under this hypothesis, the noise CSM can statistically be modeled by a diagonal matrix,

$$\boldsymbol{S}_{nn} = \lceil \boldsymbol{\sigma}_n^2 \rfloor, \tag{1.1.6}$$

where the notation $\lceil \boldsymbol{u} \rfloor$ stands for a diagonal matrix whose diagonal entries are the elements in vector $\boldsymbol{u}$. This implies that

$$\hat{\boldsymbol{S}}_{yy} \approx \boldsymbol{S}_{aa} + \lceil \boldsymbol{\sigma}_n^2 \rfloor. \tag{1.1.7}$$

1.1.4 Organization of the chapter

The work presented in this thesis focuses on denoising methods that do not make any assumptions about the nature and propagation of the acoustic sources, because they are often uncertain when characterizing aeroacoustic sources, especially in the case where the flow is not completely spatially uniform. Therefore, the methods based on the use of acoustic imaging are not presented here. The reader can refer to the work of Sijtsma et al. (2019), that gives a benchmark of the denoising results

[3] *i.e.* normal to the stream axis

obtained from imaging methods. Jiang et al. (2020) and Xia et al. (2017) also make use of a beamforming step to reduce the diagonal of the CSM.

Moreover, the present study focuses mainly on methods that do not make use of a background noise measurement, due to the difficulty of acquiring a representative background noise (some popular methods using background noise are however briefly discuss in Sec. 1.4.3).

Six approaches are discussed in the chapter, using the hypotheses of totally uncorrelated noise and/or of high correlation of the acoustic filed. The first three methods are historical, but still widely used today, and the last three ones are methods that have been newly proposed in the context of aeroacoustics during the last decade.

The principle all the methods is given here, and their performances are concurrently compared with the proposed approach in Sec. 2.5 on numerical test case and in Sec. 4.1 on wind-tunnel measurements. The present chapter is partially based on the article:

Dinsenmeyer, A., **Antoni, J.**, **Leclère, Q.**, and **Pereira, A.** A probabilistic approach for cross-spectral matrix denoising: Benchmarking with some recent methods. *The Journal of the Acoustical Society of America*, 147(5):3108–3123, 2020

1.2 Diagonal removal

As discussed in the introduction, assuming a noise uncorrelated over the microphones can be described by a diagonal CSM when the number of snapshots tends to infinity. Therefore, a common practice is to apply the imaging process using the measurement CSM with its diagonal entries set to zero (Christensen and Hald, 2004; Sijtsma, 2004, 2007), which reads

$$\bar{\boldsymbol{S}}_{yy} = \boldsymbol{S}_{yy} - \lceil \mathrm{diag}(\boldsymbol{S}_{yy}) \rfloor, \tag{1.2.1}$$

$$= \boldsymbol{S}_{yy} - \lceil \mathrm{diag}(\boldsymbol{S}_{aa}) \rfloor - \lceil \boldsymbol{\sigma}_n^2 \rfloor. \tag{1.2.2}$$

The noise can thus be theoretically totally removed, but this "trimmed" CSM is in general positive semi-definite, due to the deletion of the term $\lceil \mathrm{diag}(\boldsymbol{S}_{aa}) \rfloor$.

One can thus wonder what is the effect of the deletion of this term on the beamformer output. A single source located at a point with coordinates $\boldsymbol{r}_0$ and strength q_0 generates an acoustic field

$$\boldsymbol{a}_m = q_0 \boldsymbol{g}_{m0}, \quad \text{with } m = 1, \ldots, M, \tag{1.2.3}$$

at each microphone m. The vector $\boldsymbol{g}_{m0}$ is the propagation vector from the source to the microphone m defined by the free space Green's function:

$$\boldsymbol{g}_{m0} = \frac{\mathrm{e}^{-\imath k\|\boldsymbol{r}_m - \boldsymbol{r}_0\|_2}}{4\pi\|\boldsymbol{r}_m - \boldsymbol{r}_0\|_2}. \tag{1.2.4}$$

The output of the classical beamformer with diagonal removal at a position of index i is then

$$\tilde{\boldsymbol{S}}_{qq_i} = \boldsymbol{w}_i^H \left(\boldsymbol{S}_{aa} - \lceil \mathrm{diag}(\boldsymbol{S}_{aa})\rfloor\right) \boldsymbol{w}_i, \tag{1.2.5}$$

with $\boldsymbol{w}_i$ the steering vector. Building a steering vector that minimizes $\|\boldsymbol{w}_i^H \boldsymbol{a} - \boldsymbol{q}_i\|_2^2$ leads to

$$\boldsymbol{w}_i = \frac{\boldsymbol{g}_i}{\boldsymbol{g}_i^H \boldsymbol{g}_i}. \tag{1.2.6}$$

Then, Eq. (1.2.5) can be developed using the expression of this steering vector and of the acoustic field (Eq. (1.2.3))

$$\tilde{\boldsymbol{S}}_{qq_i} = q_0^2 \Bigg(\underbrace{\frac{\sum_{m=1}^M \boldsymbol{g}_{im}^* \boldsymbol{g}_{0m} \sum_m^M \boldsymbol{g}_{0m}^* \boldsymbol{g}_{im}}{\|\boldsymbol{g}_i\|_2^4}}_{\text{Point Spread Function}} - \underbrace{\frac{\sum_{m=1}^M \boldsymbol{g}_{im}^* \boldsymbol{g}_{0m} \boldsymbol{g}_{0m}^* \boldsymbol{g}_{im}}{\|\boldsymbol{g}_i\|_2^4}}_{\boldsymbol{Z}_i} \Bigg). \tag{1.2.7}$$

The second term $\boldsymbol{Z}_i$ is due to the diagonal removal and can be developed using the expression of the propagation vector (Eq. (1.2.4)),

$$\boldsymbol{Z}_i = \frac{\sum_{m=1}^M \|\boldsymbol{r}_i - \boldsymbol{r}_m\|_2^{-2} \|\boldsymbol{r}_0 - \boldsymbol{r}_m\|_2^{-2}}{\left(\sum_{m=1}^M \|\boldsymbol{r}_i - \boldsymbol{r}_m\|_2^{-2}\right)^2}. \tag{1.2.8}$$

From these calculations, it appears that the diagonal terms of the CSM do not contribute to the resolution of the beamforming. The diagonal terms are real and do not carry any phase information and only act as an offset that is space-dependent due to the divergence of the spherical waves. It only depends on the geometry of the source map and the microphone distribution. This is illustrated in Fig. 1.2. This figure shows a reduction of the side lobes due to the diagonal removal – for this reason, it is sometimes used on noiseless measurements.

Looking at the source point $i = 0$, the geometrical effect is more pronounced if the distances between the source point and the microphones are very variable (for example in the near-field). In practice, the beamforming is often applied in conditions where the distance from the sources to the microphones are all of the

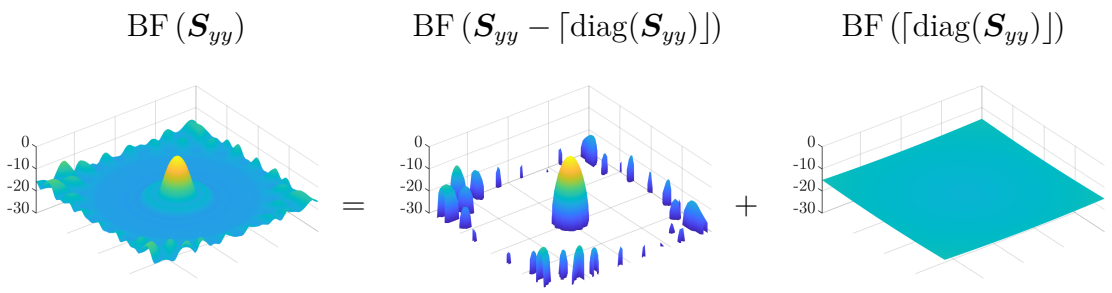

Figure 1.2: Beamforming maps (in dB) of the full CSM , with diagonal removal and of the diagonal elements (from left to right), for a source located at the center of the map.

same order of magnitude. In this case,

$$\boldsymbol{Z}_0 \approx \frac{M\|\boldsymbol{r}_0 - \boldsymbol{r}_m\|_2^{-4}}{\left(M\|\boldsymbol{r}_0 - \boldsymbol{r}_m\|_2^{-2}\right)^2} = \frac{1}{M}. \tag{1.2.9}$$

The same results is obtained if a convected propagator is used. From this observation, Dougherty (2002) suggests performing a correction by adding $10\log_{10}\left(\frac{M}{M-1}\right)$ to the beamforming maps obtained with diagonal removal. Note that this correction term is less than 0.1 dB for arrays made up of 44 sensors or more.

In the case where several sources contribute to the acoustic field, the output of the beamformer with diagonal removal, under the assumption that the sources are far enough (which implies that the associated steering vectors are orthogonal and thus that their inner product is negligible) becomes

$$\boldsymbol{S}_{qq_i} = \frac{1}{\|\boldsymbol{g}_i\|_2^4}\left(q_0^2\,\mathrm{PSF}(\boldsymbol{r}_0) - \sum_{n=0}^{N-1} q_n^2 \frac{\sum_{m=1}^{M} \boldsymbol{g}_{im}^* \boldsymbol{g}_{nm} \boldsymbol{g}_{nm}^* \boldsymbol{g}_{im}}{\|\boldsymbol{g}_i\|_2^4}\right) \tag{1.2.10}$$

where $\mathrm{PSF}(\boldsymbol{r}_0)$ is the point spread function at the point sources in $\boldsymbol{r}_0$. This shows that the quantification error accumulates with the number of sources.

In conclusion, the effect of the uncorrelated noise can theoretically be removed completely by the diagonal removal, with no impact on the resolution. However, this is at the expense of the accuracy in terms of quantification. Although these quantification errors are small in general, they accumulate when performing area integrations, such as in the Source Power Integration method (Brooks and Humphreys, 1999), and then become not negligible. Fenech (2009) shows some errors going up to 1.7 dB. Moreover, Dougherty (2002) and Sijtsma (2004) suggest considering for the integration only the source auto-powers that are less than a given threshold below the peak level. In doing so, the small and negative sources are neglected.

1.3 Wavenumber filtering

Wavenumber decomposition is convenient to characterize the pressure fluctuation under a TBL that develops over a plane surface. Concerning surfaces exposed to a turbulent flow, the wavenumber spectrum is representative of the phase velocity of the TBL, and is therefore needed to predict the possible excitation of this TBL.

This decomposition is also the basis for a separation of the acoustic and TBL contributions through a filtering process. As explained in the introduction, the correlation lengths of the two contributions are different, which in the wavenumber plane translates into two distinct domains. These two domains are schematically represented in Fig. 1.3, which shows the typical wavenumber spectrum obtained below a TBL. For a detailed review on wall pressure fluctuation under TBL, the reader can refer to the article of Bull (1996).

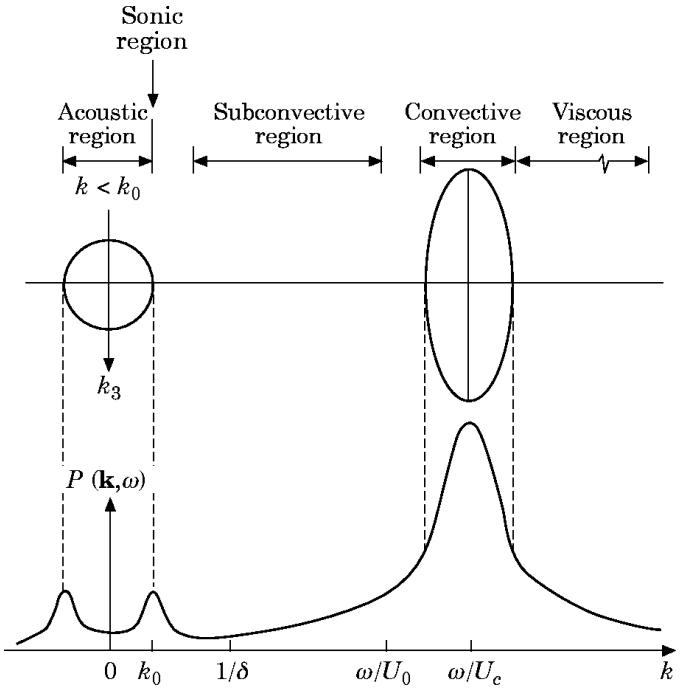

Figure 1.3: Schematic representation of the wavenumber spectrum at a given frequency, at low Mach number. From Bull (1996) and after Howe (1991)

.

First, the acoustic region is filled by the waves whose phase velocity in the measurement plane is greater or equal to the speed of sound in the propagation fluid. This region is often described as the *acoustic circle* in reference to the non-convected case, but in presence of a mean flow, this circle is in fact an ellipse (Koop and Ehrenfried, 2008; Haxter and Spehr, 2019), bounded by:

$$k_x = \frac{2\pi f \cos\theta}{c_0 + U_c \cos\theta} \quad \text{and} \quad k_y = \frac{2\pi f \sin\theta}{c_0 + U_c \cos\theta} \tag{1.3.1}$$

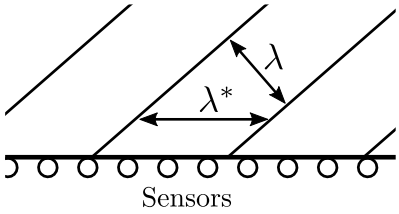

Figure 1.4: Effect of the incidence angle of a plane wave on its measured wavelength.

for a flow with a convection speed U_c, along the x-axis, with $0 \leq \theta \leq 2\pi$ and c_0 the speed of sound in the ambient air at rest. Depending on the incidence angle of the different acoustic waves contributing to the measurement, the acoustic circle may be more or less filled. As shown on Fig. 1.4, the measured wavelength λ^* is seen larger than the real wavelength when the incident angle get closer to the surface normal. Therefore, the measured wavelength is greater or equal to the effective wavelength, and at a given frequency, the measured wavenumber is smaller or equal to the effective wavenumber. The second region is centered on the convective ridge at $k = \frac{\omega}{U_c}$, usually described by an elliptical shape. The width of this region is driven by the flow parameters such as the convection speed or the coherence loss and can be evaluated experimentally.

Looking at the turbulent components, the involved wavenumbers are higher than the acoustic ones (especially at low Mach number). Therefore, in order to have a resolution satisfying Shannon's criterion, the higher the studied frequency and/or the lower the convection velocity, the closer the sensors should be. The measurement can be performed using only one or two line arrays (along and perpendicular to the flow axis, as in Abraham and Keith (1998) and Palumbo (2012)), if the transverse and longitudinal fluctuations are supposed to be independent in the two directions. In practice, this independence is not always verified (Chase, 1980) and the measurements have to be performed over the whole surface of interest. This type of measurements is rather rare because of its cost, in terms of time and number of sensors, and also because the sensor width may limit the minimal sensor interspacing – even if the use of MEMS array should address the two latter problems. Arguillat et al. (2010) reduce the number of sensors by using a rotating line antenna and reduce the sensor interspacings up to the millimeter thanks to the use of recessed microphones.

In practice, these wavenumber spectra are calculating either from a Discrete Fourier Transform if the measurement point are regularly spaced, or approached by a beamforming performed in the wavenumber space, which is expressed at

one frequency by:

$$A_i = \boldsymbol{w}_i^H \boldsymbol{S}_{yy} \boldsymbol{w}_i, \tag{1.3.2}$$

with the steering vectors defined by plane waves:

$$\boldsymbol{w}_i = \mathrm{e}^{\imath k_{x_i} \boldsymbol{x} + \imath k_{y_i} \boldsymbol{y}}. \tag{1.3.3}$$

where $\boldsymbol{x}$ and $\boldsymbol{y}$ are the coordinates along the x and y axis of the microphones.

Using either a Fourier transform or a beamformer, a deconvolution can be performed to reduce the side lobes induced by the finite size of the antenna (Haxter and Spehr, 2019; Ehrenfried and Koop, 2008; Prigent et al., 2019). Then, the acoustic and aerodynamic spectra can be obtained through an integration of the wavenumber components of each domain.

Ehrenfried et al. (2006) also make use of the wavenumber representation to separate the acoustic and TBL contributions. Their method, referred to as BiClean in the literature is based on an iterative process that search for the maximum of the beamforming in the scan plane or in the wavenumber space. A CSM is then generated from this maximum and added either to the acoustic CSM or the noise CSM depending on the domain to which the maximum was related.

As for the other methods based on the wavenumber decomposition, the main limitations of this approach are the experimental costs and that they are only effective if the acoustic and noise regions are well separated, which is generally not the case at low frequencies.

1.4 Subspace identification

The subspace identification methods are based on the assumption that signal and noise span different subspaces, which can be clearly identified in the distribution of the eigenvalues. The subspace spanned by the highest eigenvalues is considered as an approximation of the noiseless signal.

1.4.1 Distribution of the signal and noise eigenvalues

If the noise is stationary, zero-mean and complex Gaussian with a variance $\boldsymbol{\Omega}_n$, then the corresponding CSM $\boldsymbol{S}_{nn}$ follows a Complex Wishart distribution with covariance $\boldsymbol{\Omega}_n$ and N_s degrees of freedom, which reads

$$N_s \boldsymbol{S}_{nn} \sim \mathcal{W}(\boldsymbol{\Omega}_n, N_s) \tag{1.4.1}$$

Under the assumptions that the noise is independent identically distributed with common variance σ_n^2 and that the number of sensors M and snapshots N_s tends to infinity, while the ratio $\nu = M/N_s$ remains finite, the eigenvalues λ of the noise CSM are distributed following a Marčenko–Pastur Probability Density Function (PDF) (Marčenko and Pastur, 1967; Gerstoft et al., 2012):

$$[\lambda] = \frac{\sqrt{(\lambda_+ - \lambda)(\lambda - \lambda_-)}}{2\pi\nu\lambda\sigma_n^2}\mathbf{1}_{\lambda\in[\lambda_-,\lambda_+]} \quad \text{with} \quad \lambda_\pm = \sigma_n^2\left(1 \pm \sqrt{\nu}\right)^2. \tag{1.4.2}$$

The eigenvalues thus spread around σ_n^2 up to the upper and lower limits $\lambda_\pm$ that depend on the ratio ν. This PDF is plotted in Fig. 1.5a for different values of ν, and for $\sigma_n^2 = 1$.

In order to evaluate how the signal and noise subspaces can be identified looking at the eigenvalue distribution, some CSMs are simulated. These CSMs are obtained from a random noise of unit variance, uncorrelated on $M = 60$ sensors. Five uncorrelated sources are also added, such as the Signal-to-Noise Ratio (SNR) is 0, -10 and -20 dB. In Figs. 1.5b to 1.5d are plotted the eigenvalues of these CSMs for each SNR and for three different number of snapshots (which give $\nu = 1/2$, $1/8$ and $1/40$, as on the PDFs of Fig. 1.5a).

Theoretically, the distribution in Eq. (1.4.2) is only valid asymptotically, but it also fits very well the eigenvalue distribution of the noise subspace for a limited array size. These simulations show that for high SNRs, there is a clear separation in the eigenvalue distribution of the signal and noise part. At -10 dB, even if the signal eigenvalues are higher than the noise eigenvalues, the decay is steady and there is no clear separation between the two subspaces. Finally, if the number of snapshots is low, the eigenvalues of the noise are spread out and then overlap the signal eigenvalues. This overlapping also occurs for very low SNRs.

1.4.2 Subspace identification methods

Subspace identification is widely used for various applications, such as target detection, data visualization, classification, ... In the context of source and noise separation, it can also be used to mitigate the effect of an uncorrelated noise during imaging process. Moreover, subspace identification provides a reduction of the dimension of the data.

The objective of subspace identification is to find the best subspace to project data to minimize a cost function. There exist many subspace identification methods, relying on different objective functions, such as the Principal Component Analysis

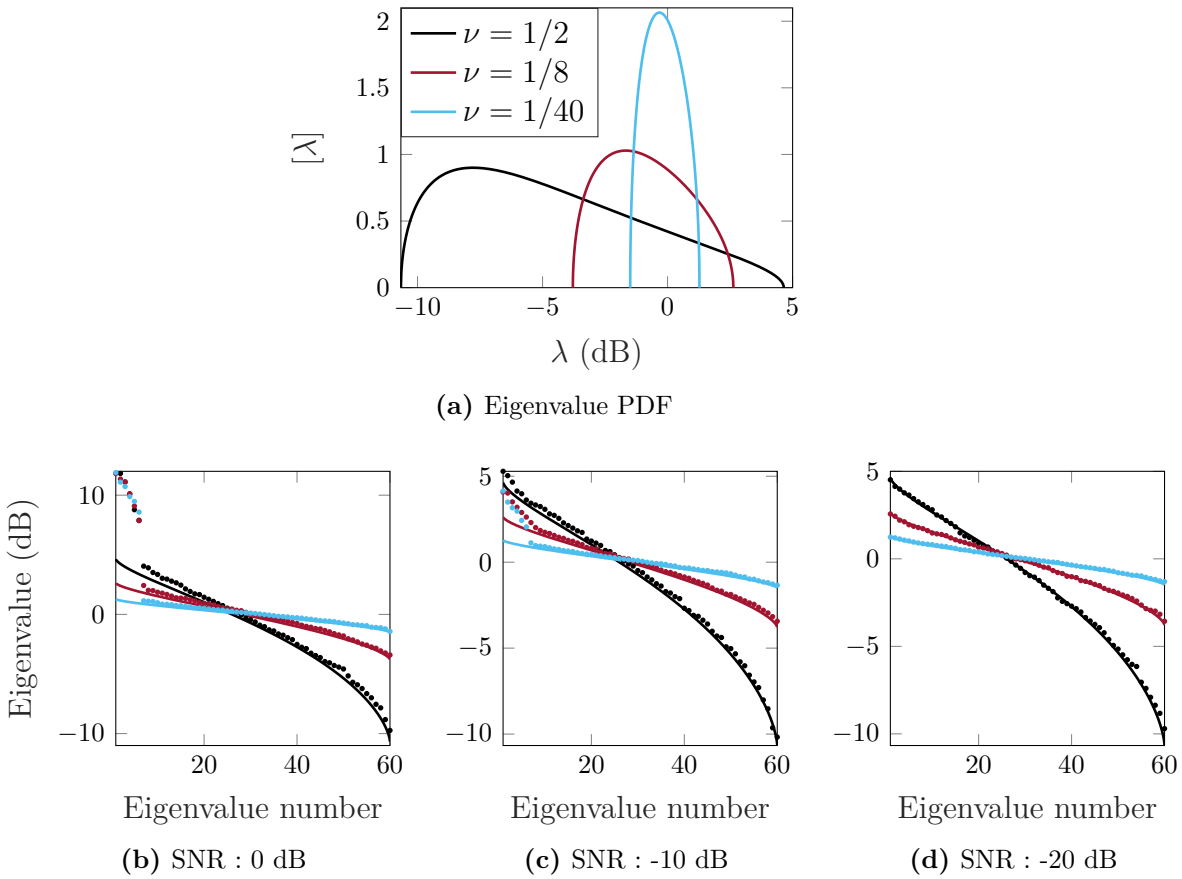

(a) Eigenvalue PDF

(b) SNR : 0 dB **(c)** SNR : -10 dB **(d)** SNR : -20 dB

Figure 1.5: (a) Eigenvalue PDF for three ratios ν. Eigenvalues from simulated CSM (dots) and predicted by Marčenko and Pastur (1967) (solid line), for the same three ratios ν and different SNR.

(PCA) (Jolliffe, 2002) and the Singular Value Decomposition (SVD) which maximizes the data representation (see the work from Druault et al. (2013) for aeroacoustic applications), or the Maximum noise fraction and the Noise Adjusted Singular Value Decomposition (Lee et al., 1990), that maximizes the SNR in doing a noise whitening (transformation to make the noise covariance become an identity matrix) before a PCA on the whitened data. This whitening step requires a background noise measurement.

One of the most popular imaging method based on subspace identification is Multiple Signal Classification (MuSiC) (Schmidt, 1986). It derives from the Capon beamforming (Capon, 1969)[4] in which the measurement CSM is replaced by the noise subspace. In doing so, MuSiC minimizes the distance between the steering vectors of the beamformer and the signal subspace, under the assumption that noise and signal subspaces are orthogonal. Indeed, as the noise subspace is orthogonal to the signal subspace, this minimal distance is given by the projection of the steering vectors on

[4]see also Pisarenko (1973) for a related approach

the noise subspace. Therefore, MuSiC induces a loss of the source levels. Note that there is no reason for the signal and noise subspaces to be orthogonal in general.

Subspace methods can significantly improve the image resolutions, including for aeroacoustic applications (Long, 2003; Sarradj, 2010; Suzuki, 2011). However, as shown in Sec. 1.4.1, the distinction between signal and noise eigenvalues can be difficult to make, and a main problem arising in the subspace approaches is how to set the appropriate threshold which separates the two subspaces, when the exact number of sources is unknown. The number of components to be retained can be estimated using methods based on the Akaike Information Criterion (Akaike, 1974; Wang and Kaveh, 1985) or based on the Minimum Description Length criterion (Wax and Kailath, 1985).

Note that some imaging techniques do not perform a clear subspace separation but instead give weight to the highest eigenvalues of the measurement CSM before applying a classical beamforming. For example, in the work from Huang et al. (2012), the highest eigenvalue is amplified by a loading parameter determined by an iterative procedure. Functional Beamforming (Dougherty, 2014) performs an exponentiation of the eigenvalues which results in a penalization of the small eigenvalues, and therefore enhance the dynamic range and the spatial resolution (Merino-Martínez et al., 2016).

The present literature review is not exhaustive and the reader can also refer to the wide literature on compressed sensing to find out more approaches for subspace separation.

1.4.3 Subspace identification with a background noise measurement

In the aeroacoustic field, it is common to perform a background noise measurement. In wind tunnel, it is generally done by removing the object of interest from the tunnel. It is then assumed that the background noise will not change when measuring the sources of interest. In practice the background measurement may not be representative, for example in the case where a source itself generates an unwanted noise (which is the case for ducted fan noise).

The aforementioned method assumes that the signal lies in a low-rank subspace and that the noise is uncorrelated. When a background noise measurement is available, some other denoising method can be used, that can take into account a correlation structure of the noise. In the case of a correlated noise, a natural extension of the subspace methods is the oblique projection. An example of this

approach is given in Behrens and Scharf (1994), where the noise structure is known and the signal and noise subspace are supposed to be disjoint.

Other subspace approaches have been developed to make use of the background measurement. Bulté (2007) build a basis from the background noise CSM and then performs a generalized SVD on the signal and noise basis in order to decompose the measurement CSM to be denoised.

Another recent but popular method in the aircraft industry is the Background Subtraction proposed by Bahr and Horne (2017). It is based on an EigenValue Decomposition (EVD) of the background noise CSM and has the main advantage to preserve the positive semi-definiteness of the denoised CSM. Assuming that the noise and signal are mutually uncorrelated, the measurements $\boldsymbol{S}_{yy}$ results from the sum of an unknown signal CSM $\boldsymbol{S}_{aa}$ and a noise CSM to be removed $\boldsymbol{S}_{nn}$ then, the Background Subtraction algorithm is composed of four steps:

❶ Build the whitening operator $\boldsymbol{B}_n$ *via* an EVD of the background noise measurement:

$$\boldsymbol{S}_{nn} = \boldsymbol{X}_n \boldsymbol{\Gamma}_n \boldsymbol{X}_n^H = \boldsymbol{B}_n \boldsymbol{B}_n^H. \tag{1.4.3}$$

❷ Apply the whitening operator to the noisy measurements:

$$\begin{aligned} \boldsymbol{B}_n^H \boldsymbol{S}_{yy} \boldsymbol{B}_n &= \boldsymbol{B}_n^H \boldsymbol{S}_{aa} \boldsymbol{B}_n + \boldsymbol{I}, \\ \Leftrightarrow \quad \hat{\boldsymbol{S}}_{yy} &= \hat{\boldsymbol{S}}_{aa} + \boldsymbol{I}. \end{aligned}$$

❸ Perform a second EVD to extract a positive semi-definite (and Hermitian) signal CSM:

$$\begin{aligned} \hat{\boldsymbol{X}}_y \hat{\boldsymbol{\Gamma}}_n \hat{\boldsymbol{X}}_y^H &= \hat{\boldsymbol{X}}_a \hat{\boldsymbol{\Gamma}}_a \hat{\boldsymbol{X}}_a^H + \boldsymbol{I}, \\ &= \hat{\boldsymbol{X}}_a \left(\hat{\boldsymbol{\Gamma}}_a + \boldsymbol{I} \right) \hat{\boldsymbol{X}}_a^H. \end{aligned}$$

At this step, the eigenvalues higher than 1 are associated to the signal subspace and those equal to 1 are associated to the noise subspace.

❹ Un-whiten the estimated signal CSM:

$$\boldsymbol{S}_{aa} = \boldsymbol{B}_n^{-H} \hat{\boldsymbol{S}}_{aa} \boldsymbol{B}_n^{-1}.$$

An application of this method is proposed in the section dedicated to the application on inflight measurements, namely Sec. 4.2.

1.5 Diagonal reconstruction

As discussed earlier, it is assumed that the noise correlation length is smaller than the microphone interspacings, which means that the measurement CSM can be written as:

$$\hat{\boldsymbol{S}}_{yy} \approx \boldsymbol{S}_{aa} + \lceil \boldsymbol{\sigma}_n^2 \rfloor. \tag{1.5.1}$$

In this section, we describe three methods from the aeroacoustic literature used to reduce the self-induced noise concentrated on the diagonal of the measurement CSM. These methods all propose to minimize the diagonal elements, while keeping the denoised CSM positive semi-definite, which can be formulated as follows :

$$\begin{aligned} &\text{maximize } \left\| \boldsymbol{\sigma}_n^2 \right\|_1, \\ &\text{subject to } \hat{\boldsymbol{S}}_{yy} - \lceil \boldsymbol{\sigma}_n^2 \rfloor \geq 0, \end{aligned} \tag{1.5.2}$$

where $\| \cdot \|_1$ is the ℓ_1 norm. Each method solves this problem differently.

1.5.1 Solved with convex optimization

Hald (2017) directly uses semi-definite programming to solve this problem, more specifically the SDPT3 solver from CVX Matlab toolbox (Grant and Boyd, 2014, 2008). This solver is an interior-point algorithm suitable for such conic optimization problems (Tütüncü et al., 2003).

1.5.2 Solved with linear optimization

Dougherty (2016) restates the problem of Eq. (1.5.2) as the following linear programming problem, solved iteratively:

$$\begin{aligned} &\text{maximize } \left\| \boldsymbol{\sigma}_{n_{(k)}}^2 \right\|_1, \\ &\text{subject to } \boldsymbol{V}_{(k-1)}^H \left(\hat{\boldsymbol{S}}_{yy} - \lceil \boldsymbol{\sigma}_n^2 \rfloor_{(k)} \right) \boldsymbol{V}_{(k-1)} \geq 0, \end{aligned} \tag{1.5.3}$$

at the k^{th} iteration. $\boldsymbol{V}_{(k-1)}$ are the eigenvectors of $\hat{\boldsymbol{S}}_{yy} - \lceil \boldsymbol{\sigma}_n^2 \rfloor_{(1,\dots,k-1)}$, concatenated from the $k-1$ previous iterations. This problem is later solved using the dual-simplex algorithm from the Matlab *linprog* function.

The concatenation of the eigenvectors increases the problem dimension – and therefore the calculation time – at each iteration. Consequently, the convergence can be very slow and the final denoised CSM may not be semi-positive definite.

1.5.3 Solved with alternating projections

The minimization problem given by Eq. (1.5.2) can also be solved by an Alternating Projections algorithm, as proposed by Leclère et al. (2015). In this case, Alternating Projections aims at finding the intersection between 2 convex sets that are the positive semi-definite matrices (*i.e.* non-negativity of eigenvalues) and the matrices with the same extra-diagonal elements as the measurement CSM. For the sake of clarity, Alg. 1 is the pseudo-code of this procedure. The iterations are performed until the smallest eigenvalues reach a given tolerance threshold.

Algorithm 1 Alternating Projections

Require: $\hat{\boldsymbol{S}}_{yy}$

▷ set diagonal to zero

$\bar{\boldsymbol{S}}_{yy_{(0)}} := \hat{\boldsymbol{S}}_{yy} - \mathrm{diag}\left(\hat{\boldsymbol{S}}_{yy}\right)$

for k **do**

▷ computes eigenvalues and eigenvectors :

$\boldsymbol{s}_{(k)} := \mathrm{eigenvalues}(\boldsymbol{S}_{yy_{(k)}})$

$\boldsymbol{V}_{(k)} := \mathrm{eigenvectors}(\boldsymbol{S}_{yy_{(k)}})$

▷ set negative eigenvalues to zero :

$\boldsymbol{s}_{(k)} := \boldsymbol{s}^{+}_{(k)}$

▷ inject in measurement CSM :

$\hat{\boldsymbol{S}}_{yy_{(k+1)}} := \bar{\boldsymbol{S}}_{yy_{(0)}} + \left\lceil \mathrm{diag}\left(\boldsymbol{V}^{H}_{(k)}\, \mathrm{diag}\left(\boldsymbol{s}_{(k)}\right) \boldsymbol{V}_{(k)}\right)\right\rfloor$

end for

Return: updated $\hat{\boldsymbol{S}}_{yy}$

1.5.4 Comparison on numerical simulations

The three diagonal reconstruction methods solve a very similar problem. In order to see if they provide comparable results, let us apply them on a numerical test case. This test case explores different properties of the CSMs to be denoised, namely noise level, rank of the signal CSM (*i.e.* the number of statistically independent acoustic sources) and number of snapshots. The CSMs are numerically simulated through the procedure described in the following section.

1.5.4.1 Description of the test case

The way CSMs are simulated is inspired by a benchmark case from the aeroacoustic context, described in Sarradj et al. (2017) and studied by Hald (2019). A line of free-field acoustic monopoles with spectra $\boldsymbol{q}$ radiates up to a circular array, which

can be expressed as the linear system $\boldsymbol{a} = \boldsymbol{H}\boldsymbol{q}$, using the following Green's functions:

$$\boldsymbol{H}_{mn} = \frac{\mathrm{e}^{-\imath k \|\boldsymbol{r}_m - \boldsymbol{r}_n\|_2}}{4\pi \|\boldsymbol{r}_m - \boldsymbol{r}_n\|_2}, \tag{1.5.4}$$

with k being the acoustic wavenumber $\frac{2\pi f}{c_0}$ and $\boldsymbol{r}_m$ the coordinate vector for the location of the microphone m. The location of the sources and receivers is represented on Fig. 1.6.

Source spectra are independently drawn from a centered complex Gaussian distribution, with common variance σ_q^2 :

$$[\boldsymbol{q}_j] = \mathcal{N}_{\mathbb{C}}\left(0, \sigma_q^2 \boldsymbol{I}_K\right), \tag{1.5.5}$$

where j refers to the realization number and K is the number of uncorrelated sources.

An independent Gaussian noise is then added to each signal $\boldsymbol{a}$ (see Eq. (1.1.1)):

$$\begin{aligned} &[\boldsymbol{n}_j] = \mathcal{N}_{\mathbb{C}}\left(0, \lceil \boldsymbol{\sigma}_n^2 \rfloor\right), \\ &\text{with } \boldsymbol{\sigma}_n^2 = \mathrm{diag}\left(\sigma_q^2 \boldsymbol{H}\boldsymbol{H}^H\right) 10^{-\mathrm{SNR}/10}. \end{aligned} \tag{1.5.6}$$

And finally, the CSM of measurements is estimated using the CSM estimates of Eq. (1.1.3) and the CSM without noise is also estimated in the same way: $\hat{\boldsymbol{S}}_{aa} = \frac{1}{N_s}\sum_{i=1}^{N_s} \boldsymbol{a}_i \boldsymbol{a}_i^H$. The objective of the denoising process is to recover this last quantity. The deviation of the denoised CSM (written $\tilde{\boldsymbol{S}}_{aa}$) from the noise-free simulation is evaluated looking at the reconstruction error of the diagonal elements, given by:

$$\delta = \frac{\left\|\mathrm{diag}\left(\hat{\boldsymbol{S}}_{aa}\right) - \mathrm{diag}\left(\tilde{\boldsymbol{S}}_{aa}\right)\right\|_2}{\left\|\mathrm{diag}\left(\hat{\boldsymbol{S}}_{aa}\right)\right\|_2}, \tag{1.5.7}$$

where $\mathrm{diag}(\boldsymbol{A})$ is the vector containing the diagonal elements of $\boldsymbol{A}$ and $\|\cdot\|_2$ is the ℓ_2 norm.

This reconstruction error is investigated for each denoising method and for varying parameters of the simulation :

- the rank of the signal matrix $\boldsymbol{S}_{aa}$, given by the number of uncorrelated monopoles,
- the noise level, given by an SNR varying from -10 to 10 dB,
- the number of snapshots N_s from 10 to 5×10^4.

When a parameter is varied, the others remain constant, given by the default values from Tab. 1.1.

Parameter	Default value
Frequency (invariant)	$f = 15$ kHz
Sound velocity (inv.)	340 m/s
Number of receivers (inv.)	$M = 93$
Number of monopoles	$K = 20$
SNR	SNR=10 dB
Number of snapshots	$N_s = 10^4$

Table 1.1: Default values for the numerical simulations.

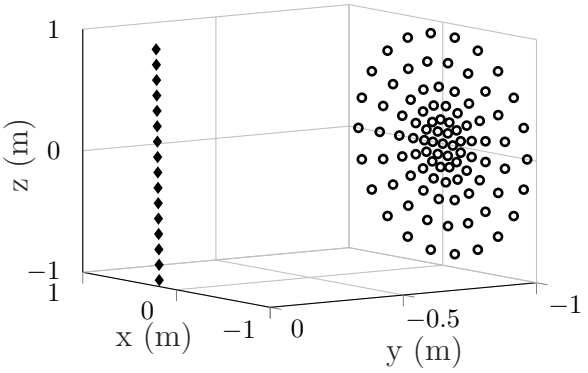

Figure 1.6: Receiver (○) and source (♦) positions for acoustic field simulations, inspired by Sarradj et al. (2017)

1.5.4.2 Results

For the three diagonal reconstruction methods, a rough estimation of the computing time is given in Tab. 1.2. The computing time for Alternating Projection highly depends on the level of the tolerance threshold for the smallest eigenvalues. Concerning Linear optimization, the dimension of the problem increases at each iteration and thus provide rather high computing time compared to the convex optimization solver.

Denoising method	Acronym	Computing time
Convex optimization	DRec	1 sec
Linear optimization	-	60 sec
Alternating projections	-	3 sec

Table 1.2: List of the diagonal reconstruction methods and their approximate computing time to denoise one 93×93 CSM, using non-optimized Matlab codes on a laptop.

For each method, the error curves are given in Fig. 1.7, as a function of the rank of the signal CSM (a), the noise level (b) and the number of snapshots (c).

As expected, when no denoising is applied, the error is given by the opposite value

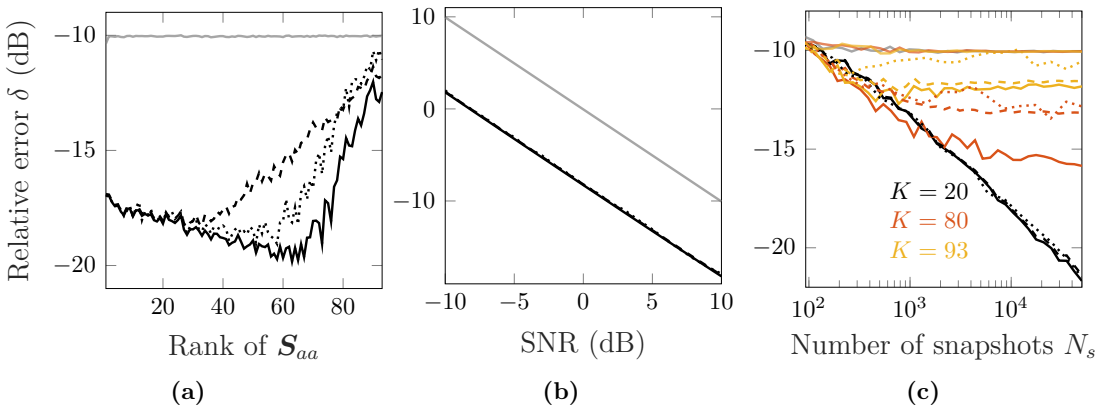

Figure 1.7: Relative reconstruction error of the diagonal terms of the signal CSM, as a function of the number of sources (a), SNR (b) and the number of snapshots (c). The diagonal reconstruction methods are : Alternating Projections (- - -), linear optimization (·····), convex optimization (——), no denoising (——).

of the SNR. The performance of each method mainly differs regarding the signal rank. As shown in Hald (2017), the error increases suddenly when the rank of the signal CSM is too high for the problem to remain identifiable. Convex optimization is less sensible to the increase of the number of sources, thanks to its faster convergence.

For 20 sources, sensitivity to noise level is the same for all the methods, and the error decreases linearly with an increasing SNR, and the same behavior is observed for a logarithmic increase of the number of snapshots.

As convex optimization runs faster and provides a more accurate denoising, it is used for comparison with the other methods in the next chapter, referred to in the following as Diagonal Reconstruction (DRec).

1.6 Robust Principal Component Analysis

Another strategy to solve Prob. 1 is to use two particular properties of $\boldsymbol{S}_{aa}$ and $\boldsymbol{S}_{nn}$, namely, low-rankness and sparsity.

From an experimental point of view, the number of acquisition channels in recent systems has been rapidly increasing. It is common nowadays to take measurements with a large number of simultaneously acquired signals, leading to high-dimensional data. Thus, in many practical situations, the number of independent sources of interest is much lower than the number of measurement channels, which justifies the assumption of a low-rank model to cross-spectral matrices in acoustics.

The use of a sparse model for a CSM of uncorrelated noise has been discussed in the introductive Sec. 1.1.3: the CSM tends to be diagonal when the number

of snapshots tends to infinity. Thus, when the number of channels is large, the noise CSM may be approximated by a sparse matrix, since the number of non-zero diagonal elements is much less than the null off-diagonal ones.

Finally, the decomposition of the CSM in sparse and low-rank matrices can be written as the following optimization problem :

$$\begin{aligned} &\text{minimize } \left\|\hat{\boldsymbol{S}}_{aa}\right\|_* + \lambda \left\|\hat{\boldsymbol{S}}_{nn}\right\|_1, \\ &\text{subject to } \hat{\boldsymbol{S}}_{aa} + \hat{\boldsymbol{S}}_{nn} = \hat{\boldsymbol{S}}_{yy}. \end{aligned} \tag{1.6.1}$$

The nuclear norm $\|\cdot\|_*$ (sum of the eigenvalues) and the ℓ_1 norm ($\|\boldsymbol{A}\|_1 = \sum_{ij} |\boldsymbol{A}_{ij}|$) are convex relaxations of low rank and sparsity constraints, respectively. The trade-off between sparsity of the noise and low-rankness of the source CSM is handled by the regularization parameter λ.

This procedure, known as Robust Principal Component Analysis (RPCA), has been used by Finez et al. (2015) and Amailland et al. (2018) to denoise aeroacoustic and hydroacoustic data. It falls in the category of the so-called "low-rank and sparse matrix decompositions", that can be written under different optimization problem and solved using various solvers (Bouwmans et al., 2016). It finds many applications in image processing, and especially video-surveillance. Thereofre, a collection of algorithms can be found to solve this convex problem. For example, the reader can refer to the LRSLibrary Sobral et al. (2015); Sobral in which the Accelerated Proximal Gradient algorithm, developed by Wright et al. (2009), is used for the denoising applications of the present thesis.

Selection of the regularization parameter

The trade-off parameter λ has to be chosen appropriately given that it may impact greatly the solution. According to Wright et al. (2009) and Candès et al. (2011), a constant parameter equal to $M^{-\frac{1}{2}}$ can be chosen as far as the rank of the signal matrix is reasonably low. As shown by Amailland (2017), this parameter is not always accurate but it is far easier to implement than a trade-off curve analysis. As shown on Fig. 1.8, the trade-off curve is very oscillating and its use can be thorny since it has several maximum curvature points.

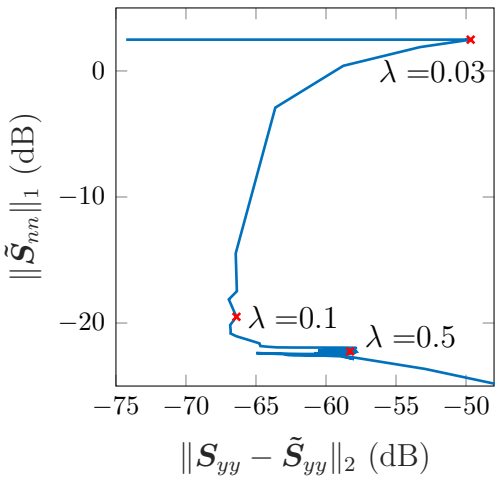

Figure 1.8: Trade-off curve as a function of λ (for default values from Tab. 1.1).

Another solution is to choose the regularization parameter that minimizes the reconstruction error $\|\tilde{\boldsymbol{S}}_{yy} - \boldsymbol{S}_{yy}\|_2$, excluding the case where $\tilde{\boldsymbol{S}}_{nn}$ is null. In Fig. 1.9, this regularization parameter is compared to Wright's ($M^{-\frac{1}{2}}$) and to the optimal regularization parameter that gives the smallest relative error (unknown on non-synthetic case).

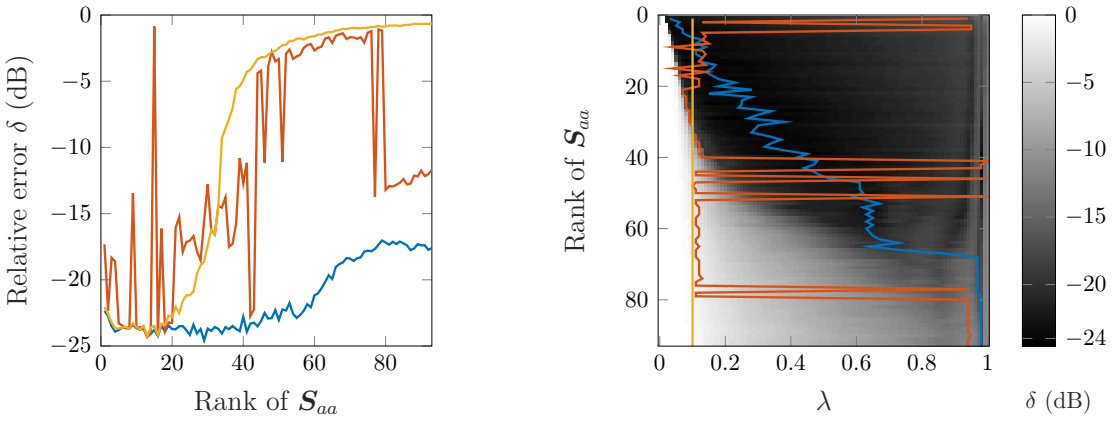

Figure 1.9: Error δ on the reconstructed diagonal solving RPCA as a function of the rank of the signal matrix, for three selection methods for the regularization parameter λ: optimal (—), minimize reconstruction error (—) and $M^{-\frac{1}{2}} = 0.1$ (—).
(b) Lines highlight the value of the regularization parameter for each selection method and their associated errors, depending on the rank of the signal matrix.

On Fig. 1.9b, the gray-scale map corresponds to the relative error as a function of the rank of the signal matrix and the regularization parameter. From this map one can see that the optimal λ (given by the blue curve) has to increase with the rank of $\boldsymbol{S}_{aa}$, in order to maintain a balance in Eq. (1.6.1). That is why a constant

λ gives good results only for very low rank of $\boldsymbol{S}_{aa}$. The regularization parameter that minimizes the reconstruction error gives a very unstable solution mostly far from the optimal solution.
In general, RPCA performances highly depend on the choice for λ and it is essential to find an appropriate way to set this parameter, for any configuration.

1.7 Canonical coherence denoising

The use of Canonical Coherence Analysis (CCA) to denoise the measurement CSM in a context of aeroacoustic measurements has been introduced recently by Hald (2019). The principle of CCA is to find the linear combination of two subgroups of sensors with the highest mutual correlation. The vector of pressure measurements $\boldsymbol{p}_j$ at the j^{th} snapshot is divided into two sub-sets $\boldsymbol{x}_j$ and $\boldsymbol{y}_j$ of I and J channels, with $M = I + J$, such that

$$\boldsymbol{x}_j = \boldsymbol{L}_x \boldsymbol{c}_j + \boldsymbol{n}_{x_j} \quad \text{and} \quad \boldsymbol{y}_j = \boldsymbol{L}_y \boldsymbol{c}_j + \boldsymbol{n}_{y_j}, \tag{1.7.1}$$

with $\boldsymbol{c}_j$ a vector of N uncorrelated equivalent sources, where $N \leq \min(I, J)$. Setting $\mathbb{E}\{\boldsymbol{c}\boldsymbol{c}^H\} = \boldsymbol{I}_N$ (with $\boldsymbol{I}_N$ the identity matrix of dimension N), without loss of generality since matrices $\boldsymbol{L}_x$ and $\boldsymbol{L}_y$ can always be defined accordingly, one has

$$\begin{aligned} \boldsymbol{S}_{xx} &= \boldsymbol{L}_x \boldsymbol{L}_x^H + \mathbb{E}\{\boldsymbol{n}_x \boldsymbol{n}_x^H\}, \\ \boldsymbol{S}_{yy} &= \boldsymbol{L}_y \boldsymbol{L}_y^H + \mathbb{E}\{\boldsymbol{n}_y \boldsymbol{n}_y^H\}, \\ \boldsymbol{S}_{xy} &= \boldsymbol{L}_x \boldsymbol{L}_y^H. \end{aligned} \tag{1.7.2}$$

The last equation shows that noise is canceled if it is uncorrelated between the two groups x and y. This gives hope to get estimates of the factors $\boldsymbol{L}_x$ and $\boldsymbol{L}_y$, say $\hat{\boldsymbol{L}}_x$ and $\hat{\boldsymbol{L}}_y$, from the measurement CSM $\hat{\boldsymbol{S}}_{xy}$. If so, the signal CSM can in turn be estimated as

$$\hat{\boldsymbol{S}}_{aa} = \begin{pmatrix} \hat{\boldsymbol{L}}_x \\ \hat{\boldsymbol{L}}_y \end{pmatrix} \begin{pmatrix} \hat{\boldsymbol{L}}_x \\ \hat{\boldsymbol{L}}_y \end{pmatrix}^H. \tag{1.7.3}$$

Estimates of the factors are obtained from a generalized singular value decomposition (GSVD)

$$\hat{\boldsymbol{S}}_{xy} = \tilde{\boldsymbol{U}} \boldsymbol{\Sigma} \tilde{\boldsymbol{V}}^H, \tag{1.7.4}$$

where $\tilde{\boldsymbol{U}} = \hat{\boldsymbol{S}}_{xx}^{1/2} \boldsymbol{U}$ and $\tilde{\boldsymbol{V}} = \hat{\boldsymbol{S}}_{yy}^{1/2} \boldsymbol{V}$ and with $\boldsymbol{U}$ and $\boldsymbol{V}$ the left and right singular vectors of $\hat{\boldsymbol{S}}_{xx}^{-1/2} \hat{\boldsymbol{S}}_{xy} \hat{\boldsymbol{S}}_{yy}^{-1/2}$, respectively. Upon truncating the GSVD to its N leading

singular values,

$$\hat{\boldsymbol{L}}_x = \tilde{\boldsymbol{U}}_N \boldsymbol{\Sigma}_N^{1/2} \quad \text{and} \quad \hat{\boldsymbol{L}}_y = \tilde{\boldsymbol{V}}_N \boldsymbol{\Sigma}_N^{1/2}, \tag{1.7.5}$$

where $\tilde{\boldsymbol{U}}_N$ (resp. $\tilde{\boldsymbol{V}}_N$) stands for the matrix containing the corresponding N "leading" left (resp. right) singular vectors, the complete denoised CSM reads

$$\tilde{\boldsymbol{S}}_{aa} = \begin{pmatrix} \hat{\boldsymbol{S}}_{xx}^{1/2} \boldsymbol{U}_N \boldsymbol{\Sigma}_N^{1/2} \\ \hat{\boldsymbol{S}}_{yy}^{1/2} \boldsymbol{V}_N \boldsymbol{\Sigma}_N^{1/2} \end{pmatrix} \begin{pmatrix} \hat{\boldsymbol{S}}_{xx}^{1/2} \boldsymbol{U}_N \boldsymbol{\Sigma}_N^{1/2} \\ \hat{\boldsymbol{S}}_{yy}^{1/2} \boldsymbol{V}_N \boldsymbol{\Sigma}_N^{1/2} \end{pmatrix}^H. \tag{1.7.6}$$

The thresholding of the singular values proposed in Hald (2019) is empirical.

The classical CCA is not able to extract a number of canonical components that is higher than the number of channels in the smallest subgroup, which is a limitation to represent a high number of uncorrelated sources. Therefore, Hald proposed to overcome this limitation by performing several CCA iteratively with different sub-groups, on the residuals of the denoised matrix from the previous iteration. However, the number of iterations has to be adapted to the number of sources in the acoustical field. An idea of the procedure is given in Alg. 2.

Algorithm 2 Canonical Coherences

Require: $\boldsymbol{S}_{xx}, \boldsymbol{S}_{yy}, \boldsymbol{S}_{xy}$ for two sub-arrays

$\boldsymbol{K} := \boldsymbol{S}_{xx}^{-1/2} \boldsymbol{S}_{xy} \boldsymbol{S}_{yy}^{-1/2}$

▷ perform a singular value decomposition of $\boldsymbol{K}$

$\boldsymbol{K} := \boldsymbol{U} \boldsymbol{\Sigma} \boldsymbol{V}^H$

▷ thresholding of the canonical coherences

$\boldsymbol{\Sigma}_{ij} = 0$ if $\boldsymbol{\Sigma}_{ij} < \sigma_{\text{thres}}$

▷ computes the canonical components

$\boldsymbol{P} = \boldsymbol{S}_{xx}^{1/2} \boldsymbol{U} \boldsymbol{\Sigma}^{1/2}$

$\boldsymbol{Q} = \boldsymbol{S}_{yy}^{1/2} \boldsymbol{V} \boldsymbol{\Sigma}^{1/2}$

▷ built the denoised CSM

$$\boldsymbol{S}_{aa} = \begin{pmatrix} \boldsymbol{P}\boldsymbol{P}^H & \boldsymbol{P}\boldsymbol{Q}^H \\ \boldsymbol{Q}\boldsymbol{P}^H & \boldsymbol{Q}\boldsymbol{Q}^H \end{pmatrix}$$

Repeat: *For other sub-arrays, depending on the number of significant canonical coherences*

Return: $\boldsymbol{S}_{aa}$

1.8 Conclusion

This chapter offers an overview of some methods of the literature for the denoising of the CSM in the framework of multi-sensor acoustic measurements. The historical methods presented first show some limitations: the diagonal removal induces a loss of amplitude information, whereas the wavenumber filtering requires a high spatial sampling, which is not adapted to measurements for acoustic source localization.

Three diagonal reconstruction methods have been investigated, giving comparable results and with the advantage of not having input parameters to set. However, they show some limitations in terms of denoising performance, especially when the rank of the acoustic CSM is low.

One way to improve the denoising for low-rank signal CSM is to add a low-rankness constrain within the denoising optimization problem, which is done by the RPCA approach. Many penalized versions of CCA also exist, some of which induces a decomposition of the CSM into a reduced number of components (see works in genetics such as Witten et al. (2009)). This falls in the vast literature of the penalized matrix decomposition, which also includes many sparsity-constrained extensions of the PCA problems. A review of these problems is given in Zou and Xue (2018).

However, these optimization problems need to be regularized, either by knowing in advance the number of independent components in the signal, or by tuning regularization parameters. They can also be written within a Bayesian framework to transpose these regularization techniques into corresponding priors, which is the approach we have adopted in the denoising method subsequently proposed.

2

Cross-spectral matrix decomposition based on Factor Analysis and uncorrelated noise

Contents

2.1 Introduction

In this chapter, a method for separating the acoustic contribution from an uncorrelated noise is proposed. Like many methods in the literature, the proposed method exploits the correlation properties of these two contributions.

The proposed approach is a penalized matrix decomposition, aiming at fitting the measured Cross-Spectral Matrix (CSM) over a structured covariance model, with the following constraints:

- The source matrix is of reduced rank, which is equivalent to describing the acoustic field with a linear combination of a limited number of variables. The acoustic contribution $\boldsymbol{a}$ at the M microphone points can thus be written

$$\boldsymbol{a}_j = \boldsymbol{L}\boldsymbol{c}_j, \tag{2.1.1}$$

  where $\boldsymbol{a}$ and $\boldsymbol{c}$ are Fourier coefficients at a given frequency for each observation j. In this factorization, $\boldsymbol{L}$ is an $M \times \kappa$ complex matrix that relates the data to the vector of complex variables $\boldsymbol{c}$.

- The structure of the noise CSM is diagonal. This constraint does not account for a correlated noise model but has the advantage of strongly constraining the problem to ensure a proper identifiability. This reads

$$\boldsymbol{S}_{nn} = \lceil \boldsymbol{\sigma}_n^2 \rfloor. \tag{2.1.2}$$

Therefore, under the assumption that the acoustic and noise are mutually independent, the model for the total measured pressure field is

$$\boldsymbol{S}_{yy} = \boldsymbol{L}\boldsymbol{S}_{cc}\boldsymbol{L}^H + \lceil \boldsymbol{\sigma}_n^2 \rfloor, \tag{2.1.3}$$

which gives the following matrix representation:

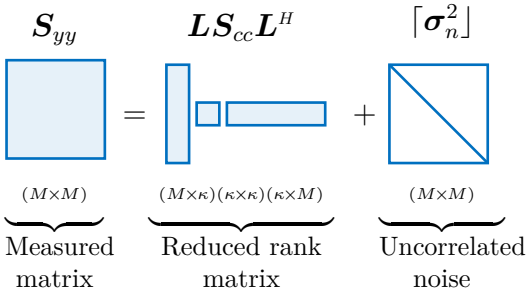

For zero-mean observations, this model is that of the statistical method called Factor Analysis (FA) (Bartholomew et al., 2011). It is very close to the Principal Component Analysis (PCA) model, with the main difference being that the PCA model is based on an isotropic noise model, which means that its covariance is proportional to the identity: $\lceil \boldsymbol{\sigma}_n^2 \rfloor = \sigma_n^2 \boldsymbol{I}_M$ (Tipping and Bishop, 1999).

FA falls into the category of the latent variable models. The idea of a latent variable model is to describe some data of dimension M (in our case the number of measurement points) with a reduced number of unobserved factors. By imposing an uncorrelated noise model, the latent factors are thus intended to describe the correlation structure of the data. Latent variable models are studied since the beginning of the 20$^{\text{th}}$ century, for applications in social science and econometrics (for an historical overview, see Bartholomew et al. (2011), p. 12–17). Yet, this kind of matrix factorization problems is still topical, and has received a renewed interest for the development of recommender system of on-line commercial applications or social networks (Mehta and Rana, 2017).

The FA model is particularly suitable for the denoising of CSMs because, as shown in the present chapter, it can be solved using only the CSM form of the data. Moreover, this method does not require any knowledge about the nature of the sources or an acoustic propagation model. Therefore, the denoising problem is solved in a rather small dimension space, since it does not make use of a source map (which generally contains a number of source points much higher than the number of sensors). Moreover, this inverse problem can be solved using a Bayesian approach, which provides a suitable context for taking into account the a priori level of knowledge of the problem. The Bayesian framework being flexible, it is easily possible to move away from the classic FA model to adapt more precisely to the separation issue in aeroacoustics.

In this chapter, the probabilistic framework of the factor analysis model is first detailed. Then, a first approach to solve the inference problem is described, using an Expectation-Maximization (EM) procedure, written for CSM data. However, as EM has no guaranty to converge toward the global optimum, the problem is then formulated in a Bayesian way, which offers global optimization solvers, among which the Gibbs sampler is selected. In order to regularize the problem, the model is rephrased to promote a sparse solution. Finally, an acceleration of the optimization process is proposed through a marginalization of the Gibbs sampler and some numerical experiments are finally carried out, to compare the proposed approach with some methods of the literature.

2.2 The Factor Analysis model

2.2.1 Probabilistic modeling of the direct problem

In the classical FA model, the latent variables are supposed to be independent, with a distribution given by a centered unit-covariance Gaussian:

$$[\boldsymbol{c}_j] = \mathcal{N}_{\mathbb{C}}\left(\mathbf{0}, \boldsymbol{I}_\kappa\right). \tag{2.2.1}$$

The notation $\mathcal{N}_{\mathbb{C}}(\boldsymbol{\mu}, \boldsymbol{\Omega})$ refers to the multivariate complex normal distribution with mean $\boldsymbol{\mu}$ and covariance matrix $\boldsymbol{\Omega}$. The Identity form of the latent variables covariance matrix is not a limitation here, since different gains may be affected through the mixing matrix coefficients.

According to the Central Limit Theorem, the random noise is also supposed to be centered Gaussian, with a variance which may vary from one microphone to another:

$$[\boldsymbol{n}] = \mathcal{N}_{\mathbb{C}}(\mathbf{0}, \lceil \boldsymbol{\sigma}_n^2 \rfloor). \tag{2.2.2}$$

It then follows that the likelihood is also Gaussian,

$$[\boldsymbol{y}_j \mid \infty] = \mathcal{N}_{\mathbb{C}}\left(\boldsymbol{L}\boldsymbol{c}_j, \lceil \boldsymbol{\sigma}_n^2 \rfloor\right), \tag{2.2.3}$$

where "$\mid \infty$" is to be understood as "conditioned to all the other variables of the model". The unknown parameters $\boldsymbol{L}$ and $\boldsymbol{\sigma}_n^2$ can thus be inferred through a maximum likelihood estimation, or a maximum a posteriori estimation in case of a Bayesian approach.

Note that in general, in the FA model, the mixing matrix and the factors are not uniquely identifiable. However, the product $\boldsymbol{L}\boldsymbol{c}$ is uniquely identifiable, which is sufficient for the denoising application.

In the overall denoising problem Prob. 1, the objective is thus, in a probabilistic framework, to find an estimate of the conditional random variable $\boldsymbol{S}_{aa} \mid \hat{\boldsymbol{S}}_{yy}$.

2.2.2 Sparse representation

First of all, let us introduce the notion of sparsity. In the present thesis, the term "sparsity" refers to a sparsity known as *weak* (Starck et al., 2010, p. 3). It means that one can consider as sparse a description of the data with a number M of atoms, whose coefficients decrease very rapidly and which is thus very well represented by a few κ-largest coefficients (the $M - \kappa$ others being negligible but not necessarily null).

In the FA model, κ is not directly inferred. It must therefore be a priori chosen and it is not certain that in case of overestimation, the optimization converges

towards a sparse solution. The sparsity of the model acts as a regularization, and therefore the choice of this number is important. It should not be too small (*i.e.* less than the true number K of components of the acoustic field) nor too large to avoid over-fitting. In other words, κ should be the optimal number of factors which reasonably describes the data, and for which the data is less well described with $\kappa - 1$ factors and not significantly better described with $\kappa + 1$ factors. This is what is subsequently referred to as a sparse solution.

The choice of this number can be left to the discretion of the user, if she/he has a good knowledge of the acoustic field, and some selection strategies can also be implemented. For example, it is possible to take successive values for κ in turn and then see what value is more appropriate in term of likelihood ratio (Bishop, 1999). The difficulty of this approach is to find a trade-off between the model order and the goodness of fit. Otherwise, many criteria exist in the literature to estimate the optimal number of factors, based on this trade-off (Minka, 2001; Preacher et al., 2013; Bouveyron et al., 2019).

In the present work, the strategy to avoid over-fitting is based on a Bayesian approach. It is shown hereafter that using Markov Chain Monte Carlo (MCMC) computational tools, a Bayesian model-based approach is able to automatically select the dimensionality that best fit the acoustic subspace.

2.2.3 Bayesian hierarchical inference

In Bayesian inference, all the parameter of a fitting model are seen as random variables to which are associated probability laws before any measurements. These Probability Density Function (PDF) are called priors. The goal of the Bayesian inference is to find the parameter set $\boldsymbol{\Theta}$ that has the highest joint probability knowing the measured data, called posterior probability, that is:

$$\boldsymbol{\Theta}^{\star} = \operatorname{argmax} \left[\boldsymbol{\Theta} \mid \hat{\boldsymbol{S}}_{yy} \right], \tag{2.2.4}$$

where $[x \mid y]$ stands for the conditional PDF of x given y. $\hat{\boldsymbol{S}}_{yy}$ is an estimate of the measurement CSM obtained from a limited number of snapshots. From the Bayes' rule, the unknown posterior distribution in Eq. (2.2.4) can be written from two known quantities: the likelihood of the measured data and the prior functions. This reads

$$[\boldsymbol{\Theta} \mid \hat{\boldsymbol{S}}_{yy}] \propto [\boldsymbol{\Theta}][\hat{\boldsymbol{S}}_{yy} \mid \boldsymbol{\Theta}]. \tag{2.2.5}$$

If this distribution does not have an explicit form, it has to be approximated through numerical methods such as Monte Carlo Markov Chain approaches, which performs

an iterative sampling of each parameter in its own posterior. The parameters which are found to maximize the posterior probability are then called maximum a posteriori estimates.

2.2.4 Hierarchical graphs

The hierarchical relation between all the unknown parameters of the problem can be summarily represented using a graph (Bishop, 2006, chap. 8). On these graphs, the variables of the model are embodied by nodes, linked together by arrows which indicate their hierarchical relationships. The arrows go from nodes called *parents* to nodes called *children*. The parent nodes are variables involved in priors while the child nodes are involved in the likelihood. This graphical representation allows writing the posterior distribution of each parameter, by completing the following Bayes formula:

$$[\theta \mid \infty] \propto \underbrace{[\theta \mid \text{ Parents of } \theta]}_{\text{Prior}} \times \underbrace{\prod_i \left[\text{ i}^{\text{th}} \text{ child of } \theta \mid \text{ Parents of i}^{\text{th}} \text{ child} \right]}_{\text{Likelihood}}. \quad (2.2.6)$$

The graph representing the classical FA model is given in Fig. 2.1. The graphical convention used is the following: the shaded case indicates the observations, the other round circles stand for random variables to be inferred and the constant parameters are denoted without any border. Moreover, squares nodes indicates the density of the variables and the dashed box indicates a duplication of the pattern, called the plate notation (for example, for each snapshot).

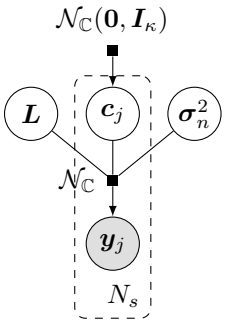

Figure 2.1: Bayesian hierarchical graph for the classical FA model

2.3 Model estimation *via* the EM algorithm

2.3.1 The Expectation-Maximization algorithm

The EM algorithm is a very popular tool used to find maximum a posteriori or maximum likelihood estimators, especially for latent variable models. In the FA model, the objective is to find the maximum likelihood estimates of the parameters $\boldsymbol{L}$ and $\boldsymbol{\sigma}_n^2$, which reads

$$\left(\boldsymbol{L}^\star, \boldsymbol{\sigma}_n^{2\star}\right) = \operatorname{argmax}\left[\boldsymbol{y} \mid \boldsymbol{L}, \boldsymbol{\sigma}_n^2\right]. \tag{2.3.1}$$

This problem could be solved by any classical gradient descent algorithm (see McLachlan and Krishnan (2007), p. 5-7), but the EM algorithm is particularly well-suited for likelihood from the exponential family, as in the present case (see Eq. (2.2.3)).

The idea of EM is to maximize the complete-data (*i.e.* of both the data $\boldsymbol{y}$ and the missing values $\boldsymbol{c}$) log-likelihood, but as it is unobservable, it is replaced by its expectation using the current estimates of the parameters (Bishop, 2006, p. 439-441). This procedure is hereafter developed to find the maximum likelihood estimates of the parameters, using CSM data. The EM algorithm alternates between 2 steps at each iteration i:

❶ **Expectation-step**: Perform the expectation with respect to $[\boldsymbol{c}_j \mid \boldsymbol{y}_j]$ of the complete-data log-likelihood $\mathcal{P}$ (*i.e.* including the missing values $\boldsymbol{c}_j$)

$$\mathbb{E}\left\{\mathcal{P}\right\} = \mathbb{E}\left\{\ln\left(\prod_{j=1}^{N_s}\left[\boldsymbol{y}_j, \boldsymbol{c}_j \mid \boldsymbol{L}, \boldsymbol{\sigma}_n^2\right]\right)\right\}. \tag{2.3.2}$$

where

$$\left[\boldsymbol{y}_j, \boldsymbol{c}_j \mid \boldsymbol{L}, \boldsymbol{\sigma}_n^2\right] = \mathcal{N}_{\mathbb{C}}\left(\boldsymbol{L}\boldsymbol{c}_j, \lceil\boldsymbol{\sigma}_n^2\rfloor\right)\mathcal{N}_{\mathbb{C}}\left(\boldsymbol{0}, \boldsymbol{I}_\kappa\right), \tag{2.3.3}$$

This leads to

$$\begin{aligned}\mathbb{E}\left\{\mathcal{P}\right\} = -\sum_{j=1}^{N_s}\Big(&\ln\left(\det(\lceil\boldsymbol{\sigma}_n^2\rfloor)\right) + \boldsymbol{y}_j^H\lceil\boldsymbol{\sigma}_n^{-2}\rfloor\boldsymbol{y}_j - \mathbb{E}\{\boldsymbol{c}_j\}^H\boldsymbol{L}^H\lceil\boldsymbol{\sigma}_n^{-2}\rfloor\boldsymbol{y}_j \\ &-\boldsymbol{y}_j^H\lceil\boldsymbol{\sigma}_n^{-2}\rfloor\boldsymbol{L}\mathbb{E}\{\boldsymbol{c}_j\} + \operatorname{tr}\Big(\boldsymbol{L}^H\lceil\boldsymbol{\sigma}_n^{-2}\rfloor\boldsymbol{L}\mathbb{E}\{\boldsymbol{c}_j\boldsymbol{c}_j^H\} + \mathbb{E}\{\boldsymbol{c}_j\boldsymbol{c}_j^H\}\Big)\Big).\end{aligned} \tag{2.3.4}$$

At this step, we make use of the posterior distribution of latent variables $[\boldsymbol{c}_j \mid \infty]$ to calculate $\mathbb{E}\{\boldsymbol{c}_j\}$ and $\mathbb{E}\{\boldsymbol{c}_j\boldsymbol{c}_j^H\}$. This posterior is obtained from the

Bayes' rule and Eqs. (2.2.1) and (2.2.3):

$$\begin{aligned}[\boldsymbol{c}_j \mid \boldsymbol{y}_j] &\propto [\boldsymbol{y}_j \mid \infty][\boldsymbol{c}_j], \\ &\propto \mathcal{N}_{\mathbb{C}}\left(\boldsymbol{L}\boldsymbol{c}_j, \lceil \boldsymbol{\sigma}_n^2 \rfloor\right) \mathcal{N}_{\mathbb{C}}\left(\boldsymbol{0}, \boldsymbol{I}_\kappa\right), \\ &\propto \mathcal{N}_{\mathbb{C}}\left(\boldsymbol{\Omega}_c \boldsymbol{L}^H \lceil \boldsymbol{\sigma}_n^{-2} \rfloor \boldsymbol{y}_j, \boldsymbol{\Omega}_c\right), \\ \text{with } \boldsymbol{\Omega}_c &= \left(\boldsymbol{I}_\kappa + \boldsymbol{L}^H \lceil \boldsymbol{\sigma}_n^{-2} \rfloor \boldsymbol{L}\right)^{-1}. \end{aligned} \tag{2.3.5}$$

This gives the following statistics, in which the parameters $\boldsymbol{L}$ and $\boldsymbol{\sigma}_n^2$ are replaced by their estimates from the previous iteration:

$$\mathbb{E}\{\boldsymbol{c}_j\} = \boldsymbol{B}\boldsymbol{y}_j \tag{2.3.6}$$

$$\text{and} \quad \mathbb{E}\left\{\boldsymbol{c}_j \boldsymbol{c}_j^H\right\} = \text{var}(\boldsymbol{c}) + \mathbb{E}\{\boldsymbol{c}_j\}\mathbb{E}\{\boldsymbol{c}_j\}^H = \boldsymbol{\Omega}_c + \boldsymbol{B}\boldsymbol{y}_j\boldsymbol{y}_j^H\boldsymbol{B}^H, \tag{2.3.7}$$

with $\boldsymbol{B} = \boldsymbol{\Omega}_c \boldsymbol{L}^H \lceil \boldsymbol{\sigma}_n^{-2} \rfloor$.

❷ **Maximization-step**: Find the parameters that maximize the expected value from the previous step:

$$\left(\tilde{\boldsymbol{L}}, \tilde{\boldsymbol{\sigma}}_n^2\right) = \text{argmax}\, \mathbb{E}\left\{\mathcal{P}\right\}. \tag{2.3.8}$$

The updated parameters, written $\tilde{\boldsymbol{L}}$ and $\tilde{\boldsymbol{\sigma}}_n^2$, are thus obtained when the derivative of $\mathbb{E}\left\{\mathcal{P}\right\}$ is null. Using some properties given in Eqs. (B.1.1) to (B.1.4) leads to[1]

$$\frac{\partial \mathbb{E}\left\{\mathcal{P}\right\}}{\partial \boldsymbol{L}} = \sum_{j=1}^{N_s} \left(2\lceil \boldsymbol{\sigma}_n^{-2} \rfloor \boldsymbol{y}_j \mathbb{E}\left\{\boldsymbol{c}_j\right\}^H - \lceil \boldsymbol{\sigma}_n^{-2} \rfloor \boldsymbol{L} \mathbb{E}\{\boldsymbol{c}_j \boldsymbol{c}_j^H\}\right), \tag{2.3.9}$$

$$\frac{\partial \mathbb{E}\left\{\mathcal{P}\right\}}{\partial \boldsymbol{\sigma}_n^{-2}} = \sum_{j=1}^{N_s} \left(\lceil \boldsymbol{\sigma}_n^2 \rfloor - \boldsymbol{y}_j\boldsymbol{y}_j^H + 2\tilde{\boldsymbol{L}}\mathbb{E}\{\boldsymbol{c}_j\}\boldsymbol{y}_j^H - \tilde{\boldsymbol{L}}\mathbb{E}\{\boldsymbol{c}_j\boldsymbol{c}_j^H\}^H\tilde{\boldsymbol{L}}^H\right). \tag{2.3.10}$$

and using the expression of $\mathbb{E}\{\boldsymbol{c}_j\}$ and $\mathbb{E}\{\boldsymbol{c}_j\boldsymbol{c}_j^H\}$ in Eqs. (2.3.6) and (2.3.7) provides the updated parameters:

$$\tilde{\boldsymbol{L}} = \hat{\boldsymbol{S}}_{yy}\boldsymbol{B}^H \left(\boldsymbol{\Omega}_c + \boldsymbol{B}\hat{\boldsymbol{S}}_{yy}\boldsymbol{B}^H\right)^{-1}, \tag{2.3.11}$$

$$\tilde{\boldsymbol{\sigma}}_n^2 = \text{diag}\left(\left(\boldsymbol{I}_M - \tilde{\boldsymbol{L}}\boldsymbol{B}\right)\hat{\boldsymbol{S}}_{yy}\left(\boldsymbol{I}_M - \tilde{\boldsymbol{L}}\boldsymbol{B}\right)^H + \tilde{\boldsymbol{L}}\boldsymbol{\Omega}_c\tilde{\boldsymbol{L}}^H\right). \tag{2.3.12}$$

The reader can also refer to the section 12.2.4 of Bishop (2006) for detailed calculations and implementation of the EM algorithm for FA.

The pseudo-code for this procedure is given in Alg. 3.

[1] since $\boldsymbol{\sigma}_n^2 \neq 0$, $\frac{\partial \mathbb{E}\{\mathcal{P}\}}{\partial \boldsymbol{\sigma}_n^{-2}} = 0$ is equivalent to $\frac{\partial \mathbb{E}\{\mathcal{P}\}}{\partial \boldsymbol{\sigma}_n^2} = 0$

Algorithm 3 FA solved with EM

Initialization: $\boldsymbol{L}_0,\ \boldsymbol{\sigma}^2_{n_0}\ \boldsymbol{S}_{cc_0}$

Require: $\hat{\boldsymbol{S}}_{yy},\ \kappa,\ i_{max},\ \epsilon$

for i **do**

Estimation of $\boldsymbol{S}_{cc_i}$ using Eq. (2.3.7)

Estimation of $\boldsymbol{L}_i$ using Eq. (2.3.11)

Estimation of $\boldsymbol{\sigma}^2_{n_i}$ using Eq. (2.3.12)

▷ Convergence criteria

if $i \geq i_{max}$ **or** $\|\boldsymbol{\sigma}^2_{n_i} - \boldsymbol{\sigma}^2_{n_{i-1}}\|_2 / \|\boldsymbol{\sigma}^2_{n_{i-1}}\|_2 \leq \epsilon$ **then**

Stop

end if

end for

return $\boldsymbol{L}_i,\ \boldsymbol{S}_{cc_i},\ \boldsymbol{\sigma}^2_{n_i}$

It can be shown that iteratively maximizing $\mathcal{P}$ using the current estimates of $\boldsymbol{L}$ and $\boldsymbol{\sigma}^2_n$ is equivalent to improving the marginal likelihood $[\boldsymbol{y} \mid \boldsymbol{L}, \boldsymbol{\sigma}^2_n]$ (see for example Bishop (2006), p. 450-454). The EM algorithm can be used only if the joint distribution $[\boldsymbol{y}_j, \boldsymbol{c}_j \mid \boldsymbol{L}, \boldsymbol{\sigma}^2_n]$ has a known closed form, which is the case for the present model. The main drawback of this procedure, is that if this distribution is multimodal, the EM algorithm may converge toward a local maximum. Multiple strategies exist to avoid this situation, e.g. performing several EM iterations with different random initializations.

At the end of the EM procedure, $\mathbb{E}\{\boldsymbol{c}_j \boldsymbol{c}_j^H\}$ can be used as an estimator of $\tilde{\boldsymbol{S}}_{cc}$. The denoised matrix is then $\tilde{\boldsymbol{L}}\tilde{\boldsymbol{S}}_{cc}\tilde{\boldsymbol{L}}^H$ ($\tilde{\boldsymbol{L}}$ being the last estimation of $\boldsymbol{L}$), which is positive by construction.

2.3.2 Numerical validation

In order to assess the implementation of the EM algorithm and evaluate its characteristics, some simple numerical experiment are lead. A measurement CSM is generated by solving the direct problem described in Sec. 2.2. The chosen constants for the simulation are:

- number of sensors: $M = 30$,
- number of components for the acoustic field: $K = 5$,
- number of snapshots: $N_s = 10^4$,
- and the Signal-to-Noise Ratio (SNR) is 10 dB.

The EM algorithm is then applied to the simulated noisy CSM. Note that for the present toy case, the computation time is very small (less than one second on a laptop). To evaluate the denoising performance of EM, two indicators are studied.

First, the likelihood marginalized with respect to the factors, $[\boldsymbol{y}_j \mid \boldsymbol{L}, \boldsymbol{\sigma}_n^2]$, which is what EM is supposed to maximize. Its expression is

$$[\boldsymbol{y}_j \mid \infty_{-c_j}] = \mathcal{N}_{\mathbb{C}}(\boldsymbol{0}, \boldsymbol{B}) \quad \text{with} \quad \boldsymbol{B} = \boldsymbol{L}\boldsymbol{L}^H + \lceil \boldsymbol{\sigma}_n^2 \rfloor, \tag{2.3.13}$$

where "$\mid \infty_{-x}$" indicates "conditioned to all the other variables except x". This result is obtained by completing squares in the exponential, as demonstrated in appendix C.1.

Then, the deviation of the denoised CSM (written $\tilde{\boldsymbol{S}}_{aa}$) from the noise-free simulation is evaluated looking at the normalized Root Mean Square Error (RMSE), given by

$$\text{Normalized RMSE} = \frac{\|\boldsymbol{S}_{aa} - \tilde{\boldsymbol{S}}_{aa}\|_F}{\|\boldsymbol{S}_{aa}\|_F}, \tag{2.3.14}$$

where $\|\boldsymbol{A}\|_F$ is the Frobenius norm of $\boldsymbol{A}$ $(= \sqrt{\sum_{ij} \boldsymbol{A}_{ij}^2})$.

These two indicators are plotted for each iteration of the EM algorithm, for three different number of input factors in the model, written κ (whereas the number of simulated independent components in the acoustic field remains $K = 5$).

2.3.2.1 Initialization of the EM algorithm

Since EM may converge into a local optimum, many starting values have been tested for the parameter set $\{\boldsymbol{L}_0, \boldsymbol{\sigma}_{n_0}^2\}$, and only two of them are presented in this section, in order to illustrate the typical influence of the initialization on the EM algorithm.

A first initial parameter set is obtained from a Sub-Space Identification (SSI) approach. After performing an eigenvalue decomposition of the data CSM , the κ highest eigenvalues $\boldsymbol{\lambda}_{1:\kappa}$ and associated eigenvectors $\boldsymbol{U}_{1:\kappa}$ are used to build $\boldsymbol{\lambda}_0 = \boldsymbol{U}_{1:\kappa}\left\lceil \boldsymbol{\lambda}_{1:\kappa}^{1/2} \right\rfloor$, and in a same way, the noise variance is obtained from the remaining eigencomponents: $\boldsymbol{\sigma}_{n_0}^2 = \operatorname{diag}\left(\boldsymbol{U}_{\kappa+1:M} \lceil \boldsymbol{\lambda}_{\kappa+1:M} \rfloor \boldsymbol{U}_{\kappa+1:M}^H\right)$.

The second initial parameter set is simply assigned a very small value: $\boldsymbol{L}_0, \boldsymbol{\sigma}_{n_0}^2 = 10^{-16}$. Note that for the EM algorithm, setting both parameters to exactly zero would prevent the new parameters from being updated.

2.3.2.2 Results

The corresponding log-likelihood and RMSE are given in Figs. 2.2 and 2.3, for the two initialization strategies and three different number of factors κ.

In order to illustrate some aspects of the optimization procedure, a minimum number of iterations is set at 50. As expected, the log-likelihood increases continuously, which partially validates the algorithm. However, it increases in steps. A

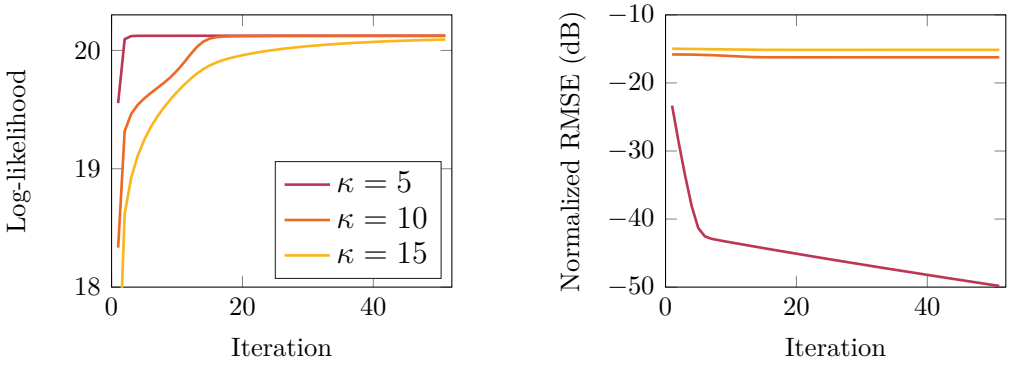

(a) Log-likelihood **(b)** Normalized RMSE

Figure 2.2: Likelihood and RMSE indicators at each iteration of the EM procedure, starting from $\boldsymbol{L}_0, \boldsymbol{\sigma}^2_{n_0}$ obtained with SSI.

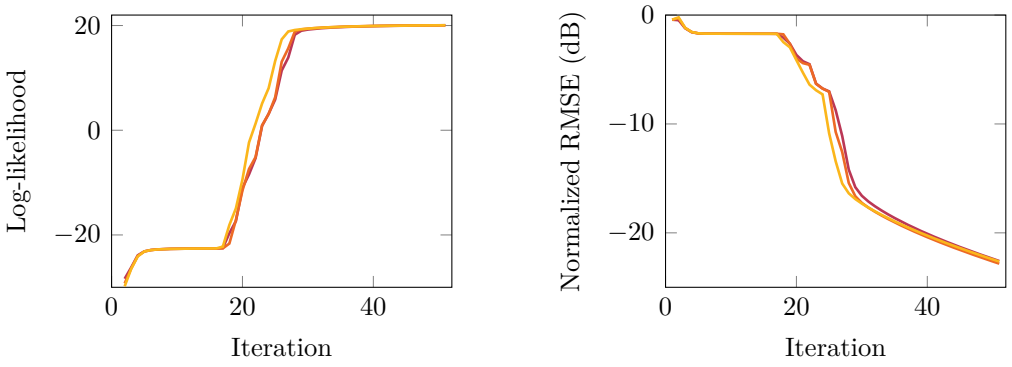

(a) Log-likelihood **(b)** Normalized RMSE

Figure 2.3: Likelihood and RMSE indicators at each iteration of the EM procedure, starting from $\boldsymbol{L}_0, \boldsymbol{\sigma}^2_{n_0} = 10^{-16}$.

stopping criterion for the algorithm is the evolution rate of the $\boldsymbol{\sigma}^2_n$ parameter, which corresponds indirectly to the evolution of the likelihood. Therefore, it is very likely to stop at the first step, depending on the chosen tolerance threshold. For example, for the parameters initialized at zero, with a threshold at 10^{-3}, the algorithm should have stopped around iteration 10, which corresponds to a RMSE of -2 dB.

In general, these figures also illustrate the fact that EM converges to a local maximum and therefore gives different results depending on the initialization. Initialize with a small value gives a slower log-likelihood growth, but a more certain decrease in terms of RMSE. This empirical observation has also been checked on many other numerical and experimental applications.

To complement the analysis, the log-likelihood and the RMSE for the two initializations are plotted in Fig. 2.4 as a function of the chosen number of components in the model κ, while the simulated number of independent sources

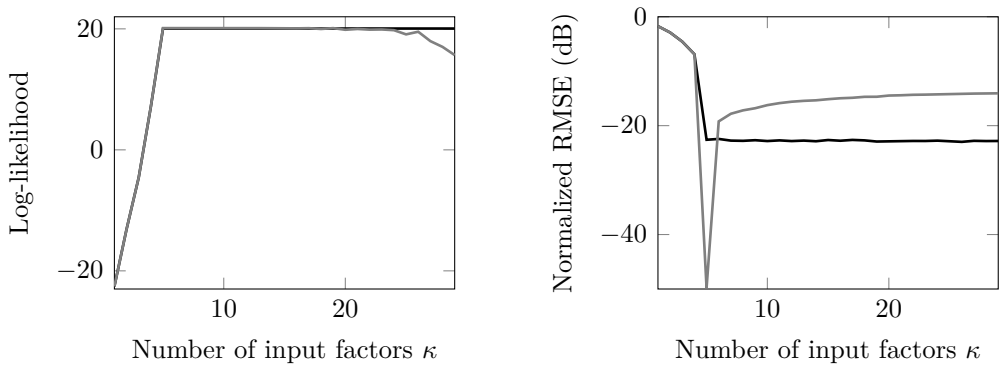

(a) Log-likelihood **(b)** Normalized RMSE

Figure 2.4: RMSE of the reconstructed acoustic CSM, as a function of the assumed number of factors in the FA model. The number of independent components used to simulate the baseline CSM is 5. The initial parameter set is obtained from SSI (—) and very small (—).

is kept to $K = 5$.

From this figure, it is visible that the SSI initialization provides very degraded performance in term of RMSE when the number of components is overestimated. In contrast, the initialization near zero is not really sensitive to the increase of κ. From this figure, it is also clear that the minimal number of factors which maximizes the likelihood is 5 for the two initializations, which is thus a way to determine the optimal number of factors that gives the sparsest solution, as shown in Bishop (1999).

2.4 Model estimation *via* the Gibbs sampler

In order to overcome the limitations of the EM solver, a Bayesian approach is then adopted. If offers a flexible framework to take into account the uncertainties on each parameter of the model, and the regularization of the problem is consequently done through the choice of the priors.

The use of MCMC numerical solvers offers the possibility of an easy modification of the FA model, which is convenient for an extension that accounts for a correlated noise, such as in chapter 3. Among the MCMC methods, the Gibbs sampler is chosen for the present application, due to its simplicity of implementation and its versatility. It also comes with some guarantees of global convergence.

2.4.1 Sparse model

In Bayesian inference, all the parameters are seen as random variables and are assigned a prior PDF. The design of these priors is a key step of the model design.

For the reasons given previously (see Sec. 2.2.2), the model detailed in the following is chosen to promote the sparsity of the solution.

In a Baysesian framework, one way to enforce the sparsity is to choose priors that promote sparsity. In the FA model, these sparse priors has to be chosen in order to encourage the smallest factors to reach zero. Therefore, they can concern the factor variance, the mixing matrix $\boldsymbol{L}$ or even the Singular Value Decomposition (SVD) of $\boldsymbol{L}$ as in Minka (2001). The strategy adopted in this work is to weight each factor with a variable which itself has a prior promoting sparsity. These weights are stored in a diagonal matrix $\lceil \boldsymbol{q} \rfloor$, and the extended FA model is then

$$\boldsymbol{y}_j = \boldsymbol{L}\lceil \boldsymbol{q} \rfloor \boldsymbol{c}_j + \boldsymbol{n}_j. \tag{2.4.1}$$

In this section, the FA model is first developed in a Bayesian framework. Then, the weighting strategy for sparsity is detailed. An implementation of the numerical solver for the inference problem is then provided, which is a Gibbs sampler. And finally, an acceleration of the convergence of this sampler is proposed through a collapsed Gibbs sampler.

2.4.1.1 Parameter priors

In Bayesian inference, all the sought parameters are assigned a prior distribution and the parameter of these priors (called hyperparameters) may also be considered as unknowns of the problem and then be assigned their own prior (called hyperpriors).

The choice of the priors is important since it plays the role of regularization of the inverse problem. It can be motivated by a physical or experimental knowledge of the problem. Depending on the confidence given to the data or the model, some priors can be chosen in order to give more weight to either the data or prior during the optimization.

If a prior distribution is chosen to have a heavier tail[2] than the likelihood, this means that the prior will be less sensitive to the outliers and the model will give more weight to the data. This strategy has to be adopted when there is more confidence in the data than in the priors. On the contrary, if a physical phenomenon is very well described, this can be used to design prior with thinner tails (compared to the likelihood's one), which will be robust with respect to the data – *i.e.* the solution will be more driven by the priors. Finally, between these two strategies, when the data and the prior are thought to be pretty in agreement, the conjugate priors are commonly used – a prior is said conjugated for the likelihood if it is such that the posterior and the prior are in the same PDF family.

[2] *i.e.* with a slower decrease

According to the Central Limit theorem applied to Fourier coefficients, the likelihood function of the measured data tends to be Gaussian, which reads

$$[\boldsymbol{y}_j \mid \infty] = \mathcal{N}_{\mathbb{C}}\left(\boldsymbol{L}\lceil \boldsymbol{q} \rfloor \boldsymbol{c}_j, \lceil \boldsymbol{\sigma}_n^2 \rfloor\right), \tag{2.4.2}$$

for the j^{th} measurement at a given frequency. As for the classical FA model, the noise is modeled by M centered Gaussian variables with a diagonal covariance matrix:

$$[\boldsymbol{n}] = \mathcal{N}_{\mathbb{C}}\left(\boldsymbol{0}, \lceil \boldsymbol{\sigma}_n^2 \rfloor\right). \tag{2.4.3}$$

The variance of the noise $\boldsymbol{\sigma}_n^2$ being unknown, it is assigned its own PDF. An inverse-gamma law (written $\mathcal{IG}$) is chosen due to its positive support and its conjugacy with the Gaussian which also provides an algebraic convenience (it gives a closed-form expression for the posterior):

$$[\boldsymbol{\sigma}_n^2] = \mathcal{IG}(\boldsymbol{a}_n, \boldsymbol{b}_n). \tag{2.4.4}$$

This prior is also convenient because its shape and scale parameters can be easily tuned to specify different levels of prior information, from very precise to very vague. This is a classical choice for variance parameters (see Gelman et al. (2014), p.42-43).

In FA, no physical interpretation can be made about the mixing matrix $\boldsymbol{L}$. Therefore, for simplicity, it is assigned a centered complex Gaussian, with a normalized variance, such that the energy of the signal part is only driven by the factors:

$$[\boldsymbol{L}] = \mathcal{N}_{\mathbb{C}}\left(\boldsymbol{0}, \frac{\boldsymbol{I}_{M\kappa}}{\kappa}\right). \tag{2.4.5}$$

The factors are supposed to be a priori independent and heteroscedastic, *i.e.* each factor has its own variance

$$[\boldsymbol{c}] = \mathcal{N}_{\mathbb{C}}(\boldsymbol{0}, \lceil \boldsymbol{\gamma}^2 \rfloor). \tag{2.4.6}$$

The choice for heteroscedasticity of the factors is motivated by the fact that it is prompt to provide sparse solution, as shown in Antoni et al. (2019). It is equivalent to a mixture of Gaussians with different variances following inverse Gamma laws, which is known to generate a Student-t marginal distribution for the factors $\boldsymbol{c}$ (see Bishop (2006), p.102-103).

As for the noise variance, an inverse-gamma distribution is chosen for the factor variances $\boldsymbol{\gamma}^2$:

$$[\boldsymbol{\gamma}^2] = \mathcal{IG}(\boldsymbol{a}_\gamma, \boldsymbol{b}_\gamma). \tag{2.4.7}$$

2.4.1.2 Bernoullian prior for the factor weights

The objective of the factor loading is to induce sparsity of the factors by that of the weight vector $\boldsymbol{q}$.

Many heavy-tailed priors are known to induce sparsity, such as the Student-t or the Laplace distribution. However, a strong sparsity constrain can also be induced by the use of a Bernoullian prior, which is analogous to a minimization constrain over a ℓ_0-norm, which is the number of non-zero elements. This prior is for example employed by Faure (2017) and Ge et al. (2011) for comparable models.

Sampled from a Bernoullian process, the κ weights $\boldsymbol{q}$ can only take two values, 0 or 1:

$$[\boldsymbol{q}] = \mathcal{B}ern(l). \tag{2.4.8}$$

Depending on the level of sparsity, they thus switch off or on a certain number of factors. The level of sparsity is driven by the hyperparameter l, that is also inferred, based on a Beta prior, which is conjugated with the Bernoullian distribution:

$$[l] = \mathcal{B}eta(a_l, b_l). \tag{2.4.9}$$

This model for FA is very close to those refer to as Beta-Bernoulli process in the literature (Zhou et al., 2011; Dang, 2016), used for model order selection.

The sampling of the binaries $\boldsymbol{q}$ is implemented through an acceptance-rejection step, which determines whether the model order is updated (the details of this step are given in Sec. 2.4.2.1. This procedure is very similar to a reversible jump MCMC used in Lopes and West (2004), that treats the number of factors as a parameter of the model and allows jumping between models of different dimensionality through an acceptance-rejection procedure.

In Dinsenmeyer et al. (2020), the weights are assigned an exponential prior instead of a Bernoullian one, which is equivalent to a mixture of Gaussians with different variances exponentially distributed, leading to a Laplace distribution for the product $\lceil \boldsymbol{q} \rfloor \boldsymbol{c}$ (Eltoft et al., 2006). The results presented afterwards show no difference between the two models, nevertheless, the Bernoullian prior on the weights presents some advantages over the exponential one. First, as the weights are either 1 or 0, they do not carry any variance information. Therefore, it avoids some scale ambiguity with the factors (see Sec. 2.4.2.2) that may harm the convergence of the sampler. Moreover, the initialization is more intuitive since it only represents a number of supposed uncorrelated sources. Also, the prior on the sparsity can easily be tuned through the l parameter.

The overall graph for this model is given in Fig. 2.5.

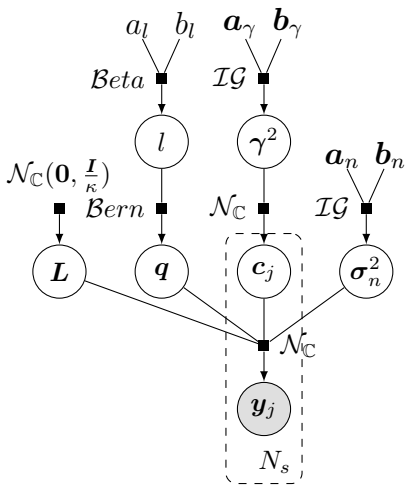

Figure 2.5: Hierarchical graphs for the sparse FA model.

2.4.2 Implementation of the Gibbs sampler

The inference problem is solved by maximizing the full posterior density:

$$\boldsymbol{L}^\star, \boldsymbol{q}^\star, \boldsymbol{S}_{cc}^\star, \boldsymbol{\sigma}^{2\star}, \boldsymbol{\gamma}^{2\star}, l^\star = \arg\max \left[\boldsymbol{L}, \boldsymbol{q}, \boldsymbol{S}_{cc}, \boldsymbol{\sigma}^2, \boldsymbol{\gamma}^2, l \mid \hat{\boldsymbol{S}}_{yy} \right] \tag{2.4.10}$$

As this posterior has no closed-form expression, it is evaluated from the univariate posterior distribution of each parameter, using a Gibbs sampler. The Gibbs sampler is used to draw random samples from a target joint distribution without using its explicit expression, which may be unknown. The principle is to sample iteratively each random variable from its own distribution conditioned on the current values of the other variables (which has to be known). For each parameter, a chain is built from a fixed number N_{run} of samples. It can be shown that the stationary distribution converges toward the sought joint distribution (Gelman et al., 2014). A generic pseudo-code for the Gibbs sampler is given in Alg. 4 performed over N_{run} iterations over an arbitrary set of parameters $\boldsymbol{\Theta}$.

Algorithm 4 Generic Gibbs sampler

Initialization: $\boldsymbol{\theta}_0$
  for $i = 1$ to N_{run} **do**
    for θ in $\boldsymbol{\Theta}$ **do**
      sample θ_i in $[\theta \mid$ all the other variables$]$ (see Eq. (2.2.6))
    end for
  end for
return Posterior distributions of all the θ in $\boldsymbol{\Theta}$

In order to denoise the CSM data, the posterior used in the Gibbs sampler have to be written accordingly. The same approach as in Antoni et al. (2019) is

followed, and therefore, the CSM of the factor is directly sampled in block from the multivariate posterior. The blocking strategy is also known to improve the mixing of the Markov chains and thus the convergence of the sampler, compared to an iterative univariate sampling, especially when there is a strong correlation between the concerned variables (Brown et al., 2019).

The counter-part of the block sampling is the manipulation (and especially inversion) of large covariance matrices. For the present application, the covariance matrices which have to be inverted are of size $M \times M$, which is reasonable (M being the number of sensors). A block updating strategy is also adopted for the sampling of the mixing matrix $\boldsymbol{L}$, which requires the inversion of an $M\kappa \times M\kappa$ matrix. However, this inversion is cheap since this matrix is (band) sparse.

The Gibbs sampler version used for the present denoising problem is given in Alg. 5 and the needed posterior distributions are detailed in the next section.

Algorithm 5 FA solved with the Gibbs sampler

Initialization: $\boldsymbol{L}_0,\ \boldsymbol{\sigma}_{n_0}^2,\ \boldsymbol{\gamma}_0^2,\ \boldsymbol{q}_0$

Require: $\hat{\boldsymbol{S}}_{yy}, \kappa,\ \boldsymbol{a}_\gamma,\ \boldsymbol{b}_\gamma,\ \boldsymbol{a}_n,\ \boldsymbol{b}_n,\ a_l, b_l,\ N_{\text{run}}$

for $i = 1, \ldots, N_{\text{run}}$ **do**

Sample $\boldsymbol{S}_{cc_i}$ following Eq. (2.4.15)

Sample $\boldsymbol{L}_i$ in Eq. (2.4.17)

Sample $\boldsymbol{\gamma}_i^2$ in Eq. (2.4.20)

Sample l in Eq. (2.4.26)

Sample $\boldsymbol{q}_i$ in Eq. (2.4.25)

Sample $\boldsymbol{\sigma}_{n_i}^2$ in Eq. (2.4.21)

end for

return Posterior PDFs of $\boldsymbol{S}_{cc},\ \boldsymbol{L},\ \boldsymbol{\sigma}_n^2,\ \boldsymbol{\gamma}^2,\ \boldsymbol{q}$

2.4.2.1 Posterior distributions for sampling

From the model described previously, the posterior distribution for each unknown parameter has to be computed using the Bayes' rule in Eq. (2.2.6), in order to implement the Gibbs sampler.

Sampling of $\boldsymbol{S}_{cc}$

From the expressions of the likelihood Eq. (2.4.2) and the prior in Eq. (2.4.6), the posterior of the factors $\boldsymbol{c}$ is:

$$\begin{aligned}[\boldsymbol{c}_j \mid \infty] &\propto [\boldsymbol{c}_j][\boldsymbol{y}_j \mid \infty] \\ &\propto \mathcal{N}_{\mathbb{C}}(\boldsymbol{0}, \lceil\boldsymbol{\gamma}^2\rfloor)\mathcal{N}_{\mathbb{C}}\left(\boldsymbol{L}\lceil\boldsymbol{q}\rfloor\boldsymbol{c}_j, \lceil\boldsymbol{\sigma}_n^2\rfloor\right) \end{aligned} \tag{2.4.11}$$

Using the multiplication rule of Gaussians (see for example Ahrendt (2005)) directly gives

$$[\boldsymbol{c}_j \mid \infty] \propto \mathcal{N}_{\mathbb{C}}\left(\boldsymbol{\mu}_{c_j}, \boldsymbol{\Omega}_c\right) \tag{2.4.12}$$

$$\begin{aligned} \text{with} \quad & \boldsymbol{\Omega}_c = \left(\lceil \boldsymbol{q} \rfloor \boldsymbol{L}^H \lceil \boldsymbol{\sigma}_n^{-2} \rfloor \boldsymbol{L} \lceil \boldsymbol{q} \rfloor + \lceil \boldsymbol{\gamma}^{-2} \rfloor\right)^{-1} \\ \text{and} \quad & \boldsymbol{\mu}_{c_j} = \boldsymbol{\Omega}_c \lceil \boldsymbol{q} \rfloor \boldsymbol{L}^H \lceil \boldsymbol{\sigma}_n^{-2} \rfloor \boldsymbol{y}_j \end{aligned}$$

In order to build a CSM-based Gibbs sampler, the same approach as in Antoni et al. (2019) is followed. As $\boldsymbol{c}_j \mid \infty$ is Gaussian, it can be written

$$\boldsymbol{c}_j \mid \infty = \boldsymbol{\mu}_{c_j} + \boldsymbol{x}_j \quad \text{with} \quad [\boldsymbol{x}_j] = \mathcal{N}_{\mathbb{C}}(\boldsymbol{0}, \boldsymbol{\Omega}_c). \tag{2.4.13}$$

Then,

$$\boldsymbol{S}_{cc} = \frac{1}{N_s}\sum_{j=1}^{N_s} \boldsymbol{\mu}_{c_j}\boldsymbol{\mu}_{c_j}^H + \frac{1}{N_s}\sum_{j=1}^{N_s} \boldsymbol{x}_j\boldsymbol{x}_j^H + \frac{2}{N_s}\sum_{j=1}^{N_s} \boldsymbol{x}_j\boldsymbol{\mu}_{c_j}^H. \tag{2.4.14}$$

Since $\boldsymbol{x}_j$ and $\boldsymbol{\mu}_{c_j}$ are independent random variables, the last terms tends to zero, and then

$$\boldsymbol{S}_{cc} \mid \infty \approx \ \boldsymbol{\Omega}_c \lceil \boldsymbol{q} \rfloor \boldsymbol{L}^H \lceil \boldsymbol{\sigma}_n^{-2} \rfloor \hat{\boldsymbol{S}}_{yy} \lceil \boldsymbol{\sigma}_n^{-2} \rfloor^H \boldsymbol{L} \lceil \boldsymbol{q} \rfloor \boldsymbol{\Omega}_c^H + \frac{1}{N_s}\boldsymbol{W}_c, \tag{2.4.15}$$

where $\boldsymbol{W}_c$ is a random matrix that follows a complex Wishart distribution, with N_s degrees of freedom and variance matrix $\boldsymbol{\Omega}_c$.

Sampling of $\boldsymbol{L}$

The sampling of $\boldsymbol{L}$ is made using a vectorized form of $\boldsymbol{L}$, written $\boldsymbol{\lambda} = \text{vec}(\boldsymbol{L})$. The posterior of $\boldsymbol{\lambda}$ is given by

$$\begin{aligned} [\boldsymbol{\lambda} \mid \infty] &\propto [\boldsymbol{\lambda}] \prod_{j=1}^{N_s} [\boldsymbol{y}_j \mid \infty] \\ &\propto \mathcal{N}_{\mathbb{C}}\left(\boldsymbol{0}, \frac{\boldsymbol{I}_{M\kappa}}{\kappa}\right) \mathcal{N}_{\mathbb{C}}\left(\boldsymbol{L}\lceil \boldsymbol{q} \rfloor \boldsymbol{c}_j, \lceil \boldsymbol{\sigma}_n^2 \rfloor\right). \end{aligned} \tag{2.4.16}$$

Using the fact that

$$\boldsymbol{y}_j = \text{vec}\left(\boldsymbol{L}\lceil \boldsymbol{q} \rfloor \boldsymbol{c}_j\right) + \boldsymbol{n}_j = \left(\lceil \boldsymbol{q} \rfloor \boldsymbol{c}_j^T \otimes \boldsymbol{I}_M\right)\boldsymbol{\lambda} + \boldsymbol{n}_j,$$

and some properties of the Kronecker product $\otimes$ (given appendix B.2) lead to:

$$[\boldsymbol{\lambda} \mid \infty] \propto \mathcal{N}_c(\boldsymbol{\mu}_\lambda, \boldsymbol{\Omega}_\lambda), \tag{2.4.17}$$

$$\begin{aligned} &\text{with} \quad \boldsymbol{\Omega}_\lambda^{-1} = (\lceil \boldsymbol{q} \rfloor \boldsymbol{S}_{cc}^* \lceil \boldsymbol{q} \rfloor) \otimes \lceil \boldsymbol{\sigma}_n^{-2} \rfloor + \kappa \boldsymbol{I}_{M\kappa} \\ &\text{and} \quad \boldsymbol{\mu}_\lambda = \boldsymbol{\Omega}_\lambda \operatorname{vec}(\lceil \boldsymbol{\sigma}_n^{-2} \rfloor \boldsymbol{S}_{yc} \lceil \boldsymbol{q} \rfloor). \end{aligned}$$

where $\cdot^*$ is the conjugate operator. Note that $\boldsymbol{\Omega}_\lambda^{-1}$ is sparse, which can be taken into account to reduce the numerical cost of its inversion. In this last equation, $\boldsymbol{S}_{yc}$ is estimated using the same decomposition of $\boldsymbol{c}_j$ as before (see Eq. (2.4.13)),

$$\begin{aligned} \boldsymbol{S}_{yc} &= \frac{1}{N_s} \sum_{j=1}^{N_s} \boldsymbol{y}_j \boldsymbol{\mu}_{c_j}^H + \frac{1}{N_s} \sum_{j=1}^{N_s} \boldsymbol{y}_j \boldsymbol{x}_j^H \\ &\approx \hat{\boldsymbol{S}}_{yy} \lceil \boldsymbol{\sigma}_n^{-2} \rfloor \boldsymbol{L} \lceil \boldsymbol{q} \rfloor \boldsymbol{\Omega}_c^H. \end{aligned} \tag{2.4.18}$$

Sampling of $\boldsymbol{\gamma}^2$

Still using the Bayes' rule (see Eq. (2.2.6)), the posterior for the k$^{\text{th}}$element in the vector $\boldsymbol{\gamma}^2$ can be written as follows:

$$\begin{aligned} [\boldsymbol{\gamma}_k^2 \mid \infty] &\propto [\boldsymbol{\gamma}_k^2] \prod_{j=1}^{N_s} [\boldsymbol{c}_j \mid \boldsymbol{\gamma}_k^2], \\ &\propto \mathcal{IG}(\boldsymbol{a}_\gamma, \boldsymbol{b}_\gamma) \prod_{j=1}^{N_s} \mathcal{N}_{\mathbb{C}}(\boldsymbol{0}, \lceil \boldsymbol{\gamma}^2 \rfloor). \end{aligned} \tag{2.4.19}$$

The use of the conjugacy of the inverse-gamma with the Gaussian directly gives the expression of the posterior:

$$[\boldsymbol{\gamma}_k^2 \mid \infty] \propto \mathcal{IG}(\boldsymbol{a}_{\gamma_k} + N_s, \boldsymbol{b}_{\gamma_k} + \boldsymbol{S}_{cc_{kk}}). \tag{2.4.20}$$

Sampling of $\boldsymbol{\sigma}_n^2$

From the inverse-gamma prior assigned to $\boldsymbol{\sigma}_n^2$ and the Gaussian likelihood function,

$$\begin{aligned} [\boldsymbol{\sigma}_n^2 \mid \infty] &\propto [\boldsymbol{\sigma}_n^2] \prod_{j=1}^{N_s} [\boldsymbol{y}_j \mid \infty], \\ &\propto \mathcal{IG}(\boldsymbol{a}_n, \boldsymbol{b}_n) \prod_{j=1}^{N_s} \mathcal{N}_{\mathbb{C}}(\boldsymbol{L} \lceil \boldsymbol{q} \rfloor \boldsymbol{c}_j, \lceil \boldsymbol{\sigma}_n^2 \rfloor), \end{aligned} \tag{2.4.21}$$

the conjugacy of the inverse-gamma with the Gaussian directly gives the expression of the posterior:

$$[\boldsymbol{\sigma}_{n_m}^2 \mid \infty] \propto \mathcal{IG}(\boldsymbol{a}_{n_m} + N_s, \boldsymbol{b}_{n_m} + \boldsymbol{T}_{mm}), \quad m = 1, \ldots, M, \tag{2.4.22}$$

$$\text{where} \quad \boldsymbol{T} = \frac{1}{N_s}\sum_{j=1}^{N_s}\left(\boldsymbol{y}_j - \boldsymbol{L}\lceil\boldsymbol{q}\rfloor\boldsymbol{c}_j\right)\left(\boldsymbol{p}_j - \boldsymbol{L}\lceil\boldsymbol{q}\rfloor\boldsymbol{c}_j\right)^H,$$
$$= \hat{\boldsymbol{S}}_{yy} + \boldsymbol{L}\lceil\boldsymbol{q}\rfloor\boldsymbol{S}_{cc}\lceil\boldsymbol{q}\rfloor\boldsymbol{L}^H - \boldsymbol{S}_{yc}\lceil\boldsymbol{q}\rfloor\boldsymbol{L}^H - \boldsymbol{L}\lceil\boldsymbol{q}\rfloor\boldsymbol{S}_{cy}.$$

Making use of the expression of $\boldsymbol{S}_{yc}$ given in Eq. (2.4.18) and replacing $\boldsymbol{S}_{cc}$ by its expression given in Eq. (2.4.15) gives

$$\boldsymbol{T} = (\boldsymbol{I}_M - \boldsymbol{B})\hat{\boldsymbol{S}}_{yy}(\boldsymbol{I}_M - \boldsymbol{B}) + \frac{1}{N_s}\boldsymbol{L}\lceil\boldsymbol{q}\rfloor\boldsymbol{W}_c\lceil\boldsymbol{q}\rfloor\boldsymbol{L}^H \tag{2.4.23}$$

$$\text{where} \quad \boldsymbol{B} = \boldsymbol{L}\lceil\boldsymbol{q}\rfloor\boldsymbol{\Omega}_c\lceil\boldsymbol{q}\rfloor\boldsymbol{L}^H\lceil\boldsymbol{\sigma}_n^{-2}\rfloor = \boldsymbol{B}^H. \tag{2.4.24}$$

By doing so, it is visible that the semi-positivity of $\boldsymbol{T}$ is ensured.

Sampling of $\boldsymbol{q}$

The Bernoullian prior for the binary weights $\boldsymbol{q}$ leads to the following posterior:

$$\begin{aligned}
[\boldsymbol{q}_k|\infty] &\propto [\boldsymbol{q}_k]\prod_j [\boldsymbol{y}_j|\boldsymbol{q}_k,\infty], \\
&\propto l^{\boldsymbol{q}_k}(1-l)^{1-\boldsymbol{q}_k}\mathrm{e}^{-\sum_j(\boldsymbol{y}_j-\boldsymbol{L}\lceil\boldsymbol{q}\rfloor\boldsymbol{c}_j)^H\lceil\boldsymbol{\sigma}_n^{-2}\rfloor(\boldsymbol{y}_j-\boldsymbol{L}\lceil\boldsymbol{q}\rfloor\boldsymbol{c}_j)}, \\
&\propto \mathrm{e}^{-\mathrm{tr}\left(\lceil\boldsymbol{\sigma}_n^{-2}\rfloor\boldsymbol{T}(\boldsymbol{q}_k)\right)-\boldsymbol{q}_k\ln\left(\frac{1}{l}-1\right)}, \\
&\propto \mathrm{e}^{-g(\boldsymbol{q}_k)},
\end{aligned}$$

where $\boldsymbol{T}$ is given by Eq. (2.4.23). The state of a binary $\boldsymbol{q}_k$ is changed by adding $\delta_k = (-1)^{\boldsymbol{q}_k}$. The binary $\boldsymbol{q}_k$ with a modified state is thus written $\boldsymbol{q}_{k_{\mathrm{mod}}} = \boldsymbol{q}_k + \delta_k$. The probability that a binary changes its state is:

$$\begin{aligned}
[\boldsymbol{q}_{k_{\mathrm{mod}}}|\infty] &\propto [\boldsymbol{q}_{k_{\mathrm{mod}}}]\prod_j [\boldsymbol{y}_j|\boldsymbol{q}_{k_{\mathrm{mod}}},\infty] \\
&\propto \mathrm{e}^{-\mathrm{tr}\left(\lceil\boldsymbol{\sigma}_n^{-2}\rfloor\boldsymbol{T}(\boldsymbol{q}_{k_{\mathrm{mod}}})\right)-\boldsymbol{q}_{k_{\mathrm{mod}}}\ln\left(\frac{1}{l}-1\right)} \\
&\propto \mathrm{e}^{-g(\boldsymbol{q}_{k_{\mathrm{mod}}})}.
\end{aligned}$$

These two probabilities have to be normalized in order to have a sum equal to 1. The probability that a binary changes its state becomes:

$$\begin{aligned}
[\boldsymbol{q}_{k_{\mathrm{mod}}}|\infty] &= \frac{\mathrm{e}^{-g(\boldsymbol{q}_{k_{\mathrm{mod}}})}}{\mathrm{e}^{-g(\boldsymbol{q}_{k_{\mathrm{mod}}})} + \mathrm{e}^{-g(\boldsymbol{q}_k)}} \\
&= \frac{1}{1+\mathrm{e}^{-\left(g(\boldsymbol{q}_k)-g(\boldsymbol{q}_{k_{\mathrm{mod}}})\right)}}
\end{aligned} \tag{2.4.25}$$

The sampling is then performed through an acceptance-rejection procedure. A sample $t \sim \mathcal{U}(0,1)$ is compared to $[\boldsymbol{q}_{k_{\mathrm{mod}}} \mid \infty]$. If the sample t is lower, the change

of state is accepted. Otherwise, the binary keeps its current state. In practice, as $\boldsymbol{T}$ can be high (especially if N_s is high), it is numerically safer to implement an acceptation of the change of state through the equivalent comparison:

$$-\ln\left(\frac{1}{t}-1\right) < g(\boldsymbol{q}_k) - g(\boldsymbol{q}_{k_{\text{mod}}}).$$

Sampling of l

The posterior for the sparsity parameter l arises from the use of the conjugacy of the Beta distribution with the Bernoullian:

$$\begin{aligned}
[l \mid \boldsymbol{q}] &\propto [l] \prod_{k=1}^{\kappa} [\boldsymbol{q}_k \mid \infty], \\
&\propto \mathcal{B}eta(a_l, b_l) \prod_{k}^{\kappa} \mathcal{B}ern(l), \\
&\propto \frac{\Gamma(a_l+b_l)}{\Gamma(a_l)\Gamma(b_l)} l^{a_l-1}(1-l)^{b_l-1} \prod_{k}^{\kappa} l^{\boldsymbol{q}_k}(1-l)^{1-\boldsymbol{q}_k}, \\
&\propto \mathcal{B}eta\left(a_l + N_q, b_l + \kappa - N_q\right), \qquad (2.4.26)
\end{aligned}$$

where $N_q = \sum_{k=1}^{\kappa} \boldsymbol{q}_k$, which is the number of non-zero binaries.

2.4.2.2 Sampling of a scale parameter

As the $\boldsymbol{L}\lceil\boldsymbol{q}\rfloor\boldsymbol{c}$ decomposition of $\boldsymbol{y}$ is not unique, the parameters $\boldsymbol{L}$ and $\boldsymbol{c}$ can take any value. Therefore, it is hard to check the convergence by looking at those chains. Moreover, it implies that $\boldsymbol{L}$ and $\boldsymbol{c}$ will be correlated, which can induce a bad mixing of the chains and slows down the convergence of the sampler. In general, a scale ambiguity appears for problems written as

$$z = h \star x + b,$$

where $\star$ is any bilinear operator. In this case, for each couple (x, h) and $s \neq 0$, we can write

$$(sx) \star \left(\frac{h}{s}\right) = x \star h.$$

In the FA model, this situation appears for each product $\boldsymbol{L}_k\boldsymbol{c}_k$ if $\boldsymbol{q}_k = 1$. Veit et al. (2008) suggest to sample a scale parameter to remedy this scale ambiguity without modifying the target distribution. We introduce κ scale factors $\boldsymbol{s}_k$, in a diagonal matrix written $\boldsymbol{S} = \lceil\boldsymbol{s}\rfloor$ such that:

$$\boldsymbol{y} = \tilde{\boldsymbol{L}}\lceil\boldsymbol{q}\rfloor\tilde{\boldsymbol{c}} + \boldsymbol{n} = (\boldsymbol{L}\boldsymbol{S}^{-1})\lceil\boldsymbol{q}\rfloor(\boldsymbol{S}\boldsymbol{c}) + \boldsymbol{n}.$$

The calculus details for the posterior of $\boldsymbol{S}$ are given in appendix C.2. The numerical cost added by the sampling of $\boldsymbol{S}$ is small as compared to the sampling of all the other (non-scalar) parameters. The effects of the sampling of these scale parameters is illustrated by a numerical toy case in appendix C.2. It is shown that the scaling is able to increase the mixing of the chains, but this effect becomes negligible at low SNR.

2.4.3 Marginalization of the Gibbs sampler

It is expected that $\boldsymbol{c}$ and $\boldsymbol{q}$ have a highly correlated posterior. This kind of situation generally causes the Gibbs sampler to explore the full posterior with small steps, leading to slow convergence rates. As the joint distribution of $\boldsymbol{q}$ and $\boldsymbol{c}$ is not known, it is not possible to do blocking to improve the convergence. Therefore, it is decided to implement a strategy of partial marginalization of the Gibbs sampler (also called collapsed Gibbs sampler), which is known in the literature to strongly increase the convergence speed (van Dyk and Park, 2011). The idea of the marginalization is to project the joint distribution on one of the variable. By doing so, the posterior distribution is replaced by a posterior conditioned on fewer unknowns and the Gibbs sampler takes larger steps, thereby improving global convergence.

The sampling of $\boldsymbol{q}$ is thus performed in a new posterior, but the overall sampler is not really more complicated. However, it induces an additional cost. As shown in the marginalized posterior given below, $\kappa + 1$ full and complex covariance matrices of size $M \times M$ (κ matrices $\boldsymbol{B}_2(\boldsymbol{q}_{k_{\text{mod}}})$ and one $\boldsymbol{B}_2(\boldsymbol{q})$) have to be inverted. Champagnat et al. (1996) suggest a way to compute the modified inverse matrices $\boldsymbol{B}_2(\boldsymbol{q}_{\text{mod}})^{-1}$ directly from $\boldsymbol{B}_2(\boldsymbol{q})^{-1}$. However, this solution has not been implemented for simplicity, since the number of sensors M is supposed to be relatively small for array denoising application.

Whereas permuting steps of a classical Gibbs sampler does not affect the stationary distribution, Park and Van Dyk (2009) suggest that the order of the draws of the collapsed sampler may sometimes alter the stationary distribution. The collapsed sampling of $\boldsymbol{q} \mid \infty_{-\boldsymbol{c}}$ induces a loss of the correlation structure between $\boldsymbol{q}$ and $\boldsymbol{c}$. Therefore, this correlation has to be restored through the sampling of $\boldsymbol{c} \mid \boldsymbol{q}, \infty$, in order to correctly converge towards the target full posterior. For the present work, several orders for the draws of $\boldsymbol{q}$ and $\boldsymbol{c}$ have been tested, and no significant difference was found from this order in our case. The current order was chosen so as to reduce the number of intermediate quantities that have to be computed.

Sampling of $\boldsymbol{q}$ with marginalization with respect to $\boldsymbol{c}$

The posterior distribution of $\boldsymbol{q}$ marginalized with respect to $\boldsymbol{c}$ is given by

$$[\boldsymbol{q}_k|\infty_{-\boldsymbol{c}}] \propto [\boldsymbol{q}_k] \prod_j [\boldsymbol{y}_j|\infty_{-\boldsymbol{c}}].$$

It can be shown that (following the same calculations as in appendix C.1)

$$[\boldsymbol{y}_j|\infty_{-\boldsymbol{c}}] = \mathcal{N}_c(\boldsymbol{0}, \underbrace{\boldsymbol{L}\lceil \boldsymbol{q} \rfloor \lceil \boldsymbol{\gamma}^2 \rfloor \lceil \boldsymbol{q} \rfloor \boldsymbol{L}^H + \lceil \boldsymbol{\sigma}_n^2 \rfloor}_{\boldsymbol{B}_2}). \tag{2.4.27}$$

Then, the marginalized posterior distribution is

$$\begin{aligned}
[\boldsymbol{q}_k|\infty_{-\boldsymbol{c}}] &\propto l^{\boldsymbol{q}_k}(1-l)^{1-\boldsymbol{q}_k} \frac{\mathrm{e}^{-\sum_j \boldsymbol{y}_j^H \boldsymbol{B}_2(\boldsymbol{q}_k)^{-1}\boldsymbol{y}_j}}{|\boldsymbol{B}_2(\boldsymbol{q}_k)|^{N_s}}, \\
&\propto \mathrm{e}^{-\operatorname{tr}\left(\boldsymbol{B}_2(\boldsymbol{q}_k)^{-1}\hat{\boldsymbol{S}}_{yy}\right) - N_s \ln|\boldsymbol{B}_2(\boldsymbol{q}_k)| - \boldsymbol{q}_k \ln\left(\frac{1}{l}-1\right)}, \\
&\propto \mathrm{e}^{-g(\boldsymbol{q}_k)}.
\end{aligned}$$

As before, the probability that the binary changes its state is

$$\begin{aligned}
[\boldsymbol{q}_{k_{\mathrm{mod}}}|\infty_{-\boldsymbol{c}}] &\propto l^{\boldsymbol{q}_{k_{\mathrm{mod}}}}(1-l)^{1-\boldsymbol{q}_{k_{\mathrm{mod}}}} \frac{\mathrm{e}^{-\sum_j \boldsymbol{y}_j^H \boldsymbol{B}_2(\boldsymbol{q}_{k_{\mathrm{mod}}})^{-1}\boldsymbol{y}_j}}{|\boldsymbol{B}_2(\boldsymbol{q}_{k_{\mathrm{mod}}})|^{N_s}}, \\
&\propto \mathrm{e}^{-g(\boldsymbol{q}_{k_{\mathrm{mod}}})}.
\end{aligned}$$

After normalization of the probability, the change of state for the binary $\boldsymbol{q}_k$ is accepted if

$$-\ln\left(\frac{1}{t}-1\right) < g(\boldsymbol{q}_k) - g(\boldsymbol{q}_{k_{\mathrm{mod}}}).$$

2.4.4 Numerical validation

The same experiment as for the assessment of the EM algorithm is led, for which the model and the data are in perfect accordance. A signal plus noise CSM is simulated solving the FA direct problem, with the same constant ($M = 30$, $K = 5$, $N_s = 10^4$), but with an SNR of -10 dB in order to enhance some characteristics of the MCMC algorithm.

The effect of the heteroscedasticity of the factor in the model is illustrated, as well as the effect of the partial marginalization of the Gibbs sampler. Moreover, some results from the same numerical experiments concerning the effect of the scaling strategy are given in appendix C.2.

2.4.4.1 Initialization and prior parameters

Before running the denoising algorithm, the constant parameters for the priors and hyperpriors have to be set by the user, and all the parameters have to be initialized.

First, all the priors are set very vague (*i.e.* nearly flat PDF):

- a uniform prior for the sparsity is chosen by setting $a_l, b_l = 1$,
- flat priors are set for the factor and for the noise variance, with $\boldsymbol{a}_\gamma, \boldsymbol{b}_\gamma, \boldsymbol{a}_n, \boldsymbol{b}_n = 10^{-4}$.

Even if the Gibbs sampler is supposed to perform global optimization, a proper initialization can lower the convergence time. The SNR is supposed to be close to 0 dB, therefore half of the measured signal variance is assigned to the noise and another half is assigned to the factor variance. All the parameters are thus initialized as follows, assuming $\kappa = 15$:

- $\boldsymbol{L}_0$ sampled in $\mathcal{N}_{\mathbb{C}}\left(0, \frac{\boldsymbol{I}_{M\kappa}}{\kappa}\right)$,
- $\boldsymbol{\sigma}_{n_0}^2 = 0.5\,\mathrm{diag}\left(\hat{\boldsymbol{S}}_{yy}\right)$,
- $\boldsymbol{\gamma}_0^2 = \frac{\mathrm{eig}_\kappa(\hat{\boldsymbol{S}}_{yy})}{2M}\,\mathrm{Trace}(\hat{\boldsymbol{S}}_{yy})$,
- $\boldsymbol{q}_0 = \boldsymbol{1}$,

where the $\mathrm{eig}_\kappa(\boldsymbol{A})$ refers to the κ highest eigenvalues of $\boldsymbol{A}$, normalized in order to have $\sum_\kappa \mathrm{eig}_\kappa(\boldsymbol{A}) = 1$. The matrix $\boldsymbol{S}_{cc}$ does not require to be initialized since it is drawn first.

2.4.4.2 Effect of the heteroscedasticity of the factors

In the model described before, a heteroscedastic prior is assumed for the factors (which means that $[\boldsymbol{c}] = \mathcal{N}_{\mathbb{C}}(\boldsymbol{0}, \lceil\boldsymbol{\gamma}^2\rfloor)$, where $\boldsymbol{\gamma}^2$ is a vector of different values). In order to show the motivation for this choice, a comparison is here performed with an homoscedastic prior for the factors (which means that $[\boldsymbol{c}] = \mathcal{N}_{\mathbb{C}}(\boldsymbol{0}, \gamma^2\boldsymbol{I}_\kappa)$, where γ^2 is a scalar). In this case, a single variance parameter for the factors is sampled. The evolution of the factor for the two samplers is given in Fig. 2.6, for which the weights $\boldsymbol{q}$ are all fixed to 1 throughout the iterations, and the scale parameters are sampled.

In the case where the factors are homoscedastic, even if the factor could be driven by the likelihood far from their assigned prior variance, they all remain close to the same value. On the contrary, when a different variance is sampled for each parameter, they are all more prompt to evolve independently. Therefore, 5 representative factors increase and the other factors slowly decrease, tending towards a sparse representation of the data.

This illustrates the mechanism behind the sparsity induced by a heteroscedastic model for the factors. With a more appropriate initialization (for example lowering

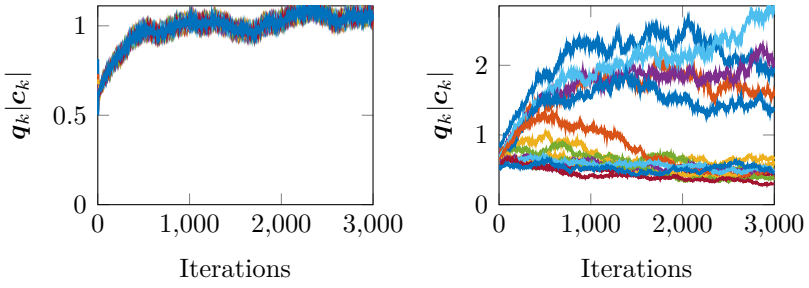

(a) $q = 1$, homoscedastic factors **(b)** $q = 1$, heteroscedastic factors

Figure 2.6: Evolution of the factors, without sampling of the weights (all $q_k = 1$), in the case of a homoscedastic (left) and heteroscedastic factors (right).

the initial factors), the convergence is improved and the solution can tend faster to the optimally sparsest solution.

2.4.4.3 Effect of the marginalization

The effect of the partial marginalization of the Gibbs sampler is now illustrated. The results presented in this section are obtained without the sampling of scale parameters. In Fig. 2.7 are plotted the absolute value of the weighted factors throughout the iterations, as well as the number of non-null weights, without and with marginalization.

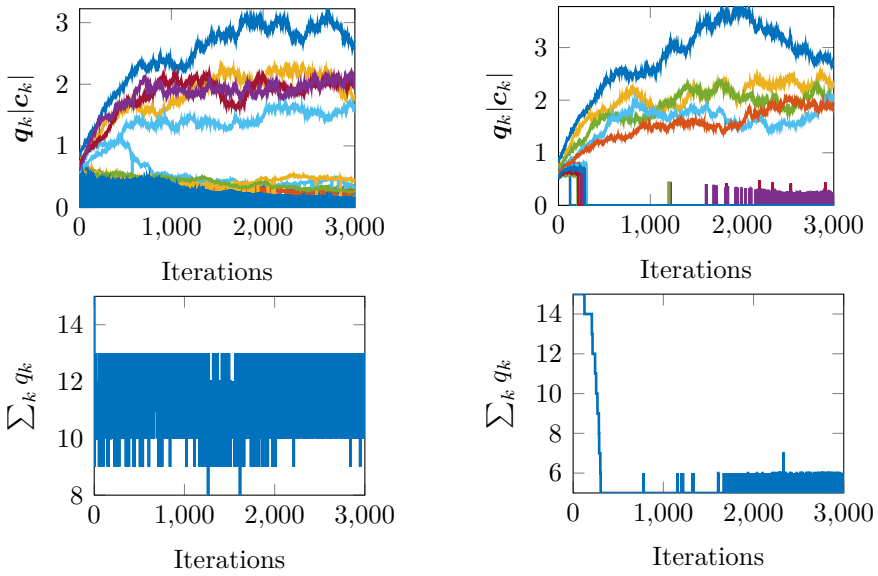

(a) No marginalization **(b)** With marginalization

Figure 2.7: Evolution of the factors and their weights, from the non-marginalized (left) and marginalized (right) Gibbs sampler, without the scaling strategy.

First, looking at the figure without marginalization (Fig. 2.7a), in comparison with the case where the weights $\boldsymbol{q}$ are not sampled (Fig. 2.6b), it appears that the sampling of the weights slightly enforces the sparsity by canceling a few small factors.

Then, looking at the case with the marginalization of the sampler, almost all the small factors are rapidly shrunk to zero, keeping only 5 dominant factors. Theoretically, the marginalization does not affect the target posterior distribution. Therefore, the solution with and without marginalization should tend to be similar after a larger amount of iterations. However, as expected, the marginalization increases significantly the convergence rate of the sampler.

2.5 Comparison of the denoising performance with methods from the literature

In this section, the performance of each investigated approach to denoise the synthesized data is compared, based on the different configurations of the numerical experiment described in Sec. 1.5.4.1. The default parameter values for the numerical simulations are recalled in Tab. 2.1.

Parameter	Default value
Frequency (invariant)	$f = 15$ kHz
Sound velocity (inv.)	340 m/s
Number of receivers (inv.)	$M = 93$
Number of monopoles	$K = 20$
SNR	SNR=10 dB
Number of snapshots	$N_s = 10^4$

Table 2.1: Default values for the numerical simulations.

It is also recalled that in this numerical case, the cross-terms are preserved during the simulation of the noisy CSMs, which causes the noise to deviate from the assumption of a total decorrelation over the sensors, especially for low SNR or/and low number of snapshots (in contrast to the numerical validation performed previously in the chapter for which no cross-term was simulated).

The relative reconstruction error given in Eq. (1.5.7) is studied for several denoising methods, first considering only the diagonal elements of the acoustical CSM and then looking at the reconstruction of the off-diagonal elements. The denoising methods of interest are:

- Convex optimization for diagonal reconstruction, referred to as Diagonal Reconstruction (DRec) (method described in Sec. 1.5.1),
- Robust Principal Component Analysis (RPCA) with a constant regularization parameter close to $1/\sqrt{M} \approx 0.1$, as suggested in Wright et al. (2009) (method described in Sec. 1.6),
- RPCA with the regularization parameter that gives the minimal error, written λ_{optimal}. Note that this optimal value will never be known in practice, since its calculation requires the knowledge of the ground-truth CSM $\boldsymbol{S}_{aa}$,
- Canonical Coherence Analysis (CCA) with both thresholding of the canonical coherences and adaptive iteration count (method described in Sec. 1.7),
- FA solved with the EM algorithm, referred to as FA-EM, initialized as in Sec. 2.3.2.1,
- FA solved with the marginalized Gibbs sampler, referred to as FA-MCMC, with the same initialization and priors as in Sec. 2.4.4.1,
- no denoising applied.

A list of the studied methods is given in Tab. 2.2 with a rough approximation of the computing time required by each method to denoise one 93×93 CSM, using non-optimized Matlab codes on a laptop. For the Gibbs sampler, a thousand of iterations are performed and the returned estimate of denoised matrix results from the mean over the last 500 samples. Considering that these last samples tend to have a stationary, symmetric, and unimodal distribution, the maximum a posteriori is assumed to be well estimated by the mean value.

Denoising method	**Acronym**	**Computing time**
Convex optimization	DRec	1 sec
Linear optimization		60 sec
Alternating projections		3 sec
Robust Principal Component Analysis	RPCA	0.5 sec
Canonical Coherence Analysis	CCA	< 0.1 sec
Factor analysis, solved with EM	FA-EM	1 sec
Factor analysis, solved with MCMC	FA-MCMC	300 sec for $\kappa = 92$ 10 sec for $\kappa = 10$

Table 2.2: List of the denoising methods and their approximate computing time to denoise one 93×93 CSM, using non-optimized Matlab codes on a laptop.

2.5.1 Reconstruction of the autospectra

As all the studied denoising methods are based on the assumption of an uncorrelated noise, we first look at their ability to reconstruct the diagonal elements of the acoustic CSM. In Fig. 2.8 is plotted the reconstruction error of the acoustic CSM as a function of the number of sources, SNR and number of averages N_s.

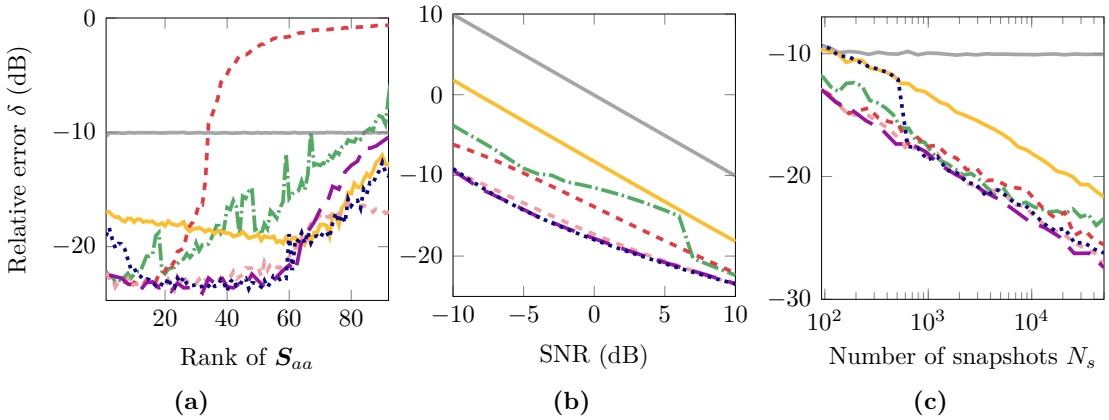

Figure 2.8: Relative reconstruction error of the diagonal terms of the signal CSM, as a function of the number of sources (a), SNR (b) and the number of snapshots (c). The denoising methods are : DRec (——), RPCA with $\lambda = 0.1$ (- - -), RPCA with λ_{optimal} (- - -), CCA (—·—), FA-MCMC (— —), FA-EM (·····), no denoising (——). The default parameter values for the simulations are given in Tab. 2.1.

The results from the FA denoising achieved with EM and MCMC are very similar because both methods rely on the formulation of a very similar inverse problem. However, when the number of sources is high, EM performs better than MCMC, because the latter makes a stronger assumption on low-rankness of the signal CSM. Moreover, for very low number of sources, or low number of snapshots, EM does not converge toward an optimal solution, whereas MCMC, being a global optimization algorithm, converges better.

Concerning RPCA, one can see that the selection of a regularization parameter can have a strong impact on the denoising performance, especially when the number of sources increases. The parameter $\lambda = 0.1$ proposed by Wright is tuned for low rank signal matrix. When the number of sources increases, the regularization parameter must also increase to keep the balance between the low-rankness of the signal CSM and sparsity of the noise CSM.

When proper assumptions are fulfilled (low rank signal CSM and high number of snapshots), the FA solution is similar to one given by RPCA when using the optimal regularization parameter, whereas the DRec error is most of the time 5 dB higher.

The reconstruction error given by CCA is very similar to those presented in Hald (2019) since the simulated case is nearly the same. The number of iterations automatically selected from the number of significant canonical coherences is also comparable to Hald (2019). This varying number of iterations induces significant discontinuities on the CCA error plotted versus the number of sources, which can be corrected by an appropriate tuning of the empirical thresholding values and iteration count criterion. Note that the CCA method generally suffers from a bias error – due to the fact that the square root matrices $\boldsymbol{S}_{xx}^{-1/2}$ and $\boldsymbol{S}_{yy}^{-1/2}$ used in Alg. 2 carry over the presence of noise – which probably explains why it has an error a few dB higher than FA and RPCA.

2.5.2 Reconstruction of the cross-spectra

All the studied methods make the assumption that the noise CSM is diagonal or nearly diagonal. Consequently, the extra-diagonal elements are expected to be almost unchanged by the denoising process.

To verify this fact, we can compare the relative error of the off-diagonal elements, defined as follows:

$$\delta_{\text{off}} = \frac{\left\| \hat{\boldsymbol{S}}_{aa} - \tilde{\boldsymbol{S}}_{aa} - \left\lceil \text{diag}\left(\hat{\boldsymbol{S}}_{aa} - \tilde{\boldsymbol{S}}_{aa}\right) \right\rfloor \right\|_F}{\left\| \hat{\boldsymbol{S}}_{aa} - \left\lceil \text{diag}\left(\hat{\boldsymbol{S}}_{aa}\right) \right\rfloor \right\|_F}, \tag{2.5.1}$$

where $\|\cdot\|_F$ is the Frobenius norm, $\hat{\boldsymbol{S}}_{aa}$ is the simulated acoustic CSM and $\tilde{\boldsymbol{S}}_{aa}$ is the denoised CSM.

The relative error curves of the cross-spectra are plotted in Fig. 2.9, for the denoising performed with FA, RPCA and CCA, always from the same numerical experiments.

On this figure, one can see that FA and RPCA denoising do not significantly change the off-diagonal terms, except that FA provides a slight denoising for very low SNR. Neither RPCA nor FA gives a worse error than without any denoising. This is not the case for CCA which modifies the cross-spectra, except when the number of sources is lower than 10 and when the number of snapshots is lower than 6000.

2.6 Conclusion

In this chapter, two ways to solve the FA problem have been proposed. The first one, the EM solver, is fast and provides satisfying results if the initialization is appropriate. Its main drawback, however, is to converge toward local maxima, which can be a problem for experimental applications for which the model errors and the

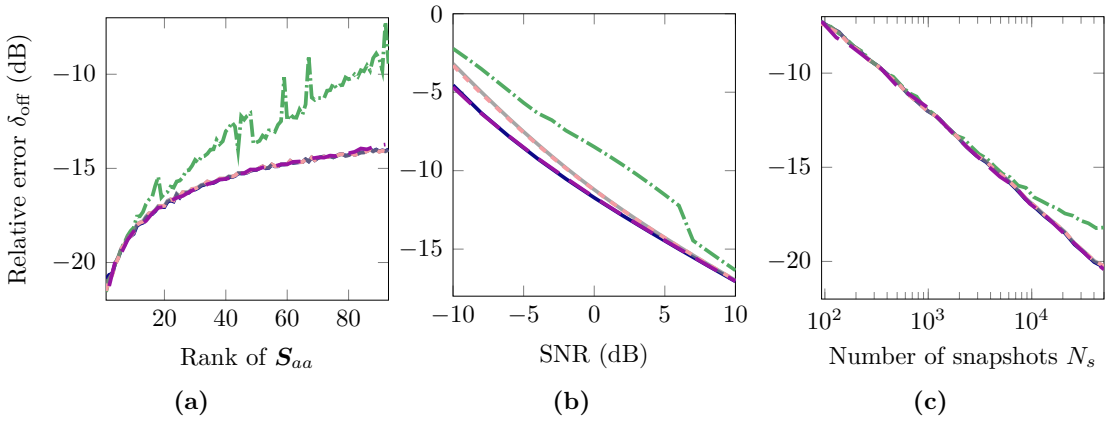

Figure 2.9: Relative reconstruction error of the signal CSM cross-spectra obtained from 3 denoising methods: RPCA with λ_{optimal} (- - -), FA-MCMC (— —), FA-EM (·····), CCA (—·—) and without denoising (——), as a function of the number of sources (a), SNR (b) and number of snapshots (c). The default parameter values for the simulations are given in Tab. 2.1.

noise can be high. Therefore, a more robust approach is also explored using a MCMC method. The Bayesian estimators obtained from the Gibbs sampler come with their whole posterior distribution, unlike the EM algorithm that returns point estimates. These distributions can then be exploited in order to provide credible intervals.

Several strategies have been employed to design and regularize a model which rapidly converges towards a sparse solution: heteroscedasticity of the factors (equivalent to a Gaussian mixture), Bernoullian factor weights, block sampling and partial marginalization of the sampler. This latter induces an extra cost which can be compensated by a reduction of the number of required iterations until convergence.

It should be noted that, as observed by Faure (2017), the model with Bernoullian weights is a little difficult to initialize, as compared to the model without weights, especially in the case where the data cannot be described by a sparse model. Therefore, this sparse model is not recommended for uncertain initializations. A strategy could be to first perform an inference using the model without weights (a simple Gaussian mixture) and then use the result to initialize the sparse model with Bernoullian weights. Some other MCMC samplers could also be implemented that may be more robust with respect to the initialization, such as Metropolis–Hastings (MH) samplers with adaptive proposal (see for example path-adaptive MH in van Dyk and Park (2011), Hamiltonian Monte Carlo in Neal (2011), Metropolis-Adjusted Langevin in Roberts and Rosenthal (1998)).

Finally, it has been shown that the Bayesian-based FA allows for a high level of denoising, as compared to the other methods from the literature, and that

MCMC offers a flexible framework, which opens up the possibility of including the correlation of the noise into the statistical model.

3

Identification of a correlated TBL noise model

Contents

The separation approach described in this chapter is an extension of the Factor Analysis (FA) model that has been introduced in the previous chapter. The objective of this extension is to deal with the situation where the Turbulent Boundary Layer (TBL) noise is correlated over the antenna, so that the assumption of uncorrelated noise done in the FA model no longer fits the data satisfactorily. This happens at low frequencies or high Mach number, when the size of the turbulent structures within the TBL becomes high enough to induce correlation lengths larger than the microphone interspacings. Therefore, the proposed extension of the FA denoising accounts for a correlated noise model for the identification of the TBL noise contribution, and is further called Factor Analysis with Correlated noise model (FA-Corr).

The chapter is organized as follows. The choice of the TBL model is first discussed and the model extension is mathematically developed. Then, some strategies for the estimation of the physical parameters for the TBL which are needed in the model,

such as the convection speed or the coherence decay rates, are discussed. And finally, the limits of the proposed separation method are discussed on a numerical toy case.

3.1 Wall-pressure models

Let us consider a flat, motion-less and rigid wall, immersed in an incompressible flow parallel to it. When it is far enough away from the wall, the fluid does not interact with the wall and its velocity is then denoted U_∞. In the vicinity of the wall, the interaction is no longer negligible and the velocity gradually decreases until it becomes zero at the wall. In this region of interaction, called the boundary layer, the fluid behavior depends on several physical parameters such as the viscosity, the density and the Reynolds number. The acoustic radiation from the TBL is supposed to be negligible since its associated energy is known to be proportional to the fifth power of Mach number (Hwang et al., 2003).

In the case of turbulent flow, the eddies in the boundary layer are convected with a velocity U_c which can be determined empirically, and generally falls within the following range:

$$0.6\ U_\infty < U_c < 0.8\ U_\infty.$$

Considering that the pressure field below a TBL is stationary and homogeneous in space, it can be described statistically by the cross-correlation of the pressure field. There exist several empirical models in the literature describing this spatial cross-correlation.

However, they are often written in the wavenumber domain, for several reasons. On the one hand, even if the space and wavenumber spectra theoretically carry the same information, it has been difficult for a long time to make measurements which are sufficiently accurate for analytic studies of the spatial correlation (Bull, 1996). And on the other hand, the wavenumber analysis is very well suited for the study of the vibroacoustic response of elastic plates to the TBL loading, which is a great advantage for many applications. The reader can refer to Bull (1996) and Graham (1997) for a comparison of the wavenumber-frequency spectrum models. These models describe the correlation length differently but are generally based on an exponential decay of the cross-spectra in space.

These exponential models mainly derive from the observations first made by Corcos (1963), who proposed a model based on the assumption of an uncorrelated decrease of the correlation along the longitudinal and transverse axes of the flow.

The statistical model proposed by Corcos for the covariance of the TBL noise for a pair of microphones (k, l) with coordinates $(\boldsymbol{x}_l, \boldsymbol{y}_l)$ and $(\boldsymbol{x}_k, \boldsymbol{y}_k)$, at a frequency f is

$$\boldsymbol{S}_{nn_{kl}}(f) = \Gamma(f)\mathrm{e}^{-\frac{2\pi f}{U_c}(\alpha_x|\boldsymbol{x}_k-\boldsymbol{x}_l|+\alpha_y|\boldsymbol{y}_k-\boldsymbol{y}_l|-\imath(\boldsymbol{x}_k-\boldsymbol{x}_l))}, \tag{3.1.1}$$

for the case where the flow is along the x direction, with $\Gamma(f)$ a scalar that depends on the frequency f, and where α_x and α_y are the longitudinal and transverse decay rates of the coherence, classically ranging from 0.1 to 0.12 and from 0.7 to 1.2, respectively (Hwang et al., 2003). In this model, the longitudinal and transverse correlation lengths are calculated as:

$$L_{c_{x,y}} = \frac{U_c}{2\pi f \alpha_{x,y}}. \tag{3.1.2}$$

Several criticisms have been made about this model. First, the decoupling of the coherence decays along the x and y axes has been refuted. Indeed, several models combining the two axes have been proposed, leading to an elliptical distribution of the wavenumbers (Mellen, 1990; Smol'Yakov et al., 1991; Singer, 1996). Moreover, this model assumes that the parameters U_c, α_x and α_y are constant with the frequency, which does not agree with measurements (Farabee and Casarella, 1991; Schloemer, 1966; Arguillat et al., 2010). Finally, the model has been shown to overestimate the low wavenumbers, which has led to numerous derived models.

However, this model also has many advantages, and seems suitable to be used in the FA-Corr denoising model, for the following reasons:

- it is written in the space domain, which is necessary since the model for the acoustic part is also written in space,
- it has a low number of parameters which have to be inferred or experimentally estimated,
- as the denoising at each frequency line is considered as a separate problem, it is possible to vary the parameter with the frequency to provide a more precise model.

As a first approach, the denoising model can therefore be based on the exponential decrease proposed by Corcos. However, the reader can easily adapt the reasoning and calculations developed in this chapter to any other model written in the space domain, especially Mellen's, which is very close in appearance to the Corcos' one:

$$\boldsymbol{S}^{\text{Mellen}}_{nn_{kl}}(f) = \Gamma(f)\mathrm{e}^{-\frac{2\pi f}{U_c}\left(\sqrt{(\alpha_x|\boldsymbol{x}_k-\boldsymbol{x}_l|)^2+(\alpha_y|\boldsymbol{y}_k-\boldsymbol{y}_l|)^2}-\imath(\boldsymbol{x}_k-\boldsymbol{x}_l)\right)}. \tag{3.1.3}$$

3.2 Extension of the PFA model

3.2.1 Problem statement

In order to state the separation problem, let us first introduce the vector of measurements $\boldsymbol{y}_j$ that concatenates the Fourier coefficients for each sensor at one frequency and one snapshot j. As said previously, these measurements result from the sum of a contribution coming from the acoustic sources written $\boldsymbol{a}_j$ and another major contribution induced by the TBL noise, written $\boldsymbol{n}_j$. A minor contribution is also added, which models the other sources of microphone self-noise $\boldsymbol{\epsilon}_j$, as well as the modeling errors. The sum of all the contributions reads:

$$\boldsymbol{y}_j = \boldsymbol{a}_j + \boldsymbol{n}_j + \boldsymbol{\epsilon}_j \quad j = 1, \cdots, N_s. \tag{3.2.1}$$

This measured field is supposed to be statistically stationary in time, and thus an estimate of the Cross-Spectral Matrix (CSM) is obtained by averaging over N_s snapshots at a given frequency. Assuming that the three terms in the sum (3.2.1) are statistically uncorrelated, such as the cross terms are negligible, the measurement CSM can be decomposed as follows:

$$\boldsymbol{S}_{yy} = \boldsymbol{S}_{aa} + \boldsymbol{S}_{nn} + \boldsymbol{S}_{\epsilon\epsilon}. \tag{3.2.2}$$

The separation method proposed in this chapter performs jointly the identification of each CSM of this sum, with a Bayesian approach. In order to make this inverse problem identifiable, the same constraints in terms of correlation structure and priors as in the classical FA model are first added to the acoustic and uncorrelated self-noise terms.

The acoustic field is still supposed to be highly correlated over the microphones, and to be possibly described by a few unobserved latent variables, which gives

$$\boldsymbol{a}_j = \boldsymbol{L}[\boldsymbol{q}]\boldsymbol{c}_j, \tag{3.2.3}$$

with $\boldsymbol{c}_j$ the complex vector of $\kappa \leq M$ latent variables, $\boldsymbol{q}$ a vector of κ binary weights and $\boldsymbol{L} \in \mathbb{C}^{M \times K}$ an unknown mixing matrix. The same priors and hyperpriors are also assigned:

$$[\boldsymbol{L}] = \mathcal{N}_{\mathbb{C}}(\boldsymbol{0}, \boldsymbol{I}_{M\kappa}/\kappa), \tag{3.2.4}$$

$$[\boldsymbol{c}] = \mathcal{N}_{\mathbb{C}}(\boldsymbol{0}, \lceil\boldsymbol{\gamma}^2\rfloor) \qquad \text{with } [\boldsymbol{\gamma}^2] = \mathcal{IG}(\boldsymbol{a}_\gamma, \boldsymbol{b}_\gamma), \tag{3.2.5}$$

$$[\boldsymbol{q}] = \mathcal{B}ern(l) \qquad \text{with } [l] = \mathcal{B}eta(a_l, b_l). \tag{3.2.6}$$

The additive random self-noise is supposed to be totally uncorrelated over the microphones and heteroscedastic. This can be statistically modeled by a diagonal CSM:

$$\boldsymbol{S}_{\epsilon\epsilon} = \lceil \boldsymbol{\sigma}_\epsilon^2 \rfloor. \tag{3.2.7}$$

This noise is supposed to be Gaussian, according to the Central Limit Theorem applied to Fourier coefficients:

$$[\boldsymbol{\epsilon}] = \mathcal{N}_{\mathbb{C}}(\mathbf{0}, \lceil \boldsymbol{\sigma}_\epsilon^2 \rfloor) \tag{3.2.8}$$

and an inverse-gamma distribution is chosen for the variance prior:

$$[\boldsymbol{\sigma}_\epsilon^2] = \mathcal{IG}(\boldsymbol{a}_\epsilon, \boldsymbol{b}_\epsilon). \tag{3.2.9}$$

Finally, another constrain is added to the model concerning the CSM of the TBL contribution. Among the existing models, the Corcos' one is chosen. Therefore, the theoretical covariance model for the TBL noise, at each frequency is

$$\boldsymbol{S}_{nn_{kl}} = |p|^2 \mathrm{e}^{-\frac{2\pi f}{U_c}(\alpha_x|\boldsymbol{x}_k - \boldsymbol{x}_l| + \alpha_y|\boldsymbol{y}_k - \boldsymbol{y}_l| - \imath(\boldsymbol{x}_k - \boldsymbol{x}_l))}, \tag{3.2.10}$$

$$= |p|^2 \boldsymbol{\Sigma}^2_{\nu_{kl}}(\boldsymbol{\theta}), \tag{3.2.11}$$

with $k, l = 1, \ldots, M$ and where $\boldsymbol{\theta} = \{U_c, \alpha_x, \alpha_y\}$ is the set of Corcos' parameters. In this model, the flow is supposed to be oriented along the x direction. The amplitude term $|p|^2$ is a real positive scalar. A first attempt to model the amplitude term with a complex vector has been undertaken. The objective was to enable the amplitude to vary over the microphone, which gave an amplitude term in the form $\boldsymbol{p}_k \boldsymbol{p}_l^*$, with $\boldsymbol{p}$ complex. However, this model makes the parameter set $\boldsymbol{\theta}$ not uniquely identifiable, which would make its physical interpretation impossible.

As the latent variable factorization which describes the acoustic part can theoretically capture any correlation structure, the correlated TBL noise can be inferred within this decomposition, leading to an underestimation of the TBL part (and an overestimation of the acoustic one). This is why this inference problem has to be appropriately regularized, which is done by choosing informative priors for the TBL parameters. A Gaussian prior, which is easy to parameterize to take prior information into account is adopted for the sampling of the complex amplitude term p:

$$[p] = \mathcal{N}_{\mathbb{C}}(a_p, \sigma_p^2). \tag{3.2.12}$$

Equivalently, $|p|^2$ could have been sampled in a Chi-square distribution.

Then, a random vector $\boldsymbol{\nu}$ representing the normalized TBL field can be sampled with a Gaussian prior distribution,

$$[\boldsymbol{\nu}] = \mathcal{N}_{\mathbb{C}}(\mathbf{0}, \boldsymbol{\Sigma}_{\nu}^2(\boldsymbol{\theta})), \tag{3.2.13}$$

in order to build the estimated CSM for the TBL contribution,

$$\hat{\boldsymbol{S}}_{nn} = |p|^2 \hat{\boldsymbol{S}}_{\nu\nu}. \tag{3.2.14}$$

As the additive noise $\boldsymbol{\epsilon}$ is not directly sought, its sampling is not required. On the contrary, the sampling of $\boldsymbol{S}_{\nu\nu}$ is required for the posterior expression of some other parameters and it is also desirable, as it would allow the TBL CSM to slightly deviate from the Corcos' variance model, driven by the likelihood of the data.

Finally, concerning the set of Corcos' parameters $\boldsymbol{\theta} = \{U_c, \alpha_x, \alpha_y\}$, two kinds of strategy can be adopted to estimate them. First, they can be estimated before performing the denoising, and then be used as it is in the model, without being sampled nor updated. This can be done by a regression over the measurement CSM, or from additional measurements with a dense microphone array designed for the characterization of the TBL for example. This kind of complementary measurements can be done in closed wind-tunnel, however, they are not always available, especially for inflight measurements. Otherwise, if these parameters cannot be precisely known prior to the denoising, they can be inferred along with all the other parameters of the model, during the denoising process. For this purpose, the proposed prior for these parameters are multivariate Gaussian:

$$[\boldsymbol{\theta}] = \mathcal{N}_{\mathbb{R}}(\boldsymbol{\mu}_{\theta}, \boldsymbol{\Sigma}_{\theta}^2). \tag{3.2.15}$$

More details about these strategies for the estimation of the TBL parameters are given bellow in Sec. 3.3.

To summarize the overall model, a hierarchical graph is given in Fig. 3.1.

3.2.2 Posterior distributions for sampling

For the development of the posterior expressions, the calculation steps are very similar to those from the previous chapter. The general form of most of the posteriors is the same, but some new cross-terms are added, *viz.* $\boldsymbol{S}_{y\nu}$ and $\boldsymbol{S}_{\nu c}$. Incidentally, the implementation of the Gibbs sampler has to properly handle the updating of these cross-terms.

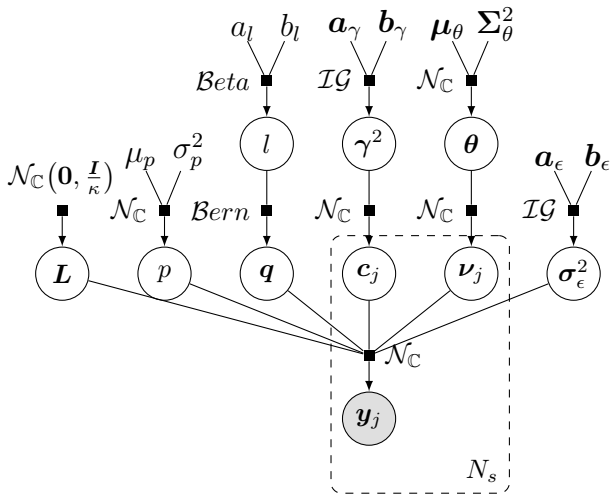

Figure 3.1: Hierchical graph for the FA-Corr model.

Using the fact that the likelihood is given by

$$[\boldsymbol{y}_j \mid \infty] = \mathcal{N}_\mathbb{C}\left(\boldsymbol{L}\lceil \boldsymbol{q} \rfloor \boldsymbol{c}_j + p\boldsymbol{\nu}_j, \lceil \boldsymbol{\sigma}_\epsilon^2 \rfloor\right), \tag{3.2.16}$$

the expressions of the posterior are given in appendix D.1, except for the case of the hyperparameter $\boldsymbol{\theta}$ whose inference is discussed below.

It would also be possible to write the direct problem in a matrix form as follows:

$$\boldsymbol{y}_j = \begin{bmatrix} \boldsymbol{L} & p\boldsymbol{I}_M \end{bmatrix} \begin{bmatrix} \lceil \boldsymbol{q} \rfloor & \boldsymbol{0} \\ \boldsymbol{0} & \boldsymbol{I}_M \end{bmatrix} \begin{bmatrix} \boldsymbol{c}_j \\ \boldsymbol{\nu}_j \end{bmatrix} + \boldsymbol{n}_j, \tag{3.2.17}$$

in order to facilitate the update of the cross-terms, and to allow block sampling in multivariate Gaussian. However, this strategy has not been adopted, so that different families of priors can be easily experimented.

3.3 Estimation of the TBL parameters

In order to identify the unknown CSM $\boldsymbol{S}_{nn}$, the variance given by the Corcos' model in Eq. (3.2.15) has to be known. Therefore, the Corcos' parameters $\boldsymbol{\theta} = \{\alpha_x, \alpha_y, U_c\}$ have to be determined from the measurements. To do so, two procedures are proposed: a least squares regression procedure to be performed before the denoising and a Bayesian inference approach to be added within the FA-Corr algorithm.

3.3.1 Least squares regression

The first approach to estimate the Corcos' parameters is inspired from Arguillat et al. (2010). A Non-Linear Least Squares (NLLS) fitting is performed on the

measurement CSM before the separation procedure, which solves the following optimization problem at each frequency:

$$(U_c, \alpha_x, \alpha_y)^\star = \operatorname{argmin} \left\| \frac{\hat{\boldsymbol{S}}_{yy}}{\frac{1}{M}\operatorname{tr}\left(\hat{\boldsymbol{S}}_{yy}\right)} - \boldsymbol{G}(U_c, \alpha_x, \alpha_y) \right\|_F^2 \tag{3.3.1}$$

with

$$\boldsymbol{G}_{kl}(U_c, \alpha_x, \alpha_y) = \mathrm{e}^{-\frac{2\pi f}{U_c}(\alpha_x|\boldsymbol{x}_k - \boldsymbol{x}_l| + \alpha_y|\boldsymbol{y}_k - \boldsymbol{y}_l| - \imath(\boldsymbol{x}_k - \boldsymbol{x}_l))}. \tag{3.3.2}$$

This method is fast and simple to implement since many ready-to-use functions exist to solve NLLS problems. In addition, at the end of the NLLS optimization, the covariance matrix can be estimated from the variance $\boldsymbol{\Sigma}^2$ and the Jacobian matrix $\boldsymbol{J}$ of the residuals:

$$\boldsymbol{\Sigma}_\theta^2 \approx \boldsymbol{\Sigma}^2 \left(\boldsymbol{J}^H \boldsymbol{J}\right)^\dagger, \tag{3.3.3}$$

where $\cdot^\dagger$ indicates the pseudo-inverse operator. The Jacobian matrix of the residuals is often required for the gradient descent algorithms, and is thus available at the end of the regression. In the present work, the Levenberg–Marquardt algorithm implemented in the Matlab function `lsqnonlin` has been used.

The NLLS approach could be used to directly perform the separation, but this method comes with some limitations. Indeed, the acoustic part is not taken into account for the data fitting. The acoustic CSM could be estimated from the residuals of the fitting process, but it may lead to a negative CSM.

3.3.2 Bayesian inference

Another way to estimate the Corcos' parameters, is to infer them within the Gibbs sampler, along with all the other unknown parameters of the model.

In this case, they have to be assigned a prior distribution. As said before, a possible prior that easily integrates prior information is the multivariate Gaussian:

$$[\boldsymbol{\theta}] = \mathcal{N}_{\mathbb{R}}(\boldsymbol{\mu}_\theta, \boldsymbol{\Sigma}_\theta^2). \tag{3.3.4}$$

The prior mean value $\boldsymbol{\mu}_\theta$ can be known, either from physical considerations, or from the NLLS regression introduced before. Another less precise but simpler approach is to look at the phase and coherence between the sensors. Indeed, the convection speed can be estimated from a linear regression on the unwrapped phase

ϕ of the cross-spectra, since in the Corcos' model,

$$\phi = -\frac{\omega(\boldsymbol{x}_k - \boldsymbol{x}_l)}{U_c} \tag{3.3.5}$$

and on the coherence γ_{kl} between sensors aligned on the flow axis or on its normal axis should give an approximation of the parameters α_x and α_y since

$$\ln(\gamma_{kl}) = \ln\left(\sqrt{\frac{|\boldsymbol{S}_{kl}|^2}{\boldsymbol{S}_{kk}\boldsymbol{S}_{ll}}}\right) = -\frac{\omega}{U_c}\alpha_x|\boldsymbol{x}_k - \boldsymbol{x}_l| \tag{3.3.6}$$

for a pair of sensors aligned along the x direction, and

$$\ln(\gamma_{kl}) = -\frac{\omega}{U_c}\alpha_y|\boldsymbol{y}_k - \boldsymbol{y}_l| \tag{3.3.7}$$

for a pair of sensors aligned along the y direction. Once an approximate range of possible values is known, the prior variance for $\boldsymbol{\theta}$ can be tuned manually, and the posterior distribution can be computed:

$$[\boldsymbol{\theta} \mid \infty] \propto [\boldsymbol{\theta}] \prod_{j=1}^{N_s} [\boldsymbol{\nu}_j \mid \infty], \tag{3.3.8}$$

$$\propto \frac{\mathrm{e}^{-\sum_j \boldsymbol{\nu}_j^H \boldsymbol{\Sigma}_\nu^{-2}(\boldsymbol{\theta})\boldsymbol{\nu}_j}}{\prod_j |\boldsymbol{\Sigma}_\nu^2(\boldsymbol{\theta})|} \frac{\mathrm{e}^{-\frac{1}{2}(\boldsymbol{\theta}-\boldsymbol{\mu}_\theta)^H \boldsymbol{\Sigma}_\theta^{-2}(\boldsymbol{\theta}-\boldsymbol{\mu}_\theta)}}{|\boldsymbol{\Sigma}_\theta^2|}. \tag{3.3.9}$$

No closed-form of this expression can be developed for the sampling, therefore, a Metropolis–Hastings (MH) step is implemented within the Gibbs sampler.

3.3.2.1 Metropolis-Hastings within Gibbs implementation

The principle of the MH algorithm is to iteratively pick a parameters set in a candidate distribution based on the current set, and then accept or reject it as the new set with some probability. In the case of a symmetric proposal distribution, the probability of acceptance is given by the ratio of the posterior distribution computed with the current parameter set and with the proposed ones. The acceptation-rejection procedure is thus performed in three steps. First, a parameter set is sampled in a Gaussian proposal distribution

$$\boldsymbol{\theta}_i = \mathcal{N}_{\mathbb{R}}(\boldsymbol{\theta}_{(i-1)}, \boldsymbol{\Sigma}^2_{\text{prop}}), \tag{3.3.10}$$

where $\boldsymbol{\theta}_{(i-1)}$ is the Corcos' parameter set at the current state and $\boldsymbol{\Sigma}^2_{\text{prop}}$ is the covariance of the proposal. Then, the acceptance rate r is computed by

$$r = \min\left(1, \frac{[\boldsymbol{\theta}_{(i-1)} \mid \infty]}{[\boldsymbol{\theta}_i \mid \infty]}\right), \tag{3.3.11}$$

where $\cdot_i$ indicates the i^{th} iteration. And finally the update is rejected if r is smaller than a sample u drawn in a uniform distribution $\mathcal{U}(0,1)$, and accepted otherwise.

In order to explore properly the target distribution, the proposal should have the same shape as the target. This implies that the covariance of the proposal has to be adjusted so that the proposed steps are large enough to ensure good convergence, but not too large to avoid having a too high rejection rate. This covariance can be tuned automatically with adaptive MH algorithm, or manually by checking the convergence rate. It has been shown that the optimal trade-off between the step size and the number of rejections is reached when the acceptance rate is 23.4% for a univariate Gaussian proposal and 44% for a Gaussian whose dimension tends to infinity (Brooks et al., 2011).

3.3.2.2 Pseudo-code

The overall pseudo-code for FA-Corr is given in Alg. 6. In this code, many options are implemented:

- the 'scaling' option is the sampling of a scale parameter as described in the previous chapter, in Sec. 2.4.2.2,
- the 'marginalization' option is the sampling of the factor weights $\boldsymbol{q}$ in a posterior marginalized with respect to the factors, as described in Sec. 2.4.3,
- the 'sampled' option for $\boldsymbol{\Sigma}_\nu^2$ is the sampling of the TBL parameters $\boldsymbol{\theta}$ and thus the update of $\boldsymbol{\Sigma}_\nu^2(\boldsymbol{\theta})$,
- the 'fixed' option for $\boldsymbol{\Sigma}_\nu^2$ is the absence of sampling of $\boldsymbol{\theta}$, which remains at its initial value.

Another option, not shown in the pseudo-code, consists in keeping the correlated noise matrix to zero ($p = 0$ and $\boldsymbol{S}_{\nu\nu} = \boldsymbol{0}$) across the iterations, which is equivalent to the FA problem with uncorrelated noise.

The main difference in terms of input parameters for FA-Corr versus FA is that the distances between the sensors $\boldsymbol{\delta x}, \boldsymbol{\delta y}$ have to be known, as well as the frequency f, which is also necessary for the TBL model.

3.4 Numerical validation

The approach is now tested on numerical experiments. The data are simulated by solving the direct problem described in Sec. 3.2.1. The various constants used for these simulations are similar to the validation case from the previous chapter: the number of microphones is $M = 30$, the number of uncorrelated sources is $K = 5$ and the number of snapshots is $N_s = 10^4$. Concerning the simulation of the TBL CSM, a

Algorithm 6 FA-Corr solved with the CSM-based Gibbs sampler.

Initialization: $\boldsymbol{L}_0,\ \boldsymbol{\sigma}^2_{\epsilon_0},\ \boldsymbol{\gamma}^2_0,\ \boldsymbol{q}_0,\ \boldsymbol{S}_{\nu\nu_0},\ \boldsymbol{\sigma}^2_{\nu_0},\ \boldsymbol{\theta}_0,\ p_0$

Require: $\hat{\boldsymbol{S}}_{yy},\ \kappa,\ \boldsymbol{a}_\gamma,\ \boldsymbol{b}_\gamma,\ \boldsymbol{a}_\epsilon,\ \boldsymbol{b}_\epsilon,\ a_l,\ b_l,\ \mu_p,\ \sigma^2_p,\ \boldsymbol{\mu}_\theta,\ \boldsymbol{\Sigma}^2_\theta,\ N_{\text{run}},\ \boldsymbol{\delta x},\ \boldsymbol{\delta y},\ f,\ \boldsymbol{\Sigma}^2_{\text{prop}}$

for $i = 1, \ldots, N_{\text{run}}$ **do**

Sample $\boldsymbol{S}_{cc_i}$ following Eq. (D.1.6)

Sample $\boldsymbol{L}_i$ in Eq. (D.1.14)

if 'Scaling' option activated **then**

Sample $\boldsymbol{s}_i$ in Eq. (C.2.3)

Scale $\boldsymbol{S}_{cc_i}$ and $\boldsymbol{L}_i$ doing $\boldsymbol{L}_k := \frac{\boldsymbol{L}_k}{\boldsymbol{s}_k}$ and $\boldsymbol{c}_k := \boldsymbol{c}_k \boldsymbol{s}_k$

Sample $\boldsymbol{\gamma}^2_i$ in Eq. (2.4.20)

Update $\boldsymbol{\Omega}_c$ using the new $\boldsymbol{L}$ and $\boldsymbol{S}_{cc}$

Resample $\boldsymbol{W}_c$ using the new $\boldsymbol{\Omega}_c$

else

Sample $\boldsymbol{\gamma}^2_i$ in Eq. (2.4.20)

end if

Update $\boldsymbol{S}_{yc}$ following Eq. (D.1.25)

Sample $\boldsymbol{S}_{\nu\nu_i}$ following Eq. (D.1.12)

Update $\boldsymbol{S}_{y\nu}$ following Eq. (D.1.27)

Sample p in Eq. (D.1.21)

if 'Fixed' option for $\boldsymbol{\Sigma}^2_\nu$ activated **then**

$\boldsymbol{\Sigma}^2_{\nu_i} = \boldsymbol{\Sigma}^2_{\nu_0}$

else 'Sampled' option for $\boldsymbol{\Sigma}^2_\nu$ activated

Sample $\boldsymbol{\theta}_i$ in Eq. (3.3.10)

Calculate the acceptance rate as Eq. (3.3.11)

if $r < (u \sim \mathcal{U}(0,1))$ **then**

$\boldsymbol{\theta}_i = \boldsymbol{\theta}_{i-1}$ *Rejection of the sample*

$\boldsymbol{\Sigma}^2_{\nu_i} = \boldsymbol{\Sigma}^2_{\nu_{i-1}}$

else

$\boldsymbol{\Sigma}^2_{\nu_i} = \boldsymbol{G}(\boldsymbol{\theta}_i)$ with $\boldsymbol{G}$ given by Eq. (3.3.2)

end if

end if

Sample l_i in Eq. (2.4.26)

if 'Marginalization' option activated **then**

Sample $\boldsymbol{q}_i$ in Eq. (D.1.46)

else

Sample $\boldsymbol{q}_i$ in Eq. (D.1.39)

end if

Sample $\boldsymbol{\sigma}^2_{\epsilon_i}$ in Eq. (D.1.32)

end for

return Posterior PDFs of $\boldsymbol{S}_{cc},\ \boldsymbol{S}_{\nu\nu},\ p,\ \boldsymbol{L},\ \boldsymbol{\sigma}^2_\epsilon,\ \boldsymbol{\gamma}^2,\ \boldsymbol{q}$

Corcos' model is chosen with the following parameters: $U_c = 10$ m/s, $\alpha_x = 0.12$ and $\alpha_y = 1$. The ratio between the acoustic signal and the TBL noise is -10 dB, whereas the ratio between the acoustic signal and the additive uncorrelated noise is 10 dB.

The microphones are randomly distributed on a squared area of 50×50 cm and the frequency of the study is 38 Hz. The TBL noise is highly correlated over the microphones at this frequency, since the correlation length along the flow axis is about 34 cm, which is twice the average microphone interspacing ($L_{c_x} = 2\overline{\boldsymbol{\delta x}}$).

For a better analysis of the chains, the scale option is activated. Even if the calculation details have been given for the implementation of a marginalized Gibbs sampler, it has been observed a strong instability of the marginalized sampler for the inference of the correlated noise. Therefore, it is recommended to not use the marginalization in unfavorable cases, such as low acoustic to TBL ratio, low number of snapshots or sensors or low frequency. As all these conditions are present in the numerical simulations, the factor weights are sampled without marginalization in the following.

3.4.1 Initialization and priors

Prior parameters

Flat priors are set for the acoustic part and the additive uncorrelated noise:

- a uniform prior for the sparsity is chosen by setting $a_l, b_l = 1$,
- for the factor variance, $\boldsymbol{a}_\gamma, \boldsymbol{b}_\gamma$ and for the uncorrelated variance $\boldsymbol{a}_\epsilon, \boldsymbol{b}_\epsilon = 10^{-4}$.

Informative priors are chosen for the TBL noise, with

- $a_p = \sqrt{\text{Trace}(\hat{\boldsymbol{S}}_{yy})/M}$ and $\sigma_p^2 = 10\,\text{Trace}(\hat{\boldsymbol{S}}_{yy})/M$,
- $\boldsymbol{a}_\theta = \{0.9U_c, 0.9\alpha_x, 0.9\alpha_y\}$, $\boldsymbol{\Sigma}_\theta^2 = \lceil 0.1U_c\ 0.5\alpha_x\ 0.5\alpha_y \rfloor$.

Initialization

The parameters are initialized as follows:

- $\kappa = 15$,
- $\boldsymbol{L}_0$ sampled in $\mathcal{N}_{\mathbb{C}}\left(0, \frac{\boldsymbol{I}_{M\kappa}}{\kappa}\right)$,
- $\boldsymbol{\sigma}_{\epsilon_0}^2 = 0.5\,\text{diag}\left(\hat{\boldsymbol{S}}_{yy}\right)$,
- $\boldsymbol{\gamma}_0^2 = \frac{\text{eig}_\kappa(\hat{\boldsymbol{S}}_{yy})}{2M}\,\text{Trace}(\hat{\boldsymbol{S}}_{yy})$,
- $\boldsymbol{q}_0 = \boldsymbol{1}$,
- $p_0 = a_p$,
- $\boldsymbol{\theta}_0 = \boldsymbol{a}_\theta$,
- $\boldsymbol{S}_{\nu\nu_0} = \boldsymbol{\Sigma}_\nu(\boldsymbol{\theta}_0)$,

where the $\text{eig}_\kappa(\boldsymbol{A})$ refers to the κ highest eigenvalues of $\boldsymbol{A}$, normalized in order to have $\sum_\kappa \text{eig}_\kappa(\boldsymbol{A}) = 1$. Even if the additive uncorrelated noise is expected to be low, it is preferable to set its initial value rather high, in order to start with a rather flat likelihood and ensure a good exploration before the chain stabilizes.

Proposal distribution for the Metropolis-Hastings step

As previously said, the proposal distribution is a Gaussian, with mean $\boldsymbol{\theta}$ from the previous iteration. However, as the algorithm is not adaptive, the variance of the proposal distribution has to be set by the user. It is chosen empirically in order to have an acceptance rate between 23 and 44 %. This corresponds to a variance of about $10^{-4}\boldsymbol{\Sigma}_\theta^2$. Note that this acceptance rate is difficult to tune precisely since it may decrease gradually as the chain stabilizes, the posterior becoming narrower.

3.4.2 Results

Some chains which are representative of the behavior of the sampler are shown, for three different options of the sampler:

- with the sampling of the Corcos' parameters, starting from arbitrary values $\boldsymbol{\theta}_0 = \{0.9U_c, 0.9\alpha_x, 0.9\alpha_y\}$, in Fig. 3.2,
- without the sampling of the Corcos' parameters, which are kept at the same arbitrary value (only the amplitude parameter p and the TBL CSM $\boldsymbol{S}_{\nu\nu}$ are sampled), in Fig. 3.3,
- with the correlated noise kept at zero, which is equivalent to the FA problem with uncorrelated noise only, in Fig. 3.4.

For each of these denoising configuration, the eigenvalues of the acoustic and TBL CSM are also given, in Fig. 3.5.

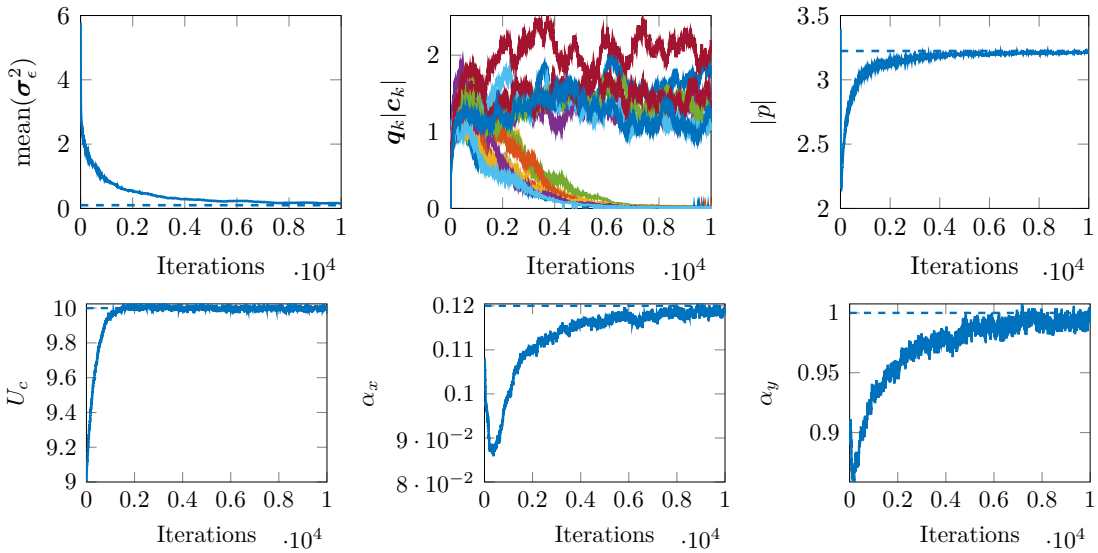

Figure 3.2: Chains of several inferred parameters, from FA-Corr with the Corcos' parameters sampled. The dashed lines indicate the target values.

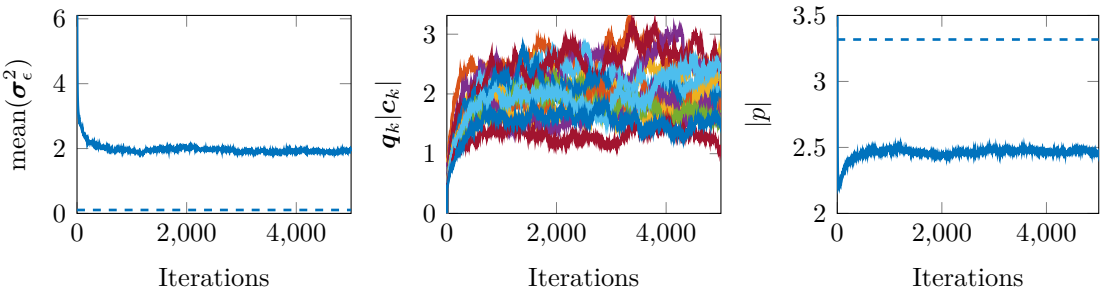

Figure 3.3: Chains of several inferred parameters, from FA-Corr with the Corcos' parameters kept constant at $\boldsymbol{\theta} = \{0.9U_c, 0.9\alpha_x, 0.9\alpha_y\}$. The dashed lines indicate the target values.

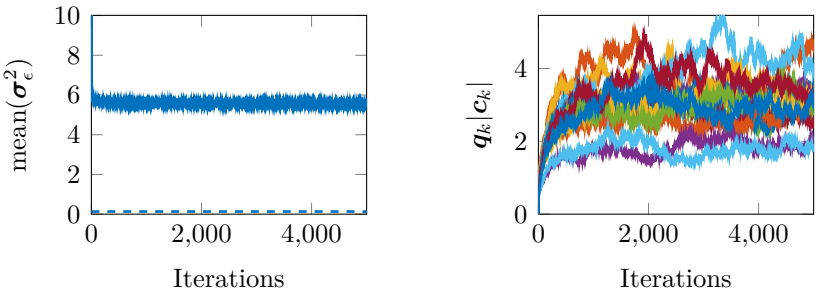

Figure 3.4: Chains of several inferred parameters, from the FA model, without inferring any correlated noise, with marginalization of the sampler. The dashed line indicates the target value for the additive noise.

The chains obtained from the solver with inference of the Corcos' parameters (Fig. 3.2) all converge toward the target values, with a correct selection of the rank for the acoustic part. However, the number of iterations before the chains stabilize is more than 8000, which is much higher than for the FA denoising with uncorrelated noise model since the number of inferred parameters is higher. The convergence of each parameters depends on many factors in the data set. For example, the parameter $\boldsymbol{\sigma}_\epsilon^2$ which drives the variance of the likelihood converges much faster when the number of sensors increases (this is illustrated in appendix, Fig. D.1). Another effect on the convergence may be the frequency. For example, if the frequency is 4 times higher, which corresponds to a much smaller correlation length of the TBL noise ($L_{c_x} = 0.5\overline{\boldsymbol{\delta x}}$), the TBL parameters converge at a slower pace, and with a higher variance, as illustarted in appendix, Fig. D.2. Many other elements can have an effect on the convergence, such as the microphone configuration, the level ratio between the different contributions, and so on.

Without the sampling of the TBL parameters, the TBL CSM is underestimated, and consequently the additive noise and acoustic part are overestimated, as well

as the number of factors. The reconstruction error on the acoustic CSM is -13 dB with the sampling of the TBL parameters, whereas without their sampling, this error is 3 dB. And for the case of inference without any correlated noise model, this reconstruction error is much larger (7 dB), which shows that taking into account a TBL model, even with an inaccurate prior is better than just considering a totally uncorrelated noise model.

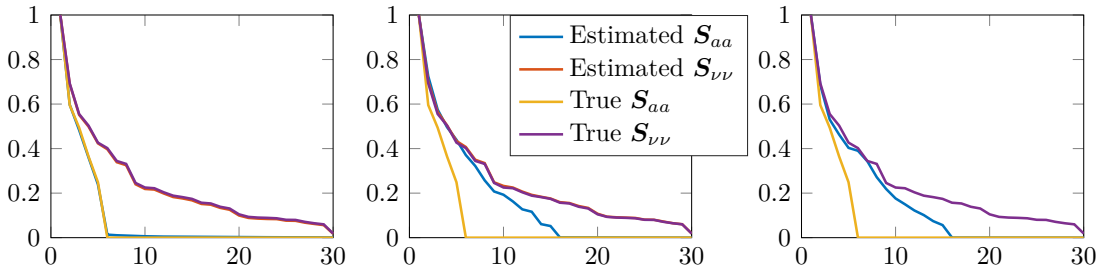

(a) From FA-Corr, $\boldsymbol{\theta}$ sampled. **(b)** From FA-Corr, $\boldsymbol{\theta}$ fixed. **(c)** From FA with uncorrelated noise only.

Figure 3.5: Normalized eigenvalues of the estimated and true CSM, for the acoustic and TBL contributions.

The chain analysis can be complemented by an examination of the eigenvalues of each simulated and inferred contribution. These eigenvalues are given in Fig. 3.5 for the three solver options. First, looking at the eigenvalues for the TBL part ($\boldsymbol{S}_{\nu\nu}$), it appears that the baseline and the inferred eigenvalues perfectly superimpose. However, it doesn't necessarily guarantee a good reconstruction of the TBL part, because several TBL parameter sets can provide the same eigenvalues. Indeed, this happens as long as the correlation structure of the CSM is preserved, which is the case when the ratio between the parameters is preserved. For example, in the present case, the eigenvalues of the initial CSM with the starting parameters $\{0.9U_c, 0.9\alpha_x, 0.9\alpha_y\}$ are similar to those from the simulated CSM with $\{U_c, \alpha_x, \alpha_y\}$. However, there is no problem of identifiability, since only one parameter (U_c) drives the phase of the CSM. This parameter is quickly updated and consequently, the other parameters are updated to finally infer the correct correlation structure with the correct parameter set.

Concerning the eigenvalue of the acoustic part, only the sampling of the TBL parameters guarantees a correct estimation of the rank. For the two other solvers, the rank is overestimated to compensate for the error made on the other contribution.

About the parametrization of the TBL model

The parametrization of the correlated noise variance was done on the basis of the physical model, but it is questionable whether it is appropriate. Indeed, if the parameters are prompt to be correlated, the chains may have a bad mixing and a slow convergence. To evaluate this, the last 2000 samples (considered as stationary) are plotted in Fig. 3.6, which corresponds to about 600 different samples for the Corcos' parameters since the acceptance rate is about 30%. The associated correlation coefficients are also given on the same figure. These bivariate scatter plots allow a visual diagnosis of the cross-correlation between the parameters. All

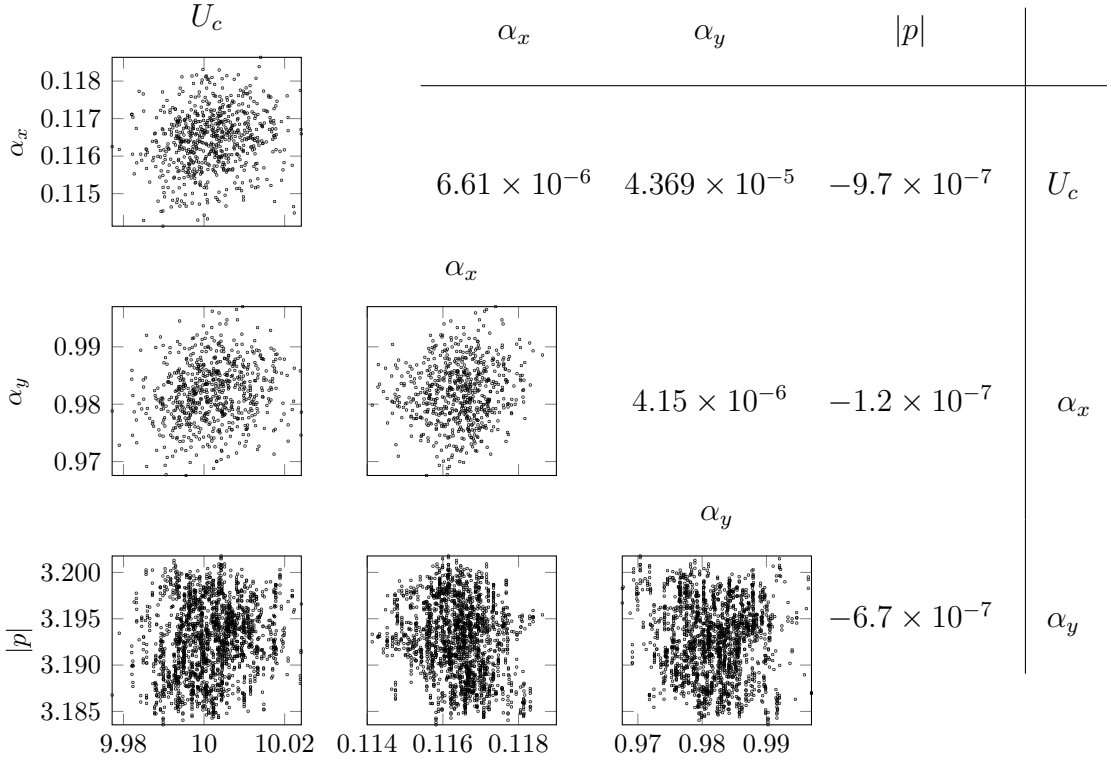

Figure 3.6: Plot of the last 2000 samples of the Corcos' and amplitude parameters. The correlation coefficients of each parameter pair is also given.

the plots seem wide enough to indicate that the correlation between the parameters is small, which is confirmed by the smallness of all the correlation coefficients. Therefore, this parameterization seems suitable to favor the sampler convergence.

3.5 Conclusion

In this chapter, an extension of the FA denoising problem has been proposed in order to account for the presence a of correlated TBL noise within the fitting model.

A Corcos' model has been chosen to model the TBL correlation structure, and the Bayesian approach accounts for the uncertainty about the physical parameters of this model. From the numerical toy case, it has been shown that the acoustic and TBL CSMs can be jointly identified. The $\boldsymbol{Lc}$ decomposition for the acoustic part could theoretically capture any correlation structure and thus the correlated TBL noise could be identified as an acoustic contribution. However, the problem is made identifiable thanks to the use of informative priors over the TBL parameters.

Compared to FA, this extension requires more knowledge about the data set, such as the microphone interspacing, and a rough idea of the flow characteristics. But still, no assumption about the acoustic sources is made.

However, a strong hypothesis is made about the TBL, which is considered as spatially homogeneous. If this assumption is reasonable for application in closed tunnel where the flow is controlled, it does not hold true for other applications such as inflight measurements. Moreover, for practical applications, the TBL model may differ from a Corcos' one and the ratio with the acoustic part can be much lower than -10 dB. Also, if the array is designed for the characterization of acoustic sources, the identification of the TBL part may be challenging and thus affect the quality of the separation of the contributions.

In order to evaluate the ability of the FA-Corr method to perform an efficient separation of the acoustic and TBL fields in such conditions, an assessment on experimental data is needed. This assessment is proposed in the next chapter, which is dedicated to the applications of the FA and FA-Corr denoising to closed tunnel and inflight measurements.

4

Experimental applications

Contents

Some applications of the Factor Analysis (FA) denoising and Factor Analysis with Correlated noise model (FA-Corr) separation approaches introduced before are given in this chapter. The objective is to see if their identifications of the acoustic and TBL contributions (the latter for FA-Corr only) are efficient under conventional conditions of imaging applications, with antennas designed for acoustic source localization.

The methods are first tested on measurements performed in a wind tunnel with a closed test section in the framework of the ADAPT project, for which the

acoustic sources power and location are known and the flow is controlled. In this situation, the validation is done by measuring the acoustic and TBL contributions separately. As the acoustic sources are loudspeakers inside the tunnel roof, their effect on the flow is negligible. Conversely, the flow has a slight impact on the propagation of the sources, and the subsequent perturbation can be quantified. Therefore, the measurement of the sources with flow is considered as the sum of the two independent contributions.

In a second step, another set of data is employed, provided by Airbus. These data are obtained from microphones flushmounted on the fuselage of a large aircraft and the measurements are made during a flight in cruise conditions. The general objectives of these measurements is the study of jet, airframe and engine noise and also of the understanding of the TBL excitation which is a major source of noise in the cabine (Maury et al., 2002). The measurement conditions are such that the aeroacoustic sources are unknown and the precise nature of the boundary layer is not known. Therefore, the validation of the separation results is more challenging. Some accelerometers located inside the cabin, which are known to be partially coherent with the external acoustic sources are therefore used to provide a baseline separation.

4.1 Measurements in closed-section wind tunnel

4.1.1 Experimental setup

The measurements are performed in a closed-section wind-tunnel at École Centrale de Lyon (LMFA laboratory), shown in Fig. 4.1a, within the framework of the ADAPT project. As shown on the sketch in Fig. 4.1b, two sources are mounted in the ceiling of the test-section, excited by two uncorrelated white noises. An array composed of 76 Microelectromechanical systems (MEMS) microphones is mounted in the floor of the section, arranged as shown on Fig. 4.1c. The microphone interspacing varies from 0.2 cm to 27.4 cm. The acquisitions are performed synchronously, during 30 s, and the CSMs are computed with a frequency resolution of 16 Hz, Hanning window and 66 % overlapping rate (the apparent number of snapshots is thus 994[1]).

Three measurements are performed with the MEMS array:

- **configuration A** : with the sources switched on and without flow,
- **configuration T30** : without sources and with a flow at 30 m/s,
- **configuration AT30** : with the sources switched on and the flow at 30 m/s.

[1]The apparent number of snapshots takes into account the window type and the overlapping rate to compensate for the redundancy between the snapshots induced by the overlapping (see for example Welch (1967); Antoni and Schoukens (2009)).

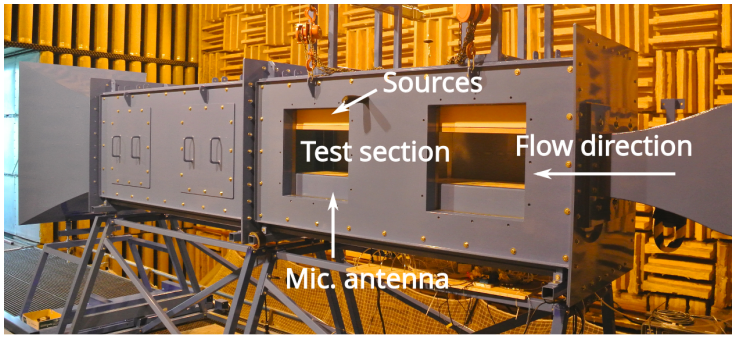

(a) Picture of the facility

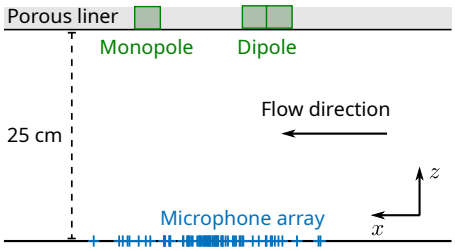

(b) Sketch of the test section (side view)

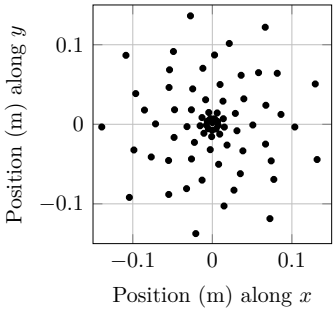

(c) MEMS antenna design

Figure 4.1: Description of the experimental setup for the wind-tunnel measurements.

The objective is to separate the acoustic and TBL contributions from the measurements AT30 and compare them with the baseline measurements A and T30. Note that the proposed separation processes do not compensate for the convection effect on the acoustic part. Therefore, the identified acoustic part cannot be exactly similar to the not-convected measurement A.

Another measurement is performed in the same wind-tunnel using a dense rotating linear array in place of the MEMS array. This array is made of 63 remote microphones spaced by 1 mm. The measurement is performed only in the T30 configuration and for three angular positions: parallel, normal and at $\pi/4$ rad from the flow axis. The records last 60 s, and the CSMs are computed with a 4 Hz resolution, and 66% overlapping rate. As this type of array is much denser than the MEMS one, it is supposed to be more appropriate to characterize the TBL.

4.1.2 Beamforming maps of the measurements

The wavenumber content of the measurements is shown in the form of a k_x-k_y map at 2096 Hz in Fig. 4.2. It is computed by means of a plane wave beamforming process, as given in Eq. (1.3.2), but skipping the autospectra thanks to a vectorized computation, such as in Leclère et al. (2021). By doing so, only the cross-spectra are represented

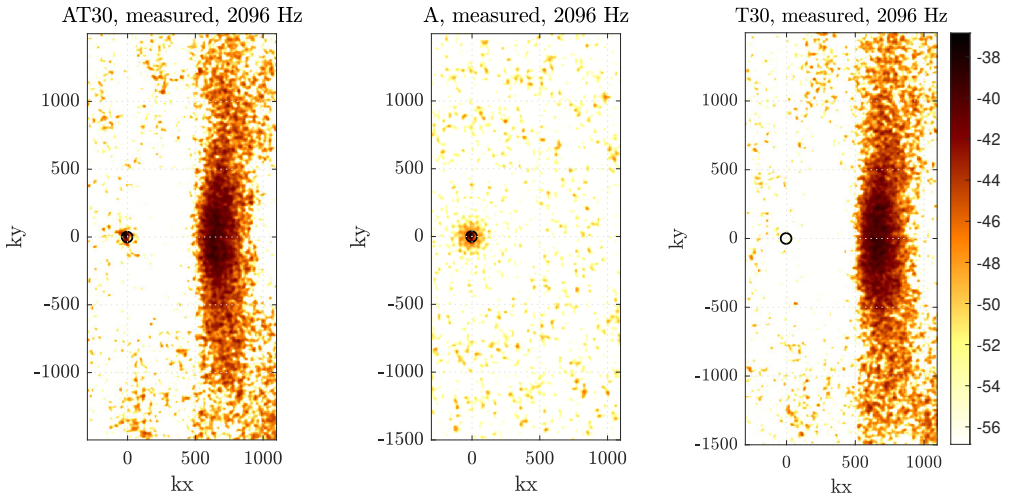

(a) AT30 configuration **(b)** A configuration **(c)** T30 configuration

Figure 4.2: Beamforming maps obtained at 2096 Hz **from the measurement** configurations AT30 (left), A (center), T30 (right), using the MEMS array. The three maps are scaled with the same color bar (in dB). The black circle indicates the convected acoustic domain.

by the beamforming maps. On these maps is plotted in black the convected acoustic circle (given by Eq. (1.3.1)). At this frequency, the acoustic and TBL domains are clearly visible, without overlapping on such a k space representation.

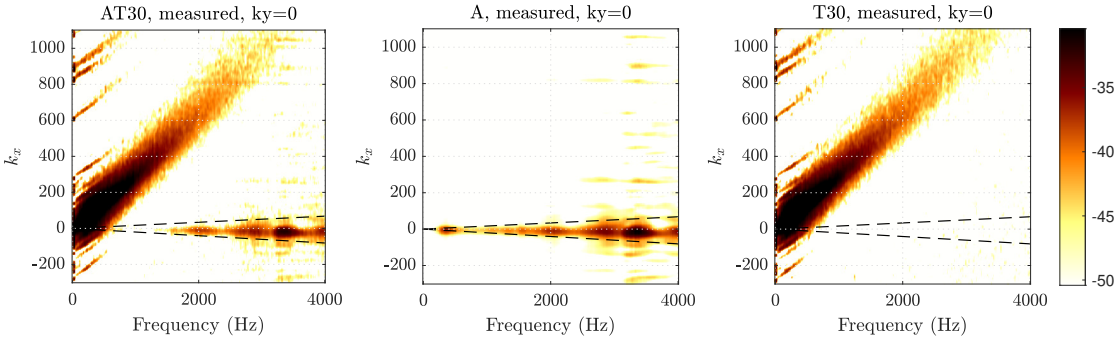

(a) AT30 configuration **(b)** A configuration **(c)** T30 configuration

Figure 4.3: Beamforming maps, as a function of the frequency at $k_y = 0$, **from the measurement** configurations AT30 (left), A (center), T30 (right), using the MEMS array. The three maps are scaled with the same color bar (in dB). The two black dashed lines indicate the acoustic domain.

The wavenumber content is also shown in the form of a k_x-f map, at $k_y = 0$, in Fig. 4.3. On these maps is also plotted the acoustic circle, that appears as a cone nearly centered on $k_x = 0$. These maps show that the two domains overlap below 500 Hz. At low frequencies, the convective ridge is duplicated along the

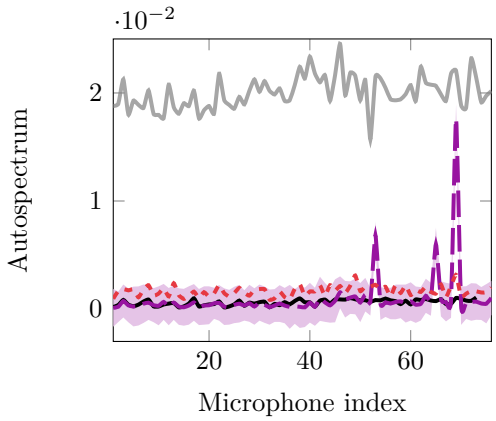

Figure 4.4: Example of the autospecta at 3008 Hz denoised with RPCA (- - -), FA (——) and its 95% credible interval (▭), along with the baseline source autospectra (——) and the raw measurements (——).

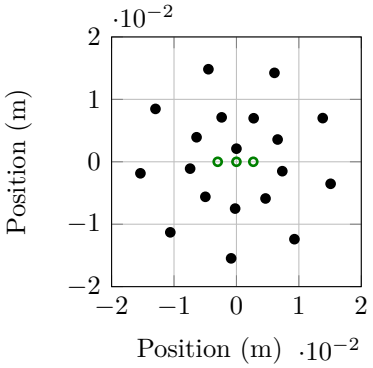

Figure 4.5: Enlarged center part of the antenna.

k_x axis because of aliasing effects. This aliasing is also visible above 3 kHz, on the map of the configuration A, leading to some duplications of the acoustic spot. It is also clear that the order of magnitude of each contribution is very different depending on the frequency.

4.1.3 Denoising with uncorrelated noise models

In this section, some results from several denoising methods which rely on an uncorrelated TBL noise model are given. Some methods from the literature are compared with the FA approach. For the latter method, the prior parameters and initial values are the same as those given in Sec. 2.3.2.1 and Sec. 2.4.4.1.

These results are presented without taking into account the denoising of 3 of the 76 microphones. Indeed, as three microphones of the antenna are very close to each other, the TBL noise is strongly correlated on them and their denoising provided by FA is very low since they are particularly far from the assumptions of uncorrelated noise. An example of autospectra denoised by FA (solved with the Markov Chain Monte Carlo (MCMC) algorithm) and Robust Principal Component Analysis (RPCA) is given in Fig. 4.4. It is visible that three microphones are poorly denoised by FA, corresponding to the three microphones represented by green circles on Fig. 4.5, which are separated by only 3 mm and aligned along the flow direction.

The reconstruction error presented below is calculated as follows:

$$\delta = \frac{\left\| \mathrm{diag}(\boldsymbol{S}_{aa}^{\star}) - \mathrm{diag}\left(\tilde{\boldsymbol{S}}_{aa}\right) \right\|_2}{\left\| \mathrm{diag}(\boldsymbol{S}_{aa}^{\star}) \right\|_2}, \tag{4.1.1}$$

with $\tilde{\boldsymbol{S}}_{aa}$ is the denoised CSM and $\boldsymbol{S}^{\star}_{aa}$ is the baseline source CSM. Using an ℓ_2 norm for this error gives more weight to the outliers and therefore, including the problematic microphones in the calculation causes the error to be much higher for FA than for RPCA, while all the other autospectra are much better reconstructed by FA than by RPCA.

It could be possible to exclude these microphones from the dataset, however their presence has very little impact on the denoising of other microphones and they will further be useful for the identification of TBL noise for the FA-Corr method. Therefore, these channels are included during the separation processes but excluded from all the results presented below.

4.1.3.1 Denoised autospectra

Fig. 4.6a shows the autospectra, averaged over the microphones, of various CSMs denoised with Diagonal Reconstruction (DRec), RPCA, Canonical Coherence Analysis (CCA), FA solved with the MCMC and Expectation-Maximization (EM) algorithm, respectively refer to as FA-MCMC and FA-EM, along with the baseline source autospectrum and the 95% credible interval provided by the FA-MCMC denoising. As the noise may vary over the microphones, the average autospectra may not be fully representative of the denoising level. Therefore, a denoising error that encompass all microphones is also given for each method in Fig. 4.6b, which illustrates the distance from each microphone autospectrum to the corresponding baseline autospectrum, given by Eq. (4.1.1).

In the present section, the analysis is limited to the autospectra of the acoustic part because it gives a good idea of the overall denoising performance of each method. However, in the following, in comparison with the results from FA-Corr, we also present the reconstruction curves of the acoustic cross-spectra (see Fig. 4.14), as well as an analysis of the autospectra of the TBL part (see Fig. 4.15).

It is not possible to have $\tilde{\boldsymbol{S}}_{aa} = \boldsymbol{S}^{\star}_{aa}$ in general, first because of the estimation error due to the limited number of snapshots and second, because of the convection effect. Indeed, the denoised CSM contains the acoustical part subjected to a convection effect, which is not compensated by the denoising process, whereas the baseline source CSM comes from measurements without any convection effect. Therefore, even after an optimal denoising, the denoising error should be limited by these two thresholds, which are numerically evaluated further below.

The major differences between the experimental data and the previous numerical simulations concern the noise properties. In the real measurements, the TBL contribution dominates the data, leading to a very poor signal-to-noise ratio (from

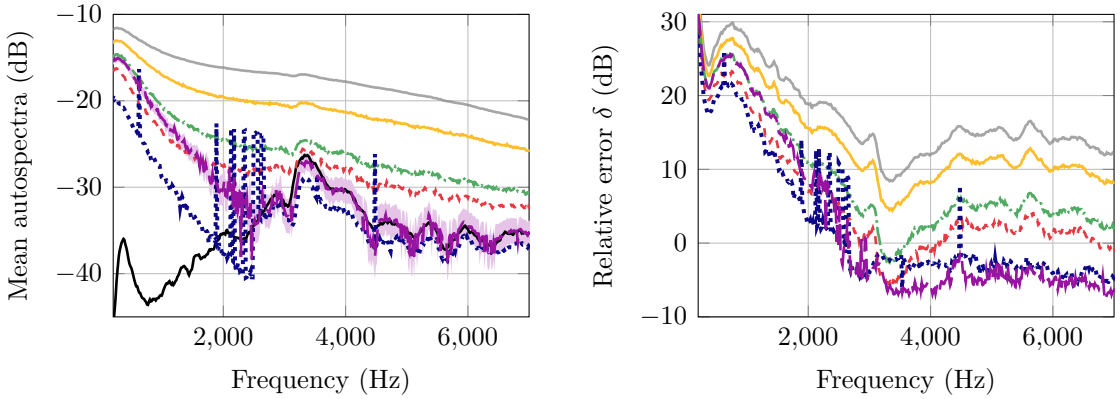

(a) Autospectra from the denoised CSMs, averaged over the microphones.

(b) Denoising error based on the measurements of the sources without flow.

Figure 4.6: Mean autospectra and associated error from CSMs denoised with DRec (——), RPCA with $\lambda = M^{-1/2}$ (- - -), CCA (- - -), FA-MCMC (— —), FA-EM (·····), and the CSM not denoised (——). On (a) is also plotted the baseline mean autospectrum (——) and the 95% credible interval for FA-MCMC ( ).

more than -25dB at low frequencies to -10dB at high frequencies). Moreover, the TBL noise is highly correlated over the microphones in the low frequency range, which does not fulfill the requirements of the denoising methods investigated in the present section. Therefore, low performance is expected from every methods at low frequencies.

CCA and FA associate all the coherent field to the signal CSM, possibly including the one from the TBL noise. Therefore, the signal CSM is overestimated in the frequency range where the TBL noise is highly correlated over the microphones. RPCA provides a more efficient denoising below 1.2 kHz, thanks to the value of the regularization parameter ($\lambda = M^{-1/2}$, M being the number of sensors), which drives the solution to a favorable low-rankness of the signal CSM, and slightly prevent the autospectra from being overestimated.

The denoising performance provided by FA-EM is very variable over frequencies, because the algorithm converges to local maxima that depend on the initialization and the choice of the stopping criteria. Below 2.5 kHz, FA-EM provides a very unstable solution, which sometimes leads to rather high denoising error as compared to those from the other methods, whereas above 2.5 kHz, FA-EM identifies only one equivalent source, which leads to an underestimation of the autospectra.

On the whole frequency range, the efficiency of CCA could be improved by a better thresholding of the canonical coherences, but the appropriate thresholding is hard to set in practice when no information about the real source CSM is available.

Above 2.5 kHz, FA-MCMC provides an estimate of the mean source autospectra very close to the measurement without noise, thanks to a sparse model that leads to an estimation of around 2 uncorrelated components in the acoustic field. However, the denoising error is limited by the convection effect on the acoustic propagation. Indeed, the effect of the flow on the acoustic propagation imposes a lower bound for the denoising error of Eq. (4.1.1). This bound can be evaluated numerically, by simulating the source propagation with and without convection.

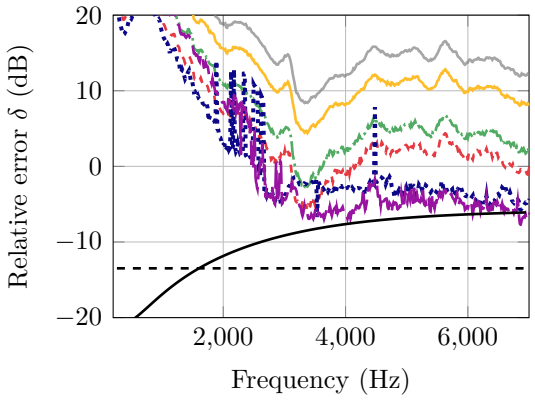

Figure 4.7: Same error curves as in Fig. 4.6b, along with the error due to the convection effect on the acoustic field (——) and the estimation error of the autospectra (- - -).

Knowing the positions for the sources and microphones from the experimental setup, two measurement CSMs are simulated. First, the baseline source CSM is simulated using free-field Green functions:

$$\boldsymbol{H}_{mn} = \frac{\mathrm{e}^{\imath k \|\boldsymbol{r}_{mn}\|_2}}{4\pi \|\boldsymbol{r}_{mn}\|_2}, \tag{4.1.2}$$

where $\boldsymbol{r}_{mn} = \boldsymbol{r}_m - \boldsymbol{r}_n$ is the difference between the microphone m and the source n position vectors. Then, another acoustic CSM is simulated using a convected propagation, in the far field and in a uniform flow (Sijtsma, 2004):

$$\boldsymbol{H}^{\mathrm{conv}}_{mn} = \frac{e^{\imath k \Delta r_{mn}}}{4\pi \sqrt{(\boldsymbol{M} \cdot \boldsymbol{r}_{mn})^2 + \beta^2 \|\boldsymbol{r}_{mn}\|_2^2}} \tag{4.1.3}$$

with $\Delta r_{mn} = \frac{1}{\beta^2}(-\boldsymbol{M} \cdot \boldsymbol{r}_{mn} + \sqrt{(\boldsymbol{M} \cdot \boldsymbol{r}_{mn})^2 + \beta^2 \|\boldsymbol{r}_{mn}\|_2^2})$ and where $\boldsymbol{M}$ is the Mach number vector, $\beta^2 = 1 - \|\boldsymbol{M}\|_2^2$ and $\cdot$ indicates a dot product. The two simulated CSMs are then injected in Eq. (4.1.1) ($\tilde{\boldsymbol{S}}_{aa}$ being the convected acoustic CSM and $\boldsymbol{S}^{\star}_{aa}$ the free-field one) and the error is plotted in Fig. 4.7. This error depends on the frequency because of the directivity of the dipole. On this figure is also plotted the estimation error of the autospectra due to the finite number of snapshots, determined

numerically. One can see that the denoising error from 3.5 kHz is clearly limited by the convection effect on the denoised spectra, but not by the estimation error.

4.1.3.2 Rank of the denoised CSMs

As several denoising methods rely on a low-rankness assumption for the acoustic CSM, Fig. 4.8 shows the eigenvalues of the denoised CSM at 3 different frequencies. On this figure, one can see that RPCA does not preserve the positive-semidefiniteness of the denoised CSM. A positivity constrain could be added to the RPCA problem, as proposed in Amailland et al. (2018). It is also visible that DRec performs a reduction of the eigenvalues, until the smallest one reaches zero.
An overview of the eigenvalues of the denoised CSM against frequency is also given in Fig. 4.9. The number of significant eigenvalues are plotted on this figure – an eigenvalue is arbitrarily considered significant if it is greater than 1% of the highest one. At low frequencies, all the methods overestimate the rank of the denoised CSM, because of the correlation of the TBL noise over the microphones, whereas FA-EM often provides only one significant eigenvalue (which is related to the underestimation of the mean autospectra on Fig. 4.6a). Above 2700 Hz, FA-MCMC provides a CSM with a number of significant eigenvalues close to 2, with an estimation of only one source in the region where the acoustic signal is low, corresponding to destructive interferences due to the tunnel geometry. The CSMs denoised by CCA have a nearly constant number of significant eigenvalues, due to the thresholding step during the denoising process. In general, the experimental setup with 2 uncorrelated sources is favorable to the FA-MCMC approach which is able, thanks to its strong sparsity constraint, to provide a very low-rank CSM.

4.1.4 Separation using FA-Corr

4.1.4.1 Estimation of the TBL parameters from NLLS

In order to estimate the Corcos' parameters required to apply the separation process, the NLLS procedure described in Sec. 3.3.1 is followed. First, the measurement from the three positions of the rotating array, at configuration T30, is used, because this antenna is supposed to be reliable for the characterization of the TBL. Then, NLLS is also applied on the MEMS measurements, at configuration AT30 to see if the strategy can be applied on measurements acquired with a less dense array and in the presence of an acoustic field.

In Fig. 4.10 are plotted the estimated parameters from the two datasets, as a function of the frequency. The longitudinal (along the stream direction, following

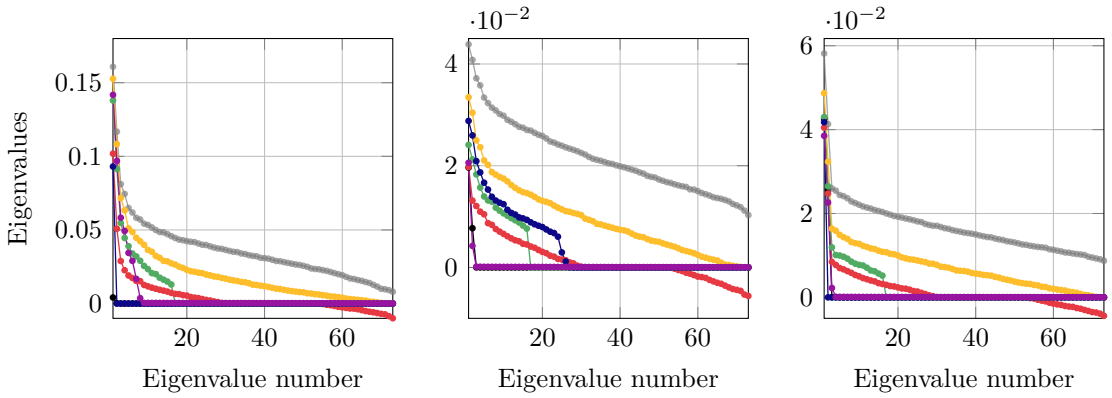

(a) At 1008 Hz **(b)** At 2512 Hz **(c)** At 4000 Hz

Figure 4.8: Eigenvalues of the CSM denoised with: DRec (••••••), RPCA with $\lambda = M^{-1/2}$ (••••••), CCA (••••••), FA-MCMC (••••••), FA-EM (••••••), no denoising (••••••). Eigenvalues of the baseline source measurements are also plotted (••••••) .

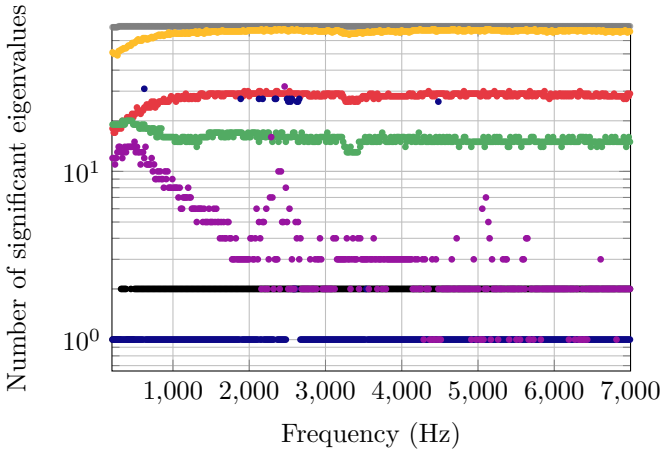

Figure 4.9: Number of significant eigenvalues of the CSM denoised with DRec (••••••), RPCA with $\lambda = M^{-1/2}$ (••••••), CCA (••••••), FA-MCMC (••••••), FA-EM (••••••), also of the CSM not denoised (••••••) and of the baseline source CSM (••••••) . The significant eigenvalues are those greater than 1% of the highest eigenvalue.

the x-direction) and transverse (normal to the stream, along y-direction) correlation lengths are calculated as:

$$L_{c_{x,y}} = \frac{U_c}{2\pi f \alpha_{x,y}}. \tag{4.1.4}$$

The two arrays and configurations give very similar results at low frequency, but above 5 kHz, the interspacing of the MEMS microphones is too high to provide an accurate estimate. The estimated convection speed follows a classical decrease, as described in the literature (Arguillat et al., 2010; Schloemer, 1966). Similarly, the evolution of the correlations lengths with frequency is well known (Farabee

and Casarella, 1991).

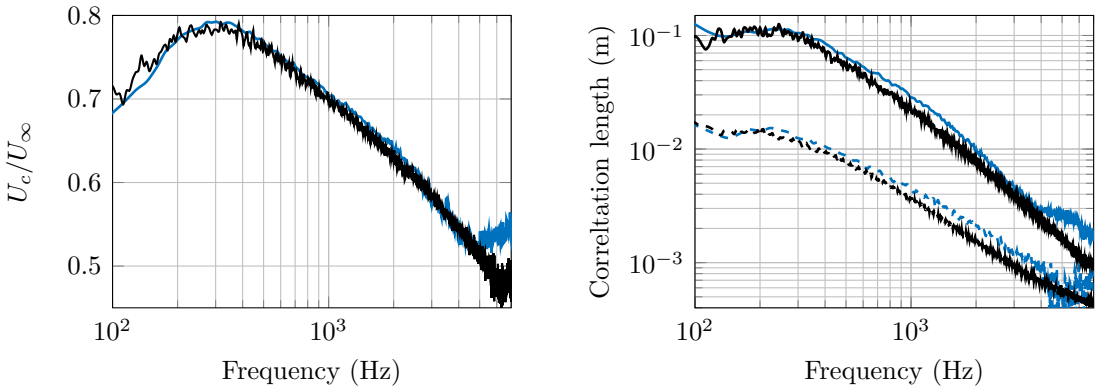

(a) Normalized convection speed

(b) Longitudinal (solid line) and transverse (dashed line) correlation lengths

Figure 4.10: Convection speed (a) ; longitudinal (solid line) and transverse (dashed line) correlations lengths (b) estimated using NLLS on the T30 measurements with the rotating array (—) and on the AT30 measurements with the MEMS array (—).

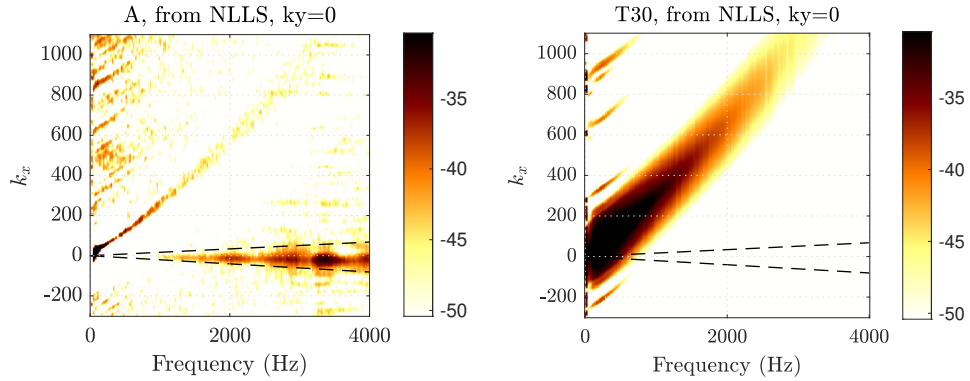

(a) Acoustic part

(b) TBL part

Figure 4.11: Beamforming maps obtained at $k_y = 0$ **from the NLLS regression** applied to the AT30 measurements. Identification of the acoustic (left) and the TBL (right) contributions. The two maps are scaled with the same color bar (in dB). The two black dashed lines indicate the acoustic domain.

In order to evaluate the capacity of the NLLS procedure to separate the acoustic and TBL contributions, the k_x-f beamforming maps are shown in Fig. 4.11. The TBL part results from the Corcos' model with the identified parameters whereas the acoustic part results from the subtraction of the TBL CSM from the measurement CSM.

Compared to the AT30 beamforming maps, the TBL contribution seems clearly lowered, even if a ridge still persists around the convective wavenumber. The

Fig. 4.11b is very similar to the map of the T30 measurements, which shows that the Corcos' model is able to well describe the TBL contribution in $k_y = 0$.

4.1.4.2 Estimation of the TBL parameters from FA-Corr

Several approaches can be employed to apply the FA-Corr separation to the measurements:

- use the TBL parameters inferred with NLLS as prior parameters and initial values, and update these parameters during FA-Corr,
- use any arbitrary values for the TBL prior parameters and initialization, and update them during FA-Corr,
- use the TBL parameters inferred with NLLS as prior parameters and initial values, and do not update them,
- use any arbitrary values for the TBL prior parameters and initialization, and do not update them.

As the solution provided by the MCMC solver is theoretically independent from the initialization, the strategies mainly differs in the prior mean and shape. Another strategy for the initialization of FA-Corr could be to employ the TBL parameters inferred from the rotative antenna. However, this case is not treated here, in order to remain in a general case where only the MEMS array is available. For all the other parameters and priors, the same values as given in Sec. 3.4.1 are employed.

The updated TBL parameters from the two first strategies are shown in Fig. 4.12 along with the associated initial and prior values. The arbitrary initial values and prior means are $\boldsymbol{\theta} = \{U_c, \alpha_x, \alpha_y\} = \{16,\ 0.3,\ 1.2\}$ and the arbitrary prior variance is $\boldsymbol{\Sigma}_\theta^2 = \lceil 4, 0.001, 0.05 \rfloor$, which are deliberately chosen far from the values given by the NLLS procedure, in order to evaluate the ability of the FA-Corr method to update the TBL parameters to fit the data, given the priors.

The TBL parameters update by FA-Corr are similar with the different priors and the two different initializations. This shows that the NLLS procedure is not essential, although it is useful to reduce the iteration number of the sampler, and therefore lower the computation time. For the present application, thanks to the NLLS initialization, the number of iterations for one frequency line is reduced from 2500 to 1000, which reduces the computation time from 42 s to 17 s per frequency, while an NLLS optimization takes less than 0.1 s per frequency.

The update of the parameters provided by FA-Corr is moderate, and it is shown in the following that the effect of this small correction in terms of reconstruction error of the acoustic and TBL parts is small.

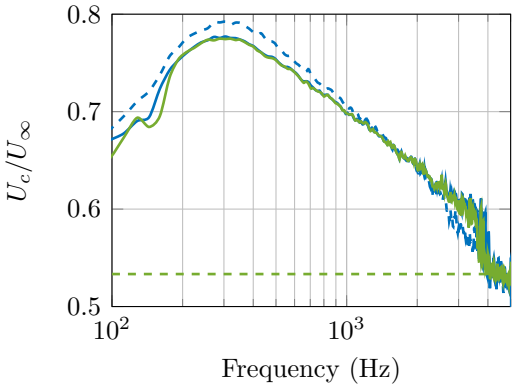

(a) Normalized convection speed.

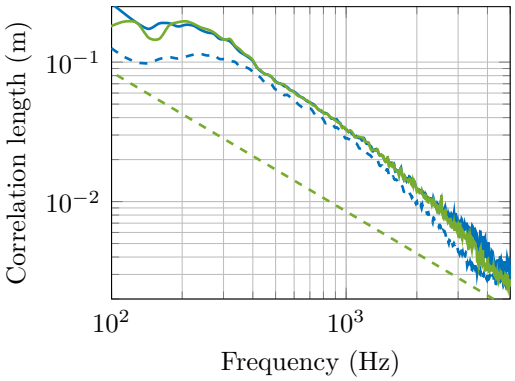

(b) Longitudinal correlation length.

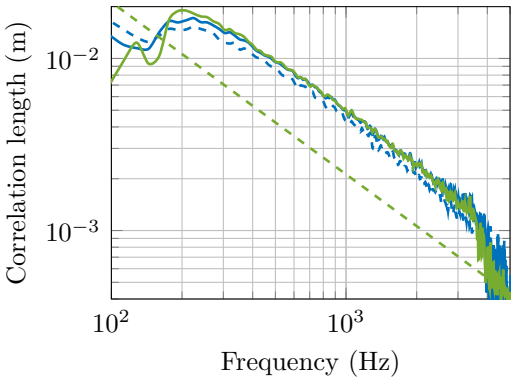

(c) Transverse correlation length.

Figure 4.12: Initial values and priors for FA-Corr: from NLLS (- - -) and arbitrary values (- - -). Estimations from FA-Corr using NNLS (——) and arbitrary values (——) for the initialization and priors.

4.1.4.3 Reconstruction of the acoustic part

The identification of the acoustic contribution is evaluated by plotting the autospectra and the absolute value of the cross-spectra, as well as their associated error obtained from the baseline measurement of the source only (configuration A), in Fig. 4.13 and Fig. 4.14.

For the autospectra, the plotted error is defined as previously (see Eq. (4.1.1)), whereas for the cross-spectra, the error is defined similarly:

$$\delta_{\text{off}} = \frac{\left\| \boldsymbol{S}^{\star}_{aa} - \tilde{\boldsymbol{S}}_{aa} - \left\lceil \text{diag}\left(\boldsymbol{S}^{\star}_{aa} - \tilde{\boldsymbol{S}}_{aa}\right) \right\rfloor \right\|_F}{\| \boldsymbol{S}^{\star}_{aa} - \lceil \text{diag}(\boldsymbol{S}^{\star}_{aa}) \rfloor \|_F}. \tag{4.1.5}$$

On these figures are compared the results from the four strategies described just before (in Sec. 4.1.4.2), along with the FA-MCMC (further refers to as FA) and RPCA methods. The results are given for the low and medium frequency range 0-5000 Hz, since the differences between the methods are expected to be observed

mainly at low frequency. Note that for these curve, the credible intervals are not given first for a legibility reason, but also because the credible intervals depend on the problem and the priors, and as FA and FA-Corr are based on different model, comparing their credible intervals wouldn't make much sense.

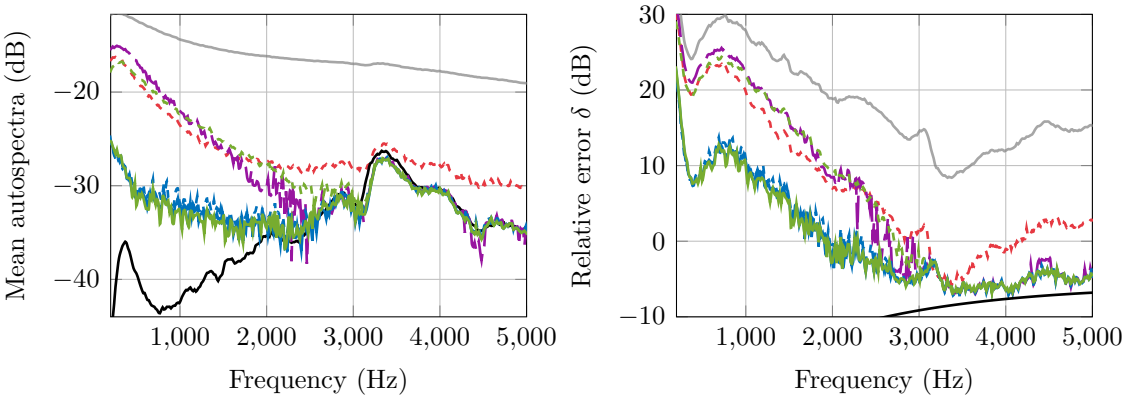

(a) Acoustic autospectra, averaged over the microphones.

(b) Error on the autospectra based on the measurements of the sources without flow.

Figure 4.13: Mean **acoustic autospectra and associated error** from the denoising with RPCA with $\lambda = M^{-1/2}$ (- - -), FA-MCMC (— ·), FA-Corr with (——) and without (- - -) updates of the TBL parameters starting from arbitrary values, with (——) and without (- - -) update from NLLS values and the CSM not denoised (——). On (a) is also plotted the baseline mean autospectrum (——) and on (b) the error due to the convection effect (——).

Looking at the raw measurements, it appears that the cross-spectra decrease much faster than the autospectra with the frequency. Above 2500 Hz, the measured cross-spectrum is very close to the acoustic one, which shows that the contribution of the TBL on the cross-spectra becomes very weak at this point. This is also visible on the wavenumber beamforming of the measurements, on which the TBL spot is low above this frequency. This corresponds to longitudinal and transverse correlation lengths of the TBL contribution which become much lower than the interspacing of most microphones. Therefore, the main difference between the results from FA and FA-Corr appears in the low frequency range 0-2500 Hz, where the convective ridge is dominant in the measurements. On this frequency range, the autospectra and cross-spectra levels as well as the reconstruction error are much lower for three of the four FA-Corr strategies. Among the four FA-Corr strategies, the poorest one is unsurprisingly the one with an arbitrary initialization and without update, which gives results similar to FA. The three others are equivalent for both the autospectra and the cross-spectra. Among these four approaches, the one

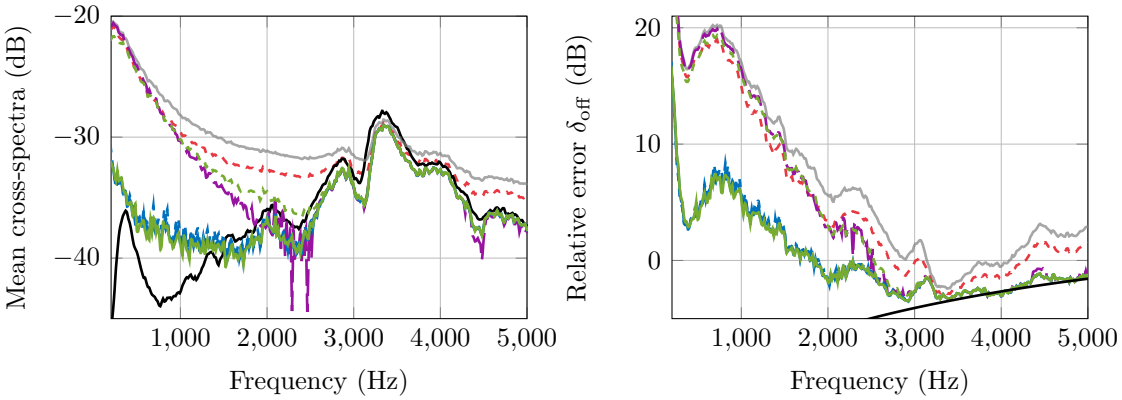

(a) Absolute value of the **acoustic cross-spectra** averaged over the microphones.

(b) Error on the cross-spectra based on the measurements of the sources without flow.

Figure 4.14: Mean absolute value of the **acoustic cross-spectra and associated error** from the separation with RPCA with $\lambda = M^{-1/2}$ (- - -), FA-MCMC (— ·), FA-Corr with (——) and without (- - -) updates of the TBL parameters starting from arbitrary values, with (——) and without (- - -) update from NLLS values and the CSM not denoised (——). On (a) is also plotted the baseline mean cross-spectrum (——) and on (b) the error due to the convection effect (——).

with NLLS initialization and no update can therefore be recommended, since it has the lowest computational cost.

Concerning the RPCA method, its performance is similar to FA at low frequencies, and are then poorer than the Bayesian approaches, except when the acoustic-to-TBL ratio becomes greater than -10 dB.

4.1.4.4 Reconstruction of the TBL part

Then, in order to evaluate the reconstruction of the TBL part, the autospectra and the absolute value of the cross-spectra identified by each approach are plotted in Fig. 4.15 and Fig. 4.16 respectively, along with the associated error based on the measurement of the flow only (configuration T). No curve is plotted concerning the cross-spectra from the FA method since it only infers the autospectra for the TBL part.

The mean autospectra of the T and AT30 configurations overlap over most of the frequency range, since the acoustic-to-TBL ratio is very low. Therefore, it is difficult to evaluate the performance of the reconstructed TBL part by the various methods, looking at the autospectra, and concerning the corresponding error, it is bounded by the estimation error related to the limited number of snapshots. However, it is possible to see that the RPCA results are poorer than the FA's one and the worst results are provided by FA-Corr with arbitrary initialization

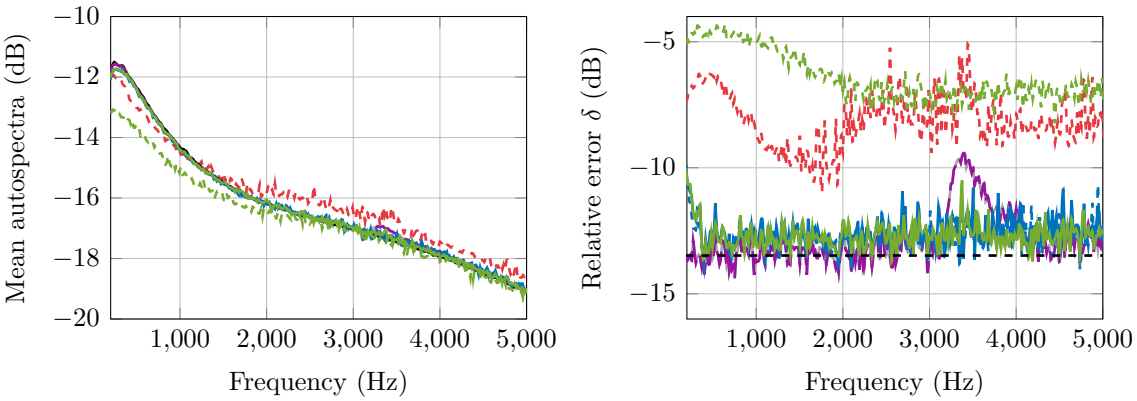

(a) TBL autospectra, averaged over the microphones.

(b) Error on the autospectra based on the measurements of the flow without sources.

Figure 4.15: Mean **TBL autospectra and associated error** from the separation with RPCA with $\lambda = M^{-1/2}$ (- - -), FA-MCMC (— ·), FA-Corr with (——) and without (- - -) updates of the TBL parameters starting from arbitrary values, with (——) and without (- - -) update starting from NLLS values and the CSM not denoised (——). On (a) is also plotted the TBL mean autospectrum (——) and the estimation error of the autospectra (- - -) is indicated on (b).

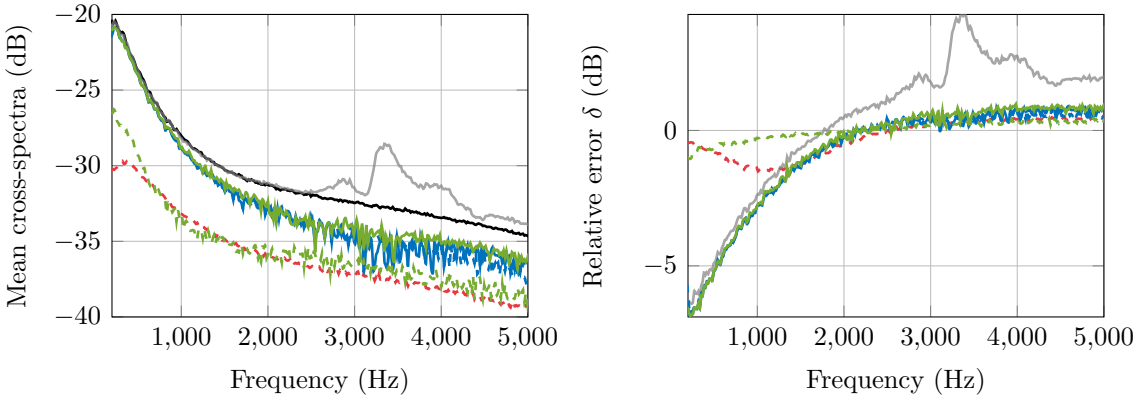

(a) Absolute value of the **TBL cross-spectra** averaged over the microphones.

(b) Error on the cross-spectra based on the measurements of the flow without sources.

Figure 4.16: Mean absolute value of the **TBL cross-spectra and associated error** from the separation with RPCA with $\lambda = M^{-1/2}$ (- - -), FA-MCMC (— ·), FA-Corr with (——) and without (- - -) updates of the TBL parameters starting from arbitrary values, with (——) and without (- - -) update from NLLS values and the CSM not denoised (——). On (a) is also plotted the TBL mean cross-spectrum (——).

without update of the TBL parameters. These curves also prove that for this kind of acoustic-to-TBL ratio, integrating a TBL autospectrum model such as those found in the literature (Hwang et al., 2009) would not be very relevant.

Below 2000 Hz, the mean cross-spectra of the AT and T measurements overlap, which indicates that the TBL dominates the cross-spectra. Therefore, at low

frequency, the error on the cross-spectra is the same with and without applying the separation process, except for RPCA for which most of the identified cross-spectra are null, leading to an error that remains close to 0 dB.

The error curves from FA-Corr increases with the frequency because a large number of the cross-spectra have an expected value very close to zero, and this number increases with the frequency. These cross-spectra induce a high threshold on the error, this threshold being related to the residual coherence between the microphones, which in turn depends on the number of snapshots and also on the small acoustic contribution present on the T baseline measurement. This error curve could be plotted without the microphone pairs of low coherence, however, the residual coherence threshold is difficult to determine in this case. Therefore, the FA-Corr curves tend toward $\sqrt{2} = 1.5$ dB with the increasing frequency, which is the estimation error for the limit case where all the cross-spectra have a null expectation.

4.1.4.5 Wavenumber beamforming maps

To complement the previous analyses, the wavenumber beamforming maps of the acoustic part identified with FA are given in Fig. 4.17, as well as the two contributions from the separation done by FA-Corr with the NLLS initialization and without update of the TBL parameters in Fig. 4.18. As the autospectra are not taken into account for the calculation of these maps, the dynamic is improved and only the reconstruction of the cross-spectra are represented.

For the two methods, the beamforming map of the residuals is also given. The residuals are calculated as follows for FA:

$$\boldsymbol{R}^{\text{FA}} = \hat{\boldsymbol{S}}_{yy} - \left(\tilde{\boldsymbol{S}}_{aa} + \lceil \tilde{\boldsymbol{\sigma}}_n^2 \rfloor\right) \tag{4.1.6}$$

and for FA-Corr:

$$\boldsymbol{R}^{\text{FA-Corr}} = \hat{\boldsymbol{S}}_{yy} - \left(\tilde{\boldsymbol{S}}_{aa} + \tilde{\boldsymbol{S}}_{nn} + \tilde{\boldsymbol{S}}_{\epsilon\epsilon}\right). \tag{4.1.7}$$

Since FA is based on a diagonal TBL noise model, the acoustic cross-spectra remain imprinted by the TBL, especially in the low frequencies. Therefore, the acoustic map is very similar to the measurements (in Sec. 4.1.2). The beamforming maps for the RPCA results are not given since, as FA, it improves mainly the autospectra, which provides very similar results.

On the beamforming maps of the acoustic part identified by FA-Corr, the convective ridge is well reduced as compared to the measurement map, and even seems totally removed, except below 220 Hz, where the TBL noise is highly correlated

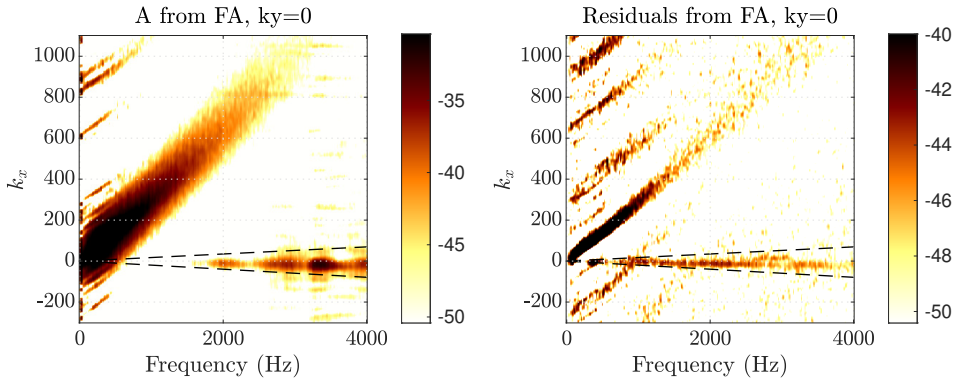

(a) Acoustic part **(b)** Residuals

Figure 4.17: Beamforming maps obtained at $k_y = 0$ **from the FA identification** applied to the AT30 measurements. Identification of the acoustic part (left) and the residuals (right). The two black dashed lines indicate the acoustic domain.

over the microphones and where the sources emit at very low amplitudes. Up to 1500 Hz, the acoustic contribution seems to be not well reconstructed compared to the baseline measurement (Fig. 4.3b), which means that even if the cross-spectra are overestimated (visible on Fig. 4.14a), they do not carry any wavenumber information related to an acoustic field. This could be confirmed by advanced acoustic imaging (in space).

The acoustic contribution appears to be removed from the FA-Corr TBL maps in Fig. 4.18b. However, as the missing acoustic contribution below 1500 Hz is not visible on the residual map, it is surely identified within the TBL part.

On this residual map for the FA-Corr method, a small part of the convective ridge persists, as well as a small part of the acoustic contribution. However, the residuals from FA-Corr are lower than those from the FA approach, which shows that the TBL model reduces the fitting error in general.

The separation quality from FA-Corr and the smallness of the residuals indicates that a Corcos' model, adapted such that its parameters vary with the frequency, is suitable for this kind of measurements.

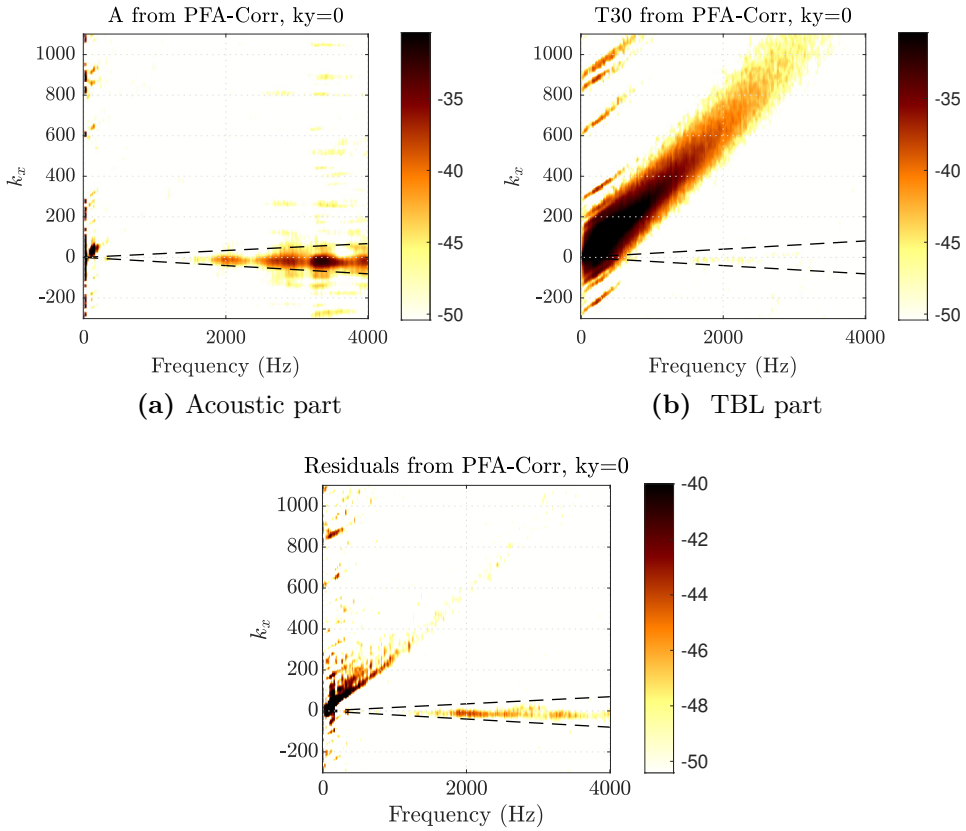

(a) Acoustic part **(b)** TBL part

(c) Residuals

Figure 4.18: Beamforming maps obtained at $k_y = 0$ **from the FA-Corr identification** applied to the AT30 measurements. Identification of the acoustic part (top left), the TBL contribution (top right) and the residual map (bottom). The 2 top maps are scaled with the same color bar (in dB) and the bottom map is scaled on a smaller dynamic range. The two black dashed lines indicate the acoustic domain.

4.2 Application to inflight measurements

4.2.1 Experimental setup

The measurements are performed synchronously by 25 large microphones, flush-mounted on the left side of the fuselage of a large Airbus aircraft. As shown in Fig. 4.19 and Fig. 4.20, the array is behind the wing, specially designed to characterize the engine jet and fan noise. On Fig. 4.19, the units are normalized with the primary jet nozzle diameter. The distance between two consecutive lines is about half a diameter. Each records lasts 60 s, and the CSMs are computed with a resolution of 4 Hz, with 66% overlapping rate (the apparent number of snapshots is thus 497).

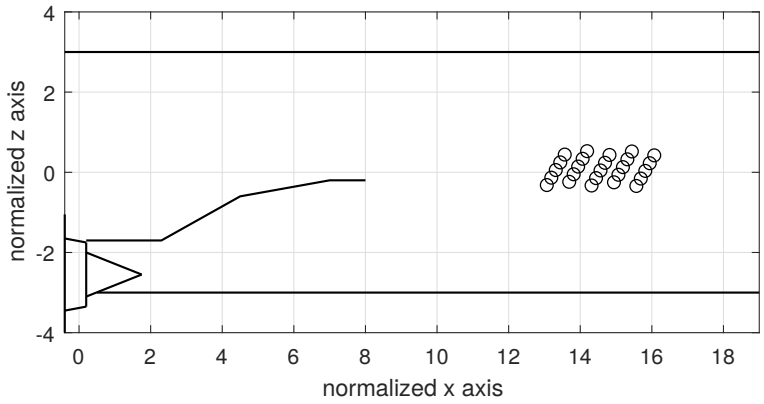

Figure 4.19: Sketch of the microphone configuration on the fuselage. The trailing edge of the wing is drawn in solid line, as well as the rear part of the engine.

Figure 4.20: Picture of the microphone antenna, from Helffer (2018).

The measurements are performed for two configurations. The first one is at idle engine speed, and is considered to contain mainly TBL noise. The second one

is a cruise configuration, at high engine power. For these two configurations, the aircraft is traveling at Mach number 0.85, at a classical cruise flight altitude (about 10 km high).

The recording conditions are thus very different from the wind-tunnel experiment: the number of sensors is much lower, the flow Mach number is much higher and the physical conditions are known to vary along the fuselage (Palumbo, 2012), which may lead to inhomogeneous TBL pressure fields over the antenna. Moreover, the microphone arrangement is very regular, which is prompt to produce aliasing on the beamforming maps.

Note that in the following, the fuselage area on which the array is mounted is assumed to have a negligible curvature, which in practice, can have an impact on the TBL characteristics.

Also, thereafter, in order to fit a Corcos' model over the measurements, the angle of the flow has to be known. However, with the present array configuration, the microphones are too far apart to be able to determine it precisely. On the $k_x - k_y$ beamforming maps, the convective ridge is imprinted by a strong aliasing, which makes it impossible to study its tilt. Therefore, the flow is considered to be orientated along the horizontal axis (x axis), which is a bit different from what has been observed in the literature (Haxter and Spehr, 2019, 2017).

4.2.2 Beamforming maps of the measurements

The beamforming maps of the idle and cruise configurations are given in Fig. 4.21 scaled on two frequency bands. On these maps is also plotted the convected acoustic circle (dashed line), which is strongly shifted toward the negative wavenumbers, due to the high convection speed.

The cruise configuration shows a wavenumber content inside the acoustic circle, compared to the idle configuration. A solid black line also indicates an approximated location of the convective ridge. The position of the ridge increases linearly with the frequency, which supposes that the convection speed is constant with the frequency. The convective ridge is duplicated many times along the k_x due to a strong aliasing. The TBL contribution dominates the cross-spectra mainly up to Strouhal number 4 therefore, in the following, the separation results are shown only in the low frequency range, corresponding to jet Strouhal number going from 0 to 3.85. This Strouhal range is computed from equivalent jet diameter and velocity

$$St = \frac{f D_e}{U_e}, \tag{4.2.1}$$

where the equivalent velocity U_e and diameter D_e are computed using the mass flow rates of the primary and secondary jets, as described in Lu (1986).

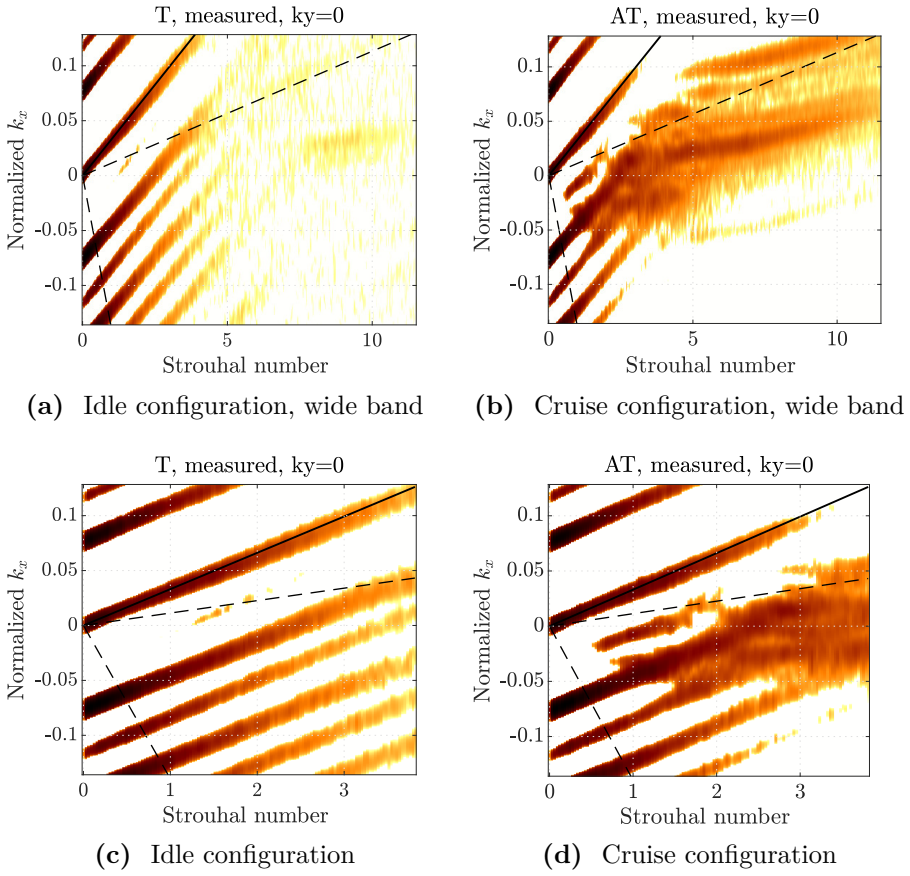

(a) Idle configuration, wide band **(b)** Cruise configuration, wide band

(c) Idle configuration **(d)** Cruise configuration

Figure 4.21: Beamforming maps obtained at $k_y = 0$ **from the measurements** at idle (left) and cruise (right) configuration, on a wide frequency band (top) and zoomed in on the low frequency band (bottom). The four maps are scaled with the same color bar (in dB), with 40 dB of dynamic range. The two black dashed lines indicate the acoustic domain, and the solid line is an approximation of the center of the convective ridge.

4.2.3 Estimation of the TBL parameters

The Corcos' parameters are first estimated using the NLLS procedure. The resulting convection speed and correlation lengths are given in Fig. 4.22. On this figure are also plotted the parameters estimated by FA-Corr starting from the NLLS values. The microphone interspacings being high, the TBL parameters can be estimated only in the low frequencies. As expected from the beamforming maps, the estimated convection speed is nearly constant with the frequency. FA-Corr only modifies the correlation in the low frequencies.

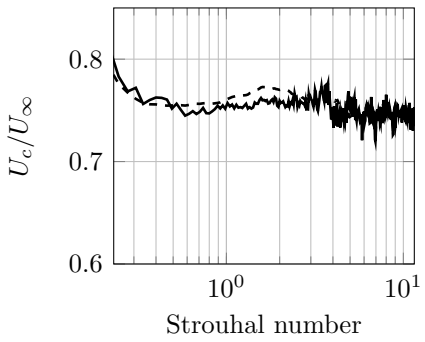

(a) Normalized convection speed

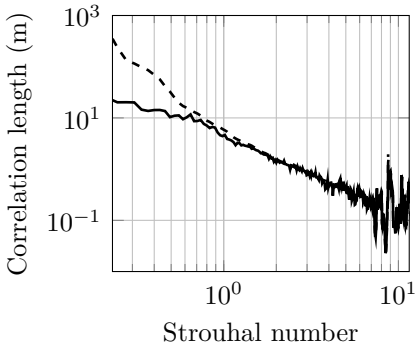

(b) Longitudinal correlation length

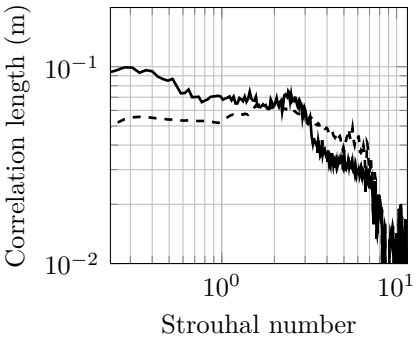

(c) Transverse correlation length

Figure 4.22: Convection speed (a), longitudinal (b) and transverse correlations lengths (c) estimated using NLLS on the measurement in idle configuration (**- - -**) and from FA-Corr (**——**).

4.2.4 Comparison with a reference-based denoising

The noise affecting fuselage microphones is mainly attributed to the contribution of the TBL. In cases where some noise-free reference signals are available, recorded simultaneously with the microphone array signals, it is possible reduce the TBL contribution over microphones measurements. Let $\boldsymbol{x}$ and $\boldsymbol{y}$ stand for a set of reference and array microphone signals, respectively. The CSM of the outputs conditioned by references is given by

$$\boldsymbol{S}_{yy}^{x} = \boldsymbol{S}_{yx}\ \boldsymbol{S}_{xx}^{-1}\ \boldsymbol{S}_{xy}. \tag{4.2.2}$$

This formulation is accordance with Bendat and Piersol's Conditioned Spectral Analysis Bendat and Piersol (1980): autospectra on the diagonal of $\boldsymbol{S}_{yy}^{x}$ are corresponding to multiple coherent output spectra, the multiple coherence being directly given by the ratio between diagonal terms of $\boldsymbol{S}_{yy}^{x}$ and $\boldsymbol{S}_{yy}$.

Note that this denoising approach assumes that the noise affecting the output signals is not contributing to references. References are not necessarily completely noise-free, however the noise affecting references has to be independent from the noise

contributing to the microphone array. Even if the assumptions and required data are different for the reference-based denoising and the Bayesian separation approaches, a good agreement between their results can be considered as a cross validation of both approaches. Their separation results are thus compared in the following.

For the considered experimental application, reference signals are 6 accelerometers and 9 microphones positioned on the inner side of the fuselage and inside the aircraft cabin, respectively. Those sensors are used as references because they are supposed to be much less affected by the TBL than external microphones : the fuselage is known to act as a low-pass filter in the wavenumber domain, the acoustic-to-TBL ratio of inside sensors is thus expected to be much more favorable. Moreover, the remaining TBL contribution on references results from the TBL excitation on the whole fuselage, that is expected to be almost incoherent with the TBL contribution to the 25 microphones covering a very small part of the whole fuselage. On the other hand, inside microphones are also disturbed by interior noise sources, mainly the air conditioning system. However, this noise being independent from the TBL, this should not cause any issue.

4.2.5 Estimation of the acoustic autospectra

In order to have an idea of the reduction of the TBL contribution over the diagonal elements of the acoustic CSMs, the mean autospectra of the acoustic part identified with several approaches are given in Fig. 4.23. The compared approaches are

- the reference-based denoising as described in the previous section,
- FA solved with the MCMC approach,
- the background subtraction method, introduced by Bahr and Horne (2017) and described in Sec. 1.4.3, using the idle configuration as the background noise,
- FA-Corr starting from NLLS TBL values and with the sampling of these parameters.

Above the Strouhal number 11.5, as the TBL parameters estimated with NLLS varies a lot, values averaged from the lower frequency lines are used for the starting parameters of the FA-Corr approach.

The mean autospectra is about 3 dB higher for the cruise configuration than for the idle configuration. But seeing the level of the various acoustic autospectra, such an augmentation cannot be due to the acoustic contribution. Therefore, this must be due to a modification of the TBL between the two configuration, which is probably not due to the jet since it is rather far from the fuselage (about 6 primary jet nozzle diameters away from the fuselage). Consequently, this difference in amplitude of

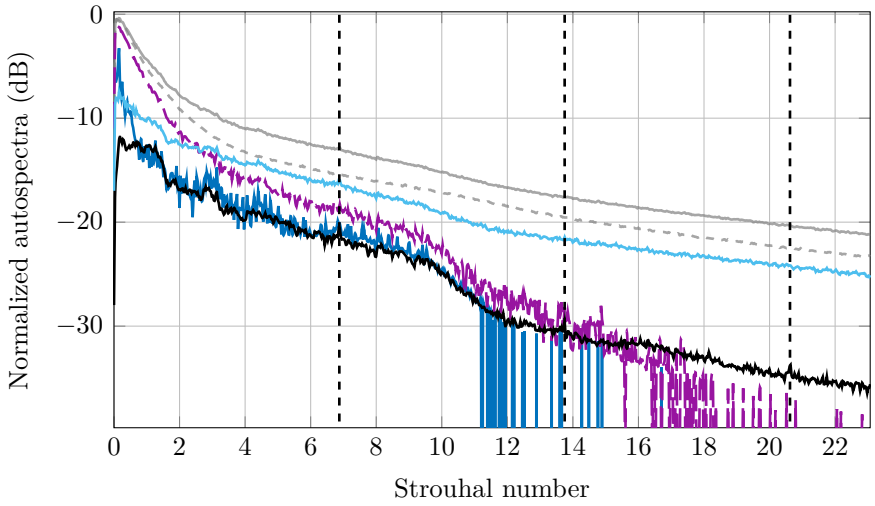

Figure 4.23: Acoustic autospectra averaged over the microphones, from the raw measurements (——), background noise measurements (- - -), after reference-based denoising (——), background subtraction (——), FA denoising (— -) and FA-Corr (——). Vertical lines (- - -) indicate the blade passing frequencies.

the TBL contribution between the idle and the cruise configuration induces a rather small reduction of the autospectra from the background subtraction method.

As for the wind-tunnel application, FA-Corr offers a greater reduction of the autospectra than FA, especially in the very low frequency range (Strouhal between 0 and 3.85). On the Strouhal range 2.3-9.2, the measured spectra is dominated by the BroadBand Shock-Associated Noise (BBSAN), generated by the dual-stream underexpanded supersonic jet (Tam et al., 2009). This noise is produced by the interactions of shock cells in the secondary stream with the convected turbulences in the inner and outer shear layers. Harper-Bourne and Fisher (1973) propose to model this BBSAN by regularly spaced partially coherent monopoles, which correspond to a low number of acoustic sources, in accordance with the FA and FA-Corr assumption. On this frequency range, the reference-based denoising and FA-Corr are in very good agreement whereas the solution of FA is higher since its solution is a bit less sparse than the FA-Corr's one. In appendix E are plotted the eigenvalue distribution for the measurement, and for the FA and FA-Corr solutions as a function of the frequency (Fig. E.1) as well as the number of significant eigenvalues for the same CSMs (Fig. E.2). These figures show that at least one eigenvalue clearly dominates the measurements in the BBSAN frequency range. Whereas at higher frequencies (above Strouhal number 9.2), no eigenvalue dominates the measurements and both FA and FA-Corr fail to reconstruct any coherent spectra.

Note that this frequency corresponds to the limit above which the half convected acoustic wavelength becomes smaller than the smallest microphone interspacing,

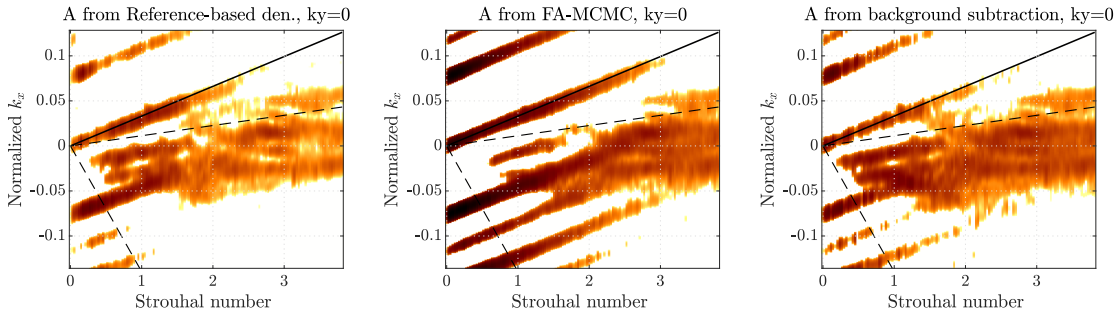

(a) Reference-based denoising **(b)** FA **(c)** Background subtraction

Figure 4.24: Beamforming maps of the acoustic part identified by three approaches. The three maps are scaled with the same color bar as Fig. 4.21 (in dB). On each figure, the two black dashed lines indicate the acoustic domain, and the solid line is an approximation of the center of the convective ridge.

and the longitudinal correlation length also becomes smaller than this smallest microphone distance. Therefore, the acoustic part becomes poorly identifiable and the noise tends to be uncorrelated.

In this frequency range, the autospectra denoised by the reference-based denoising also decreases, but it may reach a lower bound given by the number of reference channels used and the residual coherence between the references and the outer microphones.

4.2.6 Beamforming maps of the separation results

4.2.6.1 Acoustic part from FA, background subtraction and reference-based denoising

The cross-spectra of the acoustic part obtained with the reference-based, FA and background subtraction approaches are now compared by means of wavenumber beamforming maps, shown in Fig. 4.24. Compared to the AT measurement map, the FA's one is almost not modified, since FA relies on an uncorrelated noise model. On the maps from the reference-based denoising and from the background subtraction approach, which are comparable, the convective ridge is still visible, but much lowered.

4.2.6.2 FA-Corr

The beamforming maps of the FA-Corr separation are given in Fig. 4.25. The color bar and dynamic range are similar to the measurement maps (Fig. 4.21). Up to Strouhal number 3, the estimation of the TBL noise is very similar to the measured TBL noise at idle engine speed, which shows that the Corcos' model is suitable to

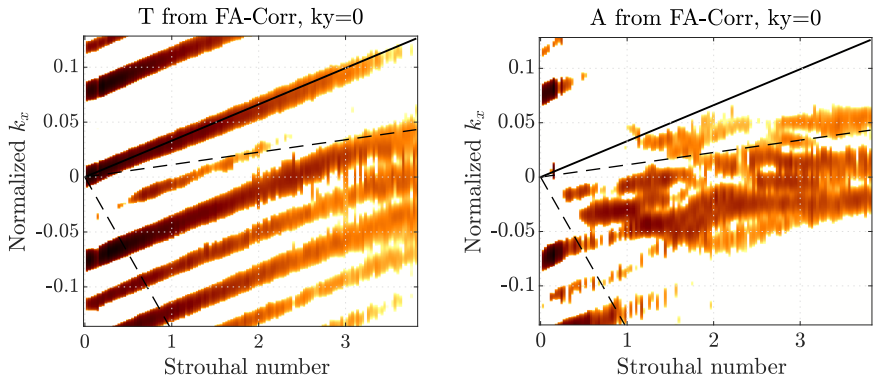

(a) TBL part **(b)** Acoustic part

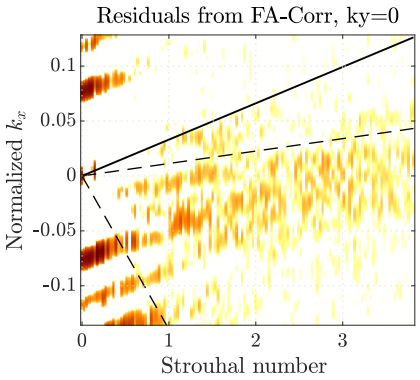

(c) Residuals

Figure 4.25: Beamforming maps obtained at $k_y = 0$ **from the FA-Corr separation**. Identification of the TBL (a) and the acoustic (b) contributions, and residuals (c). The three maps are scaled with the same color bar as Fig. 4.21 (in dB), with 40 dB of dynamic range. The two black dashed lines indicate the acoustic domain, and the solid line is an approximation of the center of the convective ridge.

describe the TBL contribution in the low frequency range. Above Strouhal number 3, the TBL contribution becomes much lower and the identification is less precise.

On the acoustic map, most of the TBL contribution is removed, except in the very low frequencies where a TBL contribution remains at high k_y (visible on a k_x-k_y map) which is then visible on the k_x-f map due to the aliasing effect. The acoustic content identified with FA-Corr has a distribution in the acoustic circle which is similar to the one provided by the reference-based denoising, even if the two methods are based on different requirements and hypotheses. Moreover, the map of the residuals is low. These two observations tend to cross-validate the two approaches.

4.3 Conclusion

In this chapter, several separation approaches have been tested on two different types of measurement. First, the closed wind-tunnel measurements provide a favorable framework for the validation of the methods developed during this thesis, since the acoustic sources and the flow are well known and controlled.

Then, the inflight measurements are a practical application of an industrial concern, where the measurement conditions are less favorable than the wind-tunnel case (Mach number is 10 times higher, number of sensors is 3 times lower, the TBL is inhomogeneous). Therefore, the performance are especially difficult to assess since the flow is very little known and so is the expected acoustic field. A way to validate the separation results is to apply some acoustic imaging process as done in Dinsenmeyer et al. (2019), but some sources require a deep analysis to evaluate whether they make physical sense (see a study about the aeroacoustic sources from the same experiment in Leclère et al. (2020)).

Some trends for the FA and FA-Corr methods can be extracted from the behaviors that are common to both experiments, which complement the numerical studies made in the previous chapters. It appears that FA offers a good reduction of the autospectra but the uncorrelated noise model shows some limits in low frequency where the noise is more correlated and where the convective ridge overlaps the acoustic circle in the wavenumber domain. The FA-Corr model is then more adapted and offers a better separation of the acoustic and TBL parts.

NLLS is a convenient way of initializing the TBL parameters for these applications, which provides a fast convergence and even makes it possible to obtain satisfying separation results by keeping the initial state of these parameters during the separation. However, whether they are identified by NLLS or by FA-Corr, the accuracy of the parameters depends on the array configuration, which should preferably be composed of close enough sensors and ideally with some sensors aligned in different axes related to the flow.

Conclusions and further researches

Conclusions

The separation problem was conducted within a general framework where no reliable measurement of the TBL contribution is available and where the sources generating the acoustic field are not known (in terms of location, number, type of propagation, etc). The literature review on this problem shows that some post-processing methods have already been developed in addition to the experimental approaches to reduce the effect of the TBL contribution on the measurements, especially concerning the diagonal elements of the measurement CSM.

Some methods aiming at reconstructing only the diagonal of the CSMs are computationally inexpensive and easy to implement, but their performance is limited as soon as the noise is correlated over the sensors or when the number of sources is very low, as shown on a numerical benchmark and on closed wind tunnel measurements. Some advanced methods, RPCA and CCA provide a more reliable reduction of the TBL noise, however their performance relies on the setting of empirical parameters, a regularization parameter and a thresholding of the canonical coherences, respectively.

In this context, an alternative post-processing approach has been proposed in this thesis work. The inverse problem of separating the two contributions is based on the differences of the statistical properties of the two pressure fields. The problem is regularized and solved using a Bayesian framework. Two different models have been proposed, the first one relying on an uncorrelated TBL contribution, as it is the case for most of the methods from the literature. This approach is in fact related to the well-known FA problem, adapted to quadratic input data (under the form of a CSM). Like for the other methods in the literature, the assumption of uncorrelated TBL noise is too restrictive in the low frequency range, but this first FA model provides an insight into the possibilities of the Bayesian approach, as compared to the existing methods. Applications on a numerical test case shows some promising reconstruction of the acoustic autospectra and this model is thus extended to give rise to a second approach aiming at improving the separation performance at low frequency.

In this second model, called FA-Corr, the assumptions made for the identification of the acoustic part are preserved, but the TBL noise model is modified, based on the correlation model proposed by Corcos (1963). Some simple numerical test

cases confirm that the problem is identifiable, provided a vague prior knowledge of the TBL physical parameters. As the TBL pressure field often dominates the measurements, it is possible to analyze the coherence loss and the phase shift between the measurement points to get an idea of these parameters. If these parameters are uncertain, they are treated as unknowns of the inverse problem and, the Bayesian approach provides a range of probable values at the end of the separation process.

The last chapter, dedicated to some applications on two very different data sets, highlights the strengths of the two proposed methods. The Bayesian framework offers an intuitive way to regularize the problem, as well as some efficient numerical tools among which the MCMC algorithms that ensure a global convergence of the solver. This approach is very versatile and therefore, the model can be adapted, for example to integrate more constraints, such as the factor shrinkage proposed to enforce the low-rankness of the acoustic CSM. The methods do not require any source propagation model, which is beneficial in cases such as inflight measurements where the propagation is very poorly known.

However, these benefits also comes with some limitations. First, the calculations involved in the numerical solver (the Gibbs sampler) can be cumbersome for the non-specialists, as well as the design of the priors which has to be performed by the user and which is crucial for the proper identification of the inverse problem. Moreover, in Bayesian inference, the solution of the problem is driven by the data, but also by the priors, which sometimes makes the result difficult to interpret. Also, the problem being data-driven, the quality of the separation necessarily depends on the quality of the data, and is therefore limited by the number of sensors, their arrangement, etc. But the experimental applications have proved that an acoustic array can be well adapted to extract the TBL and acoustic contributions, at low and medium frequency. Note that this type of separation can also be used for computational fluid dynamics simulations and, in this case, there is less constraints on the position and number of the measurement points.

Finally, the various applications show how the developed approaches perform as compared to those from the literature and it follows that in the low and medium frequency range, FA-Corr is more efficient for the overall separation of the acoustic and TBL contributions on the auto and cross-spectra. At medium frequencies, FA is efficient for the denoising of the acoustic autospectra and at high frequencies, the diagonal reconstruction methods from the literature are sufficient. In the very low frequency range, where the acoustic and TBL wavenumber contents overlap, the separation is still difficult to achieve.

Perspectives

Many perspectives for this work can be proposed. First, concerning numerical aspects for the resolution of the Bayesian inference problem, other samplers may be implemented with various benefits and limitations. For example, Variational Bayesian methods (Gelman et al., 2014, p. 331-338) can be employed to reduce the computation time, but this comes without guarantee of global convergence and requires more analytical development efforts. This may be useful to exploit very large data sets. For examples, during inflight tests, several engine and flight configurations may be recorded which provides a dataset that can be exploited globally such as in Dinsenmeyer et al. (2019), but for which the MCMC are computationally expensive.

Then, the versatility of the Bayesian framework makes it possible to extend the model to different needs. For application to flight test measurements, a spatial evolution of the TBL along the fuselage could be taken into account, as proposed in a model of Berton (2014), where the TBL parameters can vary locally. Other uncertainties can be integrated to the model, such as the angle of attack of the flow on the fuselage, which should improve the fitting of the TBL model. More advanced TBL models could also be implemented instead of the Corcos' one (Hwang et al., 2009; Graham, 1997), and the Bayesian framework offers different indicators for the selection of the most probable models (Ando, 2010). Moreover, in the field of aviation, it is frequent that numerical simulations of the TBL on the fuselage are available, so the possibility of using these simulation results as input for separation should be considered. Concerning source models, in the present study, only the random broadband acoustic sources have been taken into account, but other sources models could be implemented, such as cyclostationary sources for the study of tonal components of the aircraft engine noise.

Finally, many post-processing analyses of the separation results could be led. In general, a deep study of the effect of the separation methods on acoustic imaging maps should be conducted, in order to evaluate how the proposed separation can improve the localization, quantification or directivity of the imaged sources, as initiated in Dinsenmeyer et al. (2019). Acoustic imaging in space can be also an appropriate tool to validate the separation results when no baseline measurement is available. For example, in the case of the inflight measurements, the localized sources from the different contributions identified with FA-Corr can be analyzed to determine if they have any physical sense, in terms of location, directivity, frequency

content, etc. Once the separation approach is assessed, the components of the identified acoustic field can be physically analyzed to extract statistical properties of the sources, especially for applications on commercial aircraft engine jet noise whose noise generation mechanisms are still not fully understood.

A

Proceedings and publications

The following conference proceedings and article were produced as part of this thesis work:

Dinsenmeyer, A., **Antoni, J.**, **Leclère, Q.**, and **Pereira, A.** On the denoising of cross-spectral matrices for (aero) acoustic applications. In *7th Berlin beamforming conference*, 2018

Dinsenmeyer, A., **Leclère, Q.**, **Antoni, J.**, and **Julliard, E.** Comparison of microphone array denoising techniques and application to flight test measurements. In *25th AIAA/CEAS Aeroacoustics Conference*, page 2744, 2019

Sijtsma, P., **Dinsenmeyer, A.**, **Antoni, J.**, and **Leclère, Q.** Beamforming and other methods for denoising microphone array data. In *25th AIAA/CEAS Aeroacoustics Conference*, page 2653, 2019

Leclère, Q., **Dinsenmeyer, A.**, **Salze, E.**, and **Antoni, J.** A comparison between different wall pressure measurement devices for the separation and analysis of TBL and acoustic contributions. In *Flinovia-Flow Induced Noise and Vibration Issues and Aspects*. Springer, 2021. (In press)

Leclère, Q., **Aujogue, N.**, **Dinsenmeyer, A.**, **Antoni, J.**, and **Julliard, E.** Characterization of engine jet noise in flight conditions using advanced acoustic imaging methods. In *8th Berlin beamforming conference*, 2020

Dinsenmeyer, A., **Antoni, J.**, **Leclère, Q.**, and **Pereira, A.** A probabilistic approach for cross-spectral matrix denoising: Benchmarking with some recent methods. *The Journal of the Acoustical Society of America*, 147(5):3108–3123, 2020

B
Matrix properties

See Petersen and Pedersen (2008) for more matrix properties.

B.1 Derivatives

Let $\boldsymbol{a}$ and $\boldsymbol{b}$ be two complex vectors and $\boldsymbol{X}$, $\boldsymbol{A}$ and $\boldsymbol{B}$ be matrices.

$$\frac{\partial \boldsymbol{a}^H \boldsymbol{X} \boldsymbol{b}}{\partial \boldsymbol{X}} = \boldsymbol{a}\boldsymbol{b}^H \tag{B.1.1}$$

$$\frac{\partial \boldsymbol{a}^H \boldsymbol{X}^H \boldsymbol{b}}{\partial \boldsymbol{X}} = \boldsymbol{b}\boldsymbol{a}^H \tag{B.1.2}$$

$$\frac{\partial}{\partial \boldsymbol{X}} \operatorname{tr}(\boldsymbol{X}^H \boldsymbol{A} \boldsymbol{X} \boldsymbol{B}) = \boldsymbol{A}\boldsymbol{X}\boldsymbol{B} + \boldsymbol{A}^H \boldsymbol{X} \boldsymbol{B}^H \tag{B.1.3}$$

$$\frac{\partial}{\partial \boldsymbol{X}} \ln |\det(\boldsymbol{X})| = \boldsymbol{X}^{-H} \tag{B.1.4}$$

B.2 Kronecker product

$$\operatorname{vec}(\boldsymbol{A}\boldsymbol{X}\boldsymbol{B}) = (\boldsymbol{B}^H \otimes \boldsymbol{A}) \operatorname{vec}(X) \tag{B.2.1}$$

$$(\boldsymbol{A} \otimes \boldsymbol{B})^H = \boldsymbol{A}^H \otimes \boldsymbol{B}^H \tag{B.2.2}$$

$$(\boldsymbol{A} \otimes \boldsymbol{B})^* = \boldsymbol{A}^* \otimes \boldsymbol{B}^* \tag{B.2.3}$$

$$(\boldsymbol{A} \otimes \boldsymbol{B})(\boldsymbol{C} \otimes \boldsymbol{D}) = (\boldsymbol{A}\boldsymbol{C}) \otimes (\boldsymbol{B}\boldsymbol{D}) \tag{B.2.4}$$

C

Appendices of the Chapter 2

C.1 Marginalized likelihood

The marginalization is done by summing the joint Probability Density Function (PDF) $[\boldsymbol{y}_j, \boldsymbol{c}_j]$ over the values of $\boldsymbol{c}_j$:

$$\begin{aligned}[\boldsymbol{y}_j \mid \infty_{-\boldsymbol{c}_j}] &= \int [\boldsymbol{y}_j, \boldsymbol{c}_j] \, \mathrm{d}\boldsymbol{c}_j \\ &= \int [\boldsymbol{y}_j | \boldsymbol{c}_j][\boldsymbol{c}_j] \, \mathrm{d}\boldsymbol{c}_j\end{aligned}$$

Yet,

$$\begin{aligned}[\boldsymbol{y}_j \mid \boldsymbol{c}_j][\boldsymbol{c}_j] &\propto \mathrm{e}^{-(\boldsymbol{y}_j - \boldsymbol{L}\boldsymbol{c}_j)^H \lceil \boldsymbol{\sigma}_n^{-2} \rfloor (\boldsymbol{y}_j - \boldsymbol{L}\boldsymbol{c}_j)} \mathrm{e}^{\boldsymbol{c}^H \boldsymbol{c}_j} \\ &\propto \mathrm{e}^{-\boldsymbol{y}_j^H \lceil \boldsymbol{\sigma}_n^{-2} \rfloor \boldsymbol{y}_j} \, \mathrm{e}^{\underbrace{(\boldsymbol{L}\boldsymbol{c}_j)^H \lceil \boldsymbol{\sigma}_n^{-2} \rfloor \boldsymbol{y}_j}_{\boldsymbol{c}_j^H \boldsymbol{\Omega}_{\boldsymbol{c}_j}^{-1} \boldsymbol{\mu}_j}} \, \mathrm{e}^{\underbrace{\boldsymbol{y}_j^H \lceil \boldsymbol{\sigma}_n^{-2} \rfloor \boldsymbol{L}\boldsymbol{c}_j}_{\boldsymbol{\mu}_j^H \boldsymbol{\Omega}_{\boldsymbol{c}_j}^{-1} \boldsymbol{c}_j}} \, \mathrm{e}^{\underbrace{-\left(\boldsymbol{c}_j\right)^H (\boldsymbol{L}^H \lceil \boldsymbol{\sigma}_n^{-2} \rfloor \boldsymbol{L} + \boldsymbol{I}_\kappa) \boldsymbol{c}_j}_{-\boldsymbol{c}_j^H \boldsymbol{\Omega}_{\boldsymbol{c}_j}^{-1} \boldsymbol{c}_j}} \\ &\propto \boldsymbol{C}_1 \mathrm{e}^{-(\boldsymbol{c}_j - \boldsymbol{\mu}_{\boldsymbol{c}_j})^H \boldsymbol{\Omega}_{\boldsymbol{c}_j} (\boldsymbol{c}_j - \boldsymbol{\mu}_{\boldsymbol{c}_j})},\end{aligned}$$

$$\text{with } \boldsymbol{\Omega}_{\boldsymbol{c}_j} = \left(\boldsymbol{L}^H \lceil \boldsymbol{\sigma}_n^{-2} \rfloor \boldsymbol{L} + \boldsymbol{I}_\kappa\right)^{-1}, \tag{C.1.1}$$

$$\text{and } \boldsymbol{\mu}_{\boldsymbol{c}_j} = \boldsymbol{\Omega}_{\boldsymbol{c}_j} \boldsymbol{L}^H \lceil \boldsymbol{\sigma}_n^{-2} \rfloor \boldsymbol{y}_j. \tag{C.1.2}$$

And $\boldsymbol{C}_1$ can be identified as follows:

$$\begin{aligned}&\boldsymbol{C}_1 \, \mathrm{e}^{-\boldsymbol{\mu}_j^H \boldsymbol{\Omega}_{\boldsymbol{c}_j}^{-1} \boldsymbol{\mu}_j} \propto \mathrm{e}^{-\boldsymbol{y}_j^H \lceil \boldsymbol{\sigma}_n^{-2} \rfloor \boldsymbol{y}_j} \\ \Leftrightarrow \quad &\boldsymbol{C}_1 \propto \mathrm{e}^{-\boldsymbol{y}_j^H \lceil \boldsymbol{\sigma}_n^{-2} \rfloor \boldsymbol{y}_j} \, \mathrm{e}^{\boldsymbol{y}_j^H \overbrace{\lceil \boldsymbol{\sigma}_n^{-2} \rfloor \boldsymbol{L} \boldsymbol{\Omega}_{\boldsymbol{c}_j} \boldsymbol{L}^H \lceil \boldsymbol{\sigma}_n^{-2} \rfloor}^{\boldsymbol{A}} \boldsymbol{y}_j} \\ &\propto \mathrm{e}^{-\boldsymbol{y}_j^H \boldsymbol{B}^{-1} \boldsymbol{y}_j}.\end{aligned}$$

And as $\boldsymbol{A} = \lceil \boldsymbol{\sigma}_n^{-2} \rfloor \left(\boldsymbol{I} + \underbrace{(\boldsymbol{L}\boldsymbol{L}^H)^{-1}}_{\boldsymbol{A}_2^{-1}} \lceil \boldsymbol{\sigma}_n^2 \rfloor \right)^{-1}$, this gives

$$\begin{aligned}\boldsymbol{B}^{-1} &= -\boldsymbol{A} + \lceil \boldsymbol{\sigma}_n^{-2} \rfloor = \left(-\lceil \boldsymbol{\sigma}_n^{-2} \rfloor + \lceil \boldsymbol{\sigma}_n^{-2} \rfloor \left(\boldsymbol{I}_M + \boldsymbol{A}_2^{-1} \lceil \boldsymbol{\sigma}_n^2 \rfloor \right) \right) \left(\boldsymbol{I}_M + \boldsymbol{A}_2^{-1} \lceil \boldsymbol{\sigma}_n^2 \rfloor \right)^{-1} \\ &= \left(\boldsymbol{A}_2 + \lceil \boldsymbol{\sigma}_n^2 \rfloor \right)^{-1}.\end{aligned}$$

Finally, the marginal likelihood is

$$[\boldsymbol{y}_j \mid \infty_{-\boldsymbol{c}_j}] = \int [\boldsymbol{y}_j \mid \boldsymbol{c}_j][\boldsymbol{c}_j] \, \mathrm{d}\, \boldsymbol{c}_j \tag{C.1.3}$$

$$\propto \boldsymbol{C}_1 \underbrace{\int \mathcal{N}_c(\boldsymbol{\mu}_j, \boldsymbol{\Omega}_{\boldsymbol{c}_j}) \, \mathrm{d}\boldsymbol{c}_j}_{=1} \tag{C.1.4}$$

$$= \mathcal{N}_{\mathbb{C}}(\boldsymbol{0}, \boldsymbol{B}), \tag{C.1.5}$$

with $\boldsymbol{B} = \boldsymbol{L}\boldsymbol{L}^H + \lceil \boldsymbol{\sigma}_n^2 \rfloor$.

C.2 Sampling of the scale parameter s_k

Following the approach of Veit et al. (2008), as $\boldsymbol{c}_k$ and $\boldsymbol{L}_k$ are independent, the sampling distribution for the scale parameters $\boldsymbol{s}_k$ associated to each factor is given by

$$\begin{aligned}[\boldsymbol{s}_k \mid \infty] &\propto |\boldsymbol{s}_k|^{2(N_s-M-1)}[\boldsymbol{c}_k, \boldsymbol{L}_k \mid \boldsymbol{s}_k],\\ [\boldsymbol{s}_k \mid \infty] &\propto |\boldsymbol{s}_k|^{2(N_s-M-1)} \prod_{j=1}^{N_s}[\boldsymbol{c}_{kj}] \prod_{m=1}^{M}[\boldsymbol{L}_{mk}],\end{aligned} \tag{C.2.1}$$

with $|\boldsymbol{s}_k|^2 = \boldsymbol{s}_k\boldsymbol{s}_k^*$. Writing the change of variable $r_k = |\boldsymbol{s}_k|^2$, leads to

$$\begin{aligned}[r_k \mid \infty] &\propto r_k^{N_s-M-\frac{1}{2}-1}\mathrm{e}^{-r_k\sum_j \boldsymbol{c}_{kj}^H\gamma_k^{-2}\boldsymbol{c}_{kj}} \quad \mathrm{e}^{-r_k^{-1}\sum_m \boldsymbol{L}_{mk}^H\kappa\boldsymbol{L}_{mk}},\\ &\propto r_k^{N_s-M-\frac{1}{2}-1}\mathrm{e}^{-r_k\gamma_k^{-2}\boldsymbol{S}_{cc_{kk}}} \quad \mathrm{e}^{-r_k^{-1}\kappa\sum_m \boldsymbol{L}_{mk}^H\boldsymbol{L}_{mk}}.\end{aligned}$$

Then r_k follows a Generalized Inverse Gaussian (GIG) law such as:

$$f_{GIG}(r_k) = \left(\frac{a_{r_k}}{b_{r_k}}\right)^{\frac{p_r}{2}} \frac{r_k^{p_r-1}}{2\,\mathrm{Y}_{p_r}\left(\sqrt{a_{r_k}b_{r_k}}\right)}\mathrm{e}^{-\frac{1}{2}(a_{r_k}r_k+b_{r_k}r_k^{-1})} \quad , r_k > 0 \tag{C.2.2}$$

where $\mathrm{Y}_{p_r}(\cdot)$ is the Bessel fonction of the second kind. Identifying each term, gives

$$\begin{aligned}a_{r_k} &= 2\gamma_k^{-2}\boldsymbol{S}_{cc_{kk}},\\ b_{r_k} &= 2\kappa\sum_m \boldsymbol{L}_{mk}^H\boldsymbol{L}_{mk},\\ p_r &= N_s - M - \frac{1}{2}.\end{aligned}$$

Once r_k is sampled, we get

$$\boldsymbol{s}_k = \sqrt{r_k}\mathrm{e}^{j\phi} \quad \text{with} \quad \phi \sim \mathcal{U}(0, 2\pi). \tag{C.2.3}$$

The pseudo-code of the Gibbs sampler with the sampling of the scale parameter is given in Alg. 7, in which the lines added for the scaling are highlighted in gray.

C.2.1 Effect of the scaling

In order to illustrate the effect of the sampling of a scale parameter on the exploration of the posterior distribution by the Gibbs sampler, some numerical examples using the same toy case as given in Sec. 2.4.4 are studied. The data are fisrt simulated in presence of a low noise (SNR = 10 dB) and then for a higher noise (SNR = −10 dB).

Algorithm 7 FA solved with the Gibbs sampler, with the sampling of a scale parameter.

Initialization: $\boldsymbol{L}_0,\ \boldsymbol{\sigma}_{n_0}^2,\ \boldsymbol{\gamma}_0^2,\ \boldsymbol{q}_0$

Require: $\hat{\boldsymbol{S}}_{yy}, \kappa,\ \boldsymbol{a}_\gamma,\ \boldsymbol{b}_\gamma,\ \boldsymbol{a}_n,\ \boldsymbol{b}_n,\ a_l, b_l,\ N_{\text{run}}$

for $i = 1, \ldots, N_{\text{run}}$ **do**

Sample $\boldsymbol{S}_{cc_i}$ following Eq. (2.4.15)

Sample $\boldsymbol{L}_i$ in Eq. (2.4.17)

Sample $\boldsymbol{s}_i$ in Eq. (C.2.3)

Scale $\boldsymbol{S}_{cc_i}$ and $\boldsymbol{L}_i$ doing $\boldsymbol{L}_k := \frac{\boldsymbol{L}_k}{\boldsymbol{s}_k}$ and $\boldsymbol{c}_k := \boldsymbol{c}_k \boldsymbol{s}_k$

Sample $\boldsymbol{\gamma}_i^2$ in Eq. (2.4.20)

Update $\boldsymbol{\Omega}_c$ using the new $\boldsymbol{L}$ and $\boldsymbol{S}_{cc}$

Resample $\boldsymbol{W}_c$ using the new $\boldsymbol{\Omega}_c$

Sample l_i in Eq. (2.4.26)

Sample $\boldsymbol{q}_i$ in Eq. (2.4.25)

Sample $\boldsymbol{\sigma}_{n_i}^2$ in Eq. (2.4.21)

end for

return Posterior PDFs of $\boldsymbol{S}_{cc},\ \boldsymbol{L},\ \boldsymbol{\sigma}_n^2,\ \boldsymbol{\gamma}^2,\ \boldsymbol{q}$

C.2.1.1 For an SNR of 10 dB

In order to evaluate the effect of the scaling, the chains for the absolute value of the weighted factors $|\boldsymbol{q}_k \boldsymbol{c}_k|$ as well as the ℓ_2-norm of the vector of the mixing matrix $\|\boldsymbol{L}_k\|_2$ are plotted in Fig. C.1. On this figure, the weight are sampled in the posterior marginalized with respect to the factors.

As the model perfectly fits the data, the two approaches (with and without scaling) provide the same denoising error. However, the scaling induces a larger variance of the factors, and thus a better mixing of the chains, which is prompt to produce a more efficient exploration of the posterior distribution.

The numerical case being favorable, the convergence is quickly reached (*i.e* the chain of product $\boldsymbol{L}\lceil \boldsymbol{q} \rfloor \boldsymbol{c}$ is quickly stationary. However, looking only at the chains of Fig. C.1, the diagnosis of convergence is easier to do on the scaled parameters, for which the chains are more clearly stabilized. These results are in accordance with those of Veit et al. (2008).

C.2.1.2 For an SNR of -10 dB

The evolution of the factors and their associated number of non-null weights are provided in Fig. C.2, based on the numerical experiment performs with an Signal-to-Noise Ratio (SNR) of -10 dB. These results can thus be compared with the Fig. 2.7, obtained in the same configuration, but without scaling.

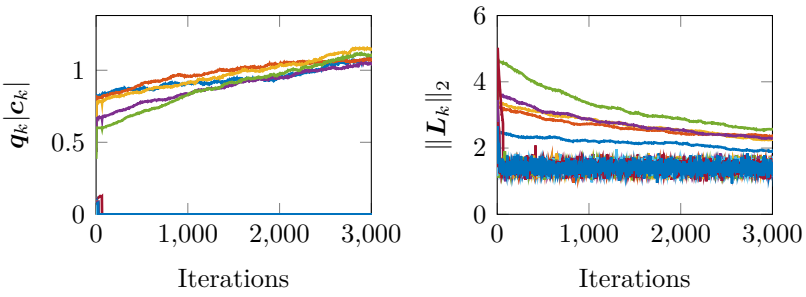

(a) No scaling

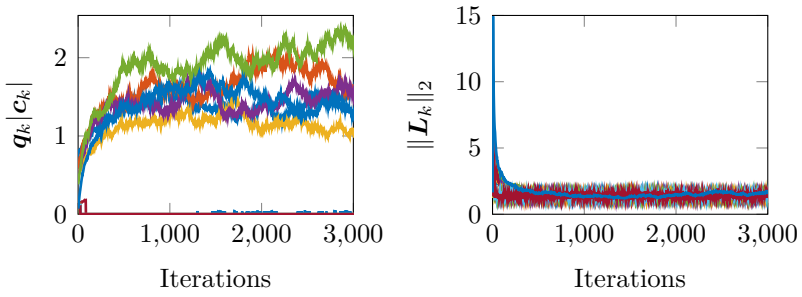

(b) With scaling

Figure C.1: Evolution of the factors and mixing matrix from the marginalized Gibbs sampler, without (top) and with (bottom) the scaling strategy.

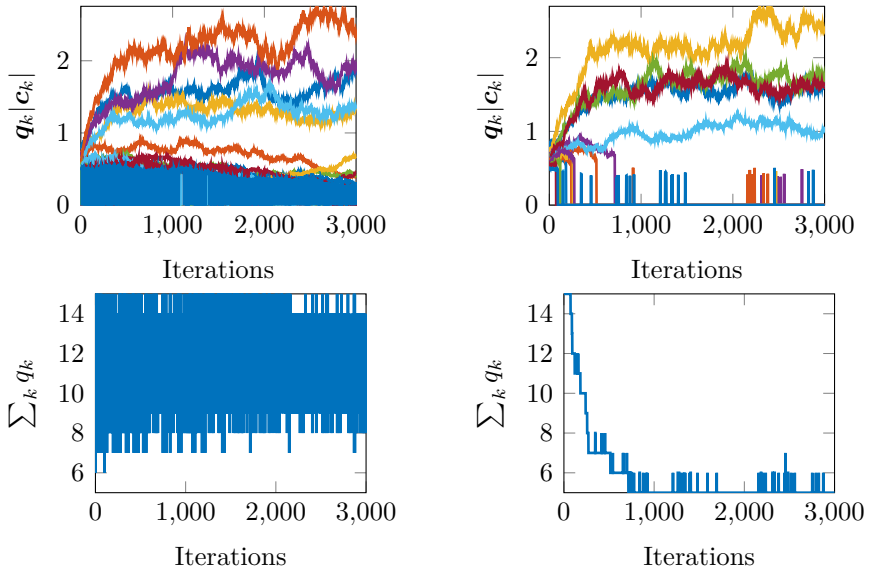

(a) With scaling, no marginalization **(b)** With scaling, with marginalization

Figure C.2: Evolution of the factors and their weights, from the non-marginalized (left) and marginalized (right) Gibbs sampler, with the scaling strategy.

At a high level of noise, the effect of the scaling is less visible. Compared to the Fig. 2.7, the chains with scaling given in Fig. C.2 rapidly stop increasing. However,

as the noise level is high, the chains are well mixed, due to the high variance of the likelihood. In this case, the effect of the scaling becomes less significant.

D

Appendices of the Chapter 3

D.1 Posteriors for the Gibbs sampler

In this section are given the expressions of the posterior distributions required for the implementation of the CSM-based Gibbs sampler, to solve the separation problem based on a correlated noise model.

Sampling of $\boldsymbol{c}$

Using the expression of the likelihood in Eq. (3.2.16) and the Gaussian prior on $\boldsymbol{c}$ (Eq. (3.2.5)) leads to:

$$[\boldsymbol{c}_j \mid \infty] \propto [\boldsymbol{c}_j][\boldsymbol{y}_j \mid \infty], \tag{D.1.1}$$

$$\propto \mathcal{N}_{\mathbb{C}}(\boldsymbol{\mu}_{c_j}, \boldsymbol{\Omega}_c), \tag{D.1.2}$$

$$\text{with } \boldsymbol{\mu}_{c_j} = \underbrace{\boldsymbol{\Omega}_c \lceil \boldsymbol{q} \rfloor \boldsymbol{L}^H \lceil \boldsymbol{\sigma}_\epsilon^{-2} \rfloor}_{\boldsymbol{T}_c^H} (\boldsymbol{y}_j - p\boldsymbol{\nu}_j), \tag{D.1.3}$$

$$\text{and } \boldsymbol{\Omega}_c = \left(\lceil \boldsymbol{q} \rfloor \boldsymbol{L}^H \lceil \boldsymbol{\sigma}_\epsilon^{-2} \rfloor \boldsymbol{L} \lceil \boldsymbol{q} \rfloor + \lceil \boldsymbol{\gamma}^{-2} \rfloor \right)^{-1}. \tag{D.1.4}$$

For the implementation of the quadratic Gibbs sampler, the same approach as in Sec. 2.4.2.1 is followed:

$$\boldsymbol{S}_{cc} \mid \infty \approx \mathbb{E}\{\boldsymbol{\mu}_{c_j} \boldsymbol{\mu}_{c_j}^H\} + \frac{1}{N_s} \boldsymbol{W}_c \tag{D.1.5}$$

$$= \boldsymbol{T}_c^H \left(\boldsymbol{S}_{yy} + p\boldsymbol{S}_{\nu\nu} p^H - p\boldsymbol{S}_{\nu y} - \boldsymbol{S}_{y\nu} p^H \right) \boldsymbol{T}_c + \frac{1}{N_s} \boldsymbol{W}_c, \tag{D.1.6}$$

where $\boldsymbol{W}_c$ is a random matrix that follows a complex Wishart distribution, with N_s degrees of freedom and variance matrix $\boldsymbol{\Omega}_c$. The expression of the CSMs $\boldsymbol{S}_{\nu y}$ and $\boldsymbol{S}_{y\nu}$ are given later in Eq. (D.1.27).

Sampling of $\boldsymbol{\nu}$

Similarly, from the Gaussian prior assigned to $\boldsymbol{\nu}$ in Eq. (3.2.15),

$$[\boldsymbol{\nu}_j \mid \infty] \propto [\boldsymbol{\nu}_j][\boldsymbol{y}_j \mid \infty], \tag{D.1.7}$$

$$\propto \mathcal{N}_{\mathbb{C}}(\boldsymbol{\mu}_{\nu_j}, \boldsymbol{\Omega}_\nu), \tag{D.1.8}$$

$$\text{with } \boldsymbol{\mu}_{\nu_j} = \underbrace{\boldsymbol{\Omega}_\nu p^H \lceil \boldsymbol{\sigma}_\epsilon \rfloor^{-2}}_{\boldsymbol{T}_\nu^H} (\boldsymbol{y}_j - \boldsymbol{L}\lceil \boldsymbol{q} \rfloor \boldsymbol{c}_j)\,, \tag{D.1.9}$$

$$\text{and } \boldsymbol{\Omega}_\nu = \left(p^H \lceil \boldsymbol{\sigma}_\epsilon^{-2} \rfloor p + \boldsymbol{\Sigma}_\nu(\boldsymbol{\theta})^{-2} \right)^{-1}. \tag{D.1.10}$$

For the CSM-based Gibbs sampler:

$$\boldsymbol{S}_{\nu\nu} \mid \infty \approx \mathbb{E}\{\boldsymbol{\mu}_{\nu_j} \boldsymbol{\mu}_{\nu_j}^H\} + \frac{1}{N_s} \boldsymbol{W}_\nu \tag{D.1.11}$$

$$= \boldsymbol{T}_\nu^H \left(\boldsymbol{S}_{yy} + \boldsymbol{L}\lceil \boldsymbol{q} \rfloor \boldsymbol{S}_{cc} \lceil \boldsymbol{q} \rfloor \boldsymbol{L}^H - \boldsymbol{L}\lceil \boldsymbol{q} \rfloor \boldsymbol{S}_{cy} - \boldsymbol{S}_{yc} \lceil \boldsymbol{q} \rfloor \boldsymbol{L}^H \right) \boldsymbol{T}_\nu + \frac{1}{N_s} \boldsymbol{W}_\nu, \tag{D.1.12}$$

where $\boldsymbol{W}_\nu$ follows a complex Wishart distribution, with N_s degrees of freedom and variance matrix $\boldsymbol{\Omega}_\nu$. The expression of the CSMs $\boldsymbol{S}_{cy}$ and $\boldsymbol{S}_{yc}$ are given later in Eq. (D.1.25)

Sampling of $\boldsymbol{L}$

From the prior on $\boldsymbol{L}$ given in Eq. (3.2.4), the posterior is calculated as follows:

$$[\boldsymbol{\lambda} \mid \infty] \propto [\boldsymbol{\lambda}] \prod_{j=1}^{N_s} [\boldsymbol{y}_j \mid \infty], \tag{D.1.13}$$

$$\propto \mathcal{N}_{\mathbb{C}}(\boldsymbol{\mu}_\lambda, \boldsymbol{\Omega}_\lambda), \tag{D.1.14}$$

$$\text{with } \boldsymbol{\Omega}_\lambda = \left(\sum_j (\boldsymbol{c}_j^T \lceil \boldsymbol{q} \rfloor \otimes \boldsymbol{I}_M)^H \lceil \boldsymbol{\sigma}_\epsilon^{-2} \rfloor (\boldsymbol{c}_j^T \lceil \boldsymbol{q} \rfloor \otimes \boldsymbol{I}_M) + \kappa \boldsymbol{I}_{M\kappa} \right)^{-1} \tag{D.1.15}$$

$$= \left((\lceil \boldsymbol{q} \rfloor \boldsymbol{S}_{cc}^* \lceil \boldsymbol{q} \rfloor) \otimes \lceil \boldsymbol{\sigma}_\epsilon^{-2} \rfloor + \kappa \boldsymbol{I}_{M\kappa} \right)^{-1}, \tag{D.1.16}$$

$$\text{and } \boldsymbol{\mu}_\lambda = \boldsymbol{\Omega}_\lambda \sum_j \left(\boldsymbol{c}_j^T \lceil \boldsymbol{q} \rfloor \otimes \boldsymbol{I}_M \right)^H \lceil \boldsymbol{\sigma}_\epsilon^{-2} \rfloor (\boldsymbol{y}_j - p\boldsymbol{\nu}_j) \tag{D.1.17}$$

$$= \boldsymbol{\Omega}_\lambda \operatorname{vec}\left(\lceil \boldsymbol{\sigma}_\epsilon^{-2} \rfloor (\boldsymbol{y}_j - p\boldsymbol{\nu}_j) \boldsymbol{c}_j^H \lceil \boldsymbol{q} \rfloor \right) \tag{D.1.18}$$

$$= \boldsymbol{\Omega}_\lambda \operatorname{vec}\left(\lceil \boldsymbol{\sigma}_\epsilon^{-2} \rfloor \left(\boldsymbol{S}_{yc} \lceil \boldsymbol{q} \rfloor - p \boldsymbol{S}_{\nu c} \lceil \boldsymbol{q} \rfloor \right) \right). \tag{D.1.19}$$

The expression of the CSMs $\boldsymbol{S}_{yc}$ and $\boldsymbol{S}_{\nu c}$ is given later in Eqs. (D.1.25) and (D.1.29) respectively.

Sampling of p

The complexe scalar parameter p is assigned a Gaussian prior (Eq. (3.2.12)), which gives the following posterior:

$$[p \mid \infty] \propto [p] \prod_j [\boldsymbol{y}_j \mid \infty], \tag{D.1.20}$$

$$\propto \mathcal{N}_{\mathbb{C}}(\mu_p, \Omega_p), \tag{D.1.21}$$

$$\text{with } \Omega_p = \left(\text{tr}\left(\boldsymbol{\sigma}_\epsilon^{-2} \boldsymbol{S}_{\nu\nu}\right) + \sigma_p^{-2}\right)^{-1}, \tag{D.1.22}$$

$$\text{and } \mu_p = \Omega_p \left(\text{tr}\left(\boldsymbol{\sigma}_\epsilon^{-2} (\boldsymbol{S}_{y\nu} - \boldsymbol{L}\lceil \boldsymbol{q} \rfloor \boldsymbol{S}_{c\nu})\right) + \sigma_p^{-2} a_p\right). \tag{D.1.23}$$

The expression of the CSMs $\boldsymbol{S}_{y\nu}$ and $\boldsymbol{S}_{c\nu}$ is given later in Eqs. (D.1.27) and (D.1.29) respectively.

Expression of the cross-correlation matrices

The previous calculations require the expression of some cross-correlations, which are detailed in the present section. The same approach as in Sec. 2.4.2 is followed, for the implementation of the CSM-based Gibbs sampler.

Starting from,

$$\boldsymbol{S}_{yc} = \sum_{j=1}^{N_s} \boldsymbol{y}_j \boldsymbol{c}_j^H, \tag{D.1.24}$$

and replacing $\boldsymbol{c}_j$ by its posterior mean value (given in Eq. (D.1.3)) leads to

$$\boldsymbol{S}_{yc} = (\boldsymbol{S}_{yy} - \boldsymbol{S}_{y\nu})\, \boldsymbol{T}_c = \boldsymbol{S}_{cy}^H. \tag{D.1.25}$$

Similarly,

$$\boldsymbol{S}_{y\nu} = \sum_{j=1}^{N_s} \boldsymbol{y}_j \boldsymbol{\nu}_j^H, \tag{D.1.26}$$

and replacing $\boldsymbol{\nu}$ by its posterior mean value (given in Eq. (D.1.9)) leads to

$$\boldsymbol{S}_{y\nu} = (\boldsymbol{S}_{yy} - \boldsymbol{S}_{yc}\lceil \boldsymbol{q} \rfloor \boldsymbol{L}^H)\, \boldsymbol{T}_\nu = \boldsymbol{S}_{\nu y}^H. \tag{D.1.27}$$

Again the calculations for $\boldsymbol{S}_{c\nu}$ starts from,

$$\boldsymbol{S}_{c\nu} = \sum_{j=1}^{N_s} \boldsymbol{c}_j \boldsymbol{\nu}_j^H, \tag{D.1.28}$$

and at this step, either ν or $\boldsymbol{c}$ can be replaced by its mean posterior. Choosing arbitrarily to replace $\boldsymbol{\nu}$ leads to

$$\boldsymbol{S}_{c\nu} = (\boldsymbol{S}_{cy} - \boldsymbol{S}_{cc}\lceil \boldsymbol{q} \rfloor \boldsymbol{L}^H)\, \boldsymbol{T}_\nu = \boldsymbol{S}_{\nu c}^H. \tag{D.1.29}$$

As all these cross-correlations are inter-dependent, they have to be properly updated during the Gibbs sampler, and some of them have to be initialized. An example of initialization is given in Sec. 3.4.1.

Sampling of $\boldsymbol{\sigma}_\epsilon^2$

The posterior expression of the additive noise is very similar to the one from the uncorrelated noise model, although a little longer:

$$[\boldsymbol{\sigma}_{\epsilon_m}^2 \mid \infty] \propto [\boldsymbol{\sigma}_\epsilon^2] \prod_j [\boldsymbol{y}_j \mid \infty], \tag{D.1.30}$$

$$\propto \mathcal{IG}(\boldsymbol{a}_\epsilon, \boldsymbol{b}_\epsilon) \prod_{j=1}^{N_s} \mathcal{N}_{\mathbb{C}} \left(\boldsymbol{L}\lceil \boldsymbol{q} \rfloor \boldsymbol{c}_j + p\boldsymbol{\nu}_j, \lceil \boldsymbol{\sigma}_\epsilon^2 \rfloor \right), \tag{D.1.31}$$

$$\propto \mathcal{IG}(\boldsymbol{a}_\epsilon + I_s, \boldsymbol{b}_\epsilon + \boldsymbol{T}_{2_{mm}}), \tag{D.1.32}$$

with

$$\boldsymbol{T}_2 = \sum_j (\boldsymbol{y}_j - \boldsymbol{L}\lceil \boldsymbol{q} \rfloor \boldsymbol{c}_j - p\boldsymbol{\nu}_j)\, (\boldsymbol{y}_j - \boldsymbol{L}\lceil \boldsymbol{q} \rfloor \boldsymbol{c}_j - p\boldsymbol{\nu}_j)^H \tag{D.1.33}$$

$$\begin{aligned} =& \boldsymbol{S}_{yy} + \boldsymbol{L}\lceil \boldsymbol{q} \rfloor \boldsymbol{S}_{cc} \lceil \boldsymbol{q} \rfloor \boldsymbol{L}^H + p\boldsymbol{S}_{\nu\nu} p^H - \boldsymbol{S}_{yc}\lceil \boldsymbol{q} \rfloor \boldsymbol{L}^H - \boldsymbol{L}\lceil \boldsymbol{q} \rfloor \boldsymbol{S}_{cy} \\ & - \boldsymbol{S}_{y\nu} p^H - p\boldsymbol{S}_{\nu y} + \boldsymbol{L}\lceil \boldsymbol{q} \rfloor \boldsymbol{S}_{c\nu} p^H + p\boldsymbol{S}_{\nu c} \lceil \boldsymbol{q} \rfloor \boldsymbol{L}^H. \end{aligned} \tag{D.1.34}$$

However, due to the iterative process, this expression can be slightly negative, which can lead to a negative parametrization of the inverse-gamma. Therefore, an alternative expression is proposed, replacing $\boldsymbol{c}_j$ by $\boldsymbol{c}_j \mid \infty = \boldsymbol{\mu}_{c_j} + \boldsymbol{x}_j$ with $[\boldsymbol{x}_j] = \mathcal{N}_{\mathbb{C}}(\boldsymbol{0}, \boldsymbol{\Omega}_c)$ in Eq. (D.1.33):

$$\begin{aligned} \boldsymbol{T}_2 \approx & \sum_j (\boldsymbol{y}_j - p\boldsymbol{\nu}_j - \boldsymbol{L}\lceil \boldsymbol{q} \rfloor \boldsymbol{T}_c^H (\boldsymbol{y}_j - p\boldsymbol{\nu}_j))\, (\boldsymbol{y}_j - p\boldsymbol{\nu}_j - \boldsymbol{L}\lceil \boldsymbol{q} \rfloor \boldsymbol{T}_c^H (\boldsymbol{y}_j - p\boldsymbol{\nu}_j))^H \\ & + \boldsymbol{L}\lceil \boldsymbol{q} \rfloor \boldsymbol{W}_c \lceil \boldsymbol{q} \rfloor \boldsymbol{L}^H \end{aligned} \tag{D.1.35}$$

$$\begin{aligned} =& (\boldsymbol{I}_M - \boldsymbol{L}\lceil \boldsymbol{q} \rfloor \boldsymbol{T}_c^H)(\boldsymbol{S}_{yy} + p\boldsymbol{S}_{\nu\nu} p^H - \boldsymbol{S}_{y\nu} p^H - p\boldsymbol{S}_{\nu y})(\boldsymbol{I}_M - \boldsymbol{T}_c \lceil \boldsymbol{q} \rfloor \boldsymbol{L}^H) \\ & + \boldsymbol{L}\lceil \boldsymbol{q} \rfloor \boldsymbol{W}_c \lceil \boldsymbol{q} \rfloor \boldsymbol{L}^H. \end{aligned} \tag{D.1.36}$$

Sampling of l and $\boldsymbol{\gamma}^2$

The sampling posterior of $\boldsymbol{\gamma}^2$ and l are the same as the one from the previous chapter, see Sec. 2.4.2.1.

Sampling of $\boldsymbol{q}$

The sampling of $\boldsymbol{q}$ is the same as from the previous chapter.

Without marginalization

According to the Beta prior assigned to $\boldsymbol{q}$ (see Eq. (3.2.6)), the posterior is given by

$$[\boldsymbol{q}_k|\infty] \propto [\boldsymbol{q}_k] \prod_j [\boldsymbol{y}_j|\boldsymbol{q}_k, \infty], \tag{D.1.37}$$

$$\propto \mathrm{e}^{-\operatorname{tr}\left(\lceil \boldsymbol{\sigma}_\epsilon^{-2} \rfloor \boldsymbol{T}_2(\boldsymbol{q}_k)\right) - \boldsymbol{q}_k \ln\left(\frac{1}{l}-1\right)}, \tag{D.1.38}$$

$$\propto \mathrm{e}^{-g(\boldsymbol{q}_k)}. \tag{D.1.39}$$

with $\boldsymbol{T}_2$ given in Eq. (D.1.36).

With marginalization with respect to $\boldsymbol{c}$

The calculation of the posterior distribution of $\boldsymbol{q}$ marginalized with respect to $\boldsymbol{c}$ requires the expression of the marginal likelihood, given by:

$$[\boldsymbol{y}_j \mid \infty_{-\boldsymbol{c}_j}] = \int [\boldsymbol{y}_j|\boldsymbol{c}_j][\boldsymbol{c}_j] \, \mathrm{d}\boldsymbol{c}_j \tag{D.1.40}$$

Yet, by doing similar calculation as in appendix C.1,

$$\begin{aligned}[\boldsymbol{y}_j \mid \boldsymbol{c}_j][\boldsymbol{c}_j] &\propto \mathrm{e}^{-(\boldsymbol{y}_j - \boldsymbol{L}\boldsymbol{c}_j - p\boldsymbol{\nu}_j)^H \lceil \boldsymbol{\sigma}_n^{-2} \rfloor (\boldsymbol{y}_j - \boldsymbol{L}\boldsymbol{c}_j - p\boldsymbol{\nu}_j)} \mathrm{e}^{\boldsymbol{c}^H \lceil \boldsymbol{\gamma}^2 \rfloor \boldsymbol{c}_j} \\ &\propto \boldsymbol{C}_2 \mathrm{e}^{-(\boldsymbol{c}_j - \boldsymbol{\mu}_j)^H \boldsymbol{\Omega}_{\boldsymbol{c}_j} (\boldsymbol{c}_j - \boldsymbol{\mu}_j)},\end{aligned}$$

$$\text{with} \quad \boldsymbol{C}_2 \propto \mathcal{N}_{\mathbb{C}}(p\boldsymbol{\nu}_j, \boldsymbol{B}_2), \tag{D.1.41}$$

$$\text{and} \quad \boldsymbol{B}_2 = \boldsymbol{L}\lceil \boldsymbol{\gamma}^2 \rfloor \boldsymbol{L}^H + \lceil \boldsymbol{\sigma}_\epsilon^{-2} \rfloor. \tag{D.1.42}$$

Therefore, the marginalized likelihood is

$$[\boldsymbol{y}_j \mid \infty_{-\boldsymbol{c}_j}] = \mathcal{N}_{\mathbb{C}}(p\boldsymbol{\nu}_j, \boldsymbol{B}_2). \tag{D.1.43}$$

Then, the posterior distribution of $\boldsymbol{q}$ marginalized with respect to $\boldsymbol{c}$ is

$$[\boldsymbol{q}_k|\infty_{-\boldsymbol{c}}] \propto [\boldsymbol{q}_k] \prod_j [\boldsymbol{y}_j|\infty_{-\boldsymbol{c}}], \tag{D.1.44}$$

$$\propto \mathrm{e}^{-\operatorname{tr}\left(\boldsymbol{B}_2(\boldsymbol{q}_k)^{-1}(\boldsymbol{S}_{yy}-p\boldsymbol{S}_{\nu y}-\boldsymbol{S}_{y\nu}p^H+p\boldsymbol{S}_{\nu\nu}p^H)\right)-N_s \ln|\boldsymbol{B}_2(\boldsymbol{q}_k)|-\boldsymbol{q}_k \ln\left(\frac{1}{l}-1\right)}, \tag{D.1.45}$$

$$\propto \mathrm{e}^{g_2(\boldsymbol{q}_k)}. \tag{D.1.46}$$

Then, the probability of state change for each binary is evaluated the same way as in Sec. 2.4.3.

D.2 Complementary figures for the numerical validations

D.2.1 Effect of the number of sensors on the chain convergence

In order to evaluate the effect of the number of sensors on the convergence of the sampler, the chains of the mean additive noise for different numbers of sensors are plotted in Fig. D.1. The mean of the additive noise $\boldsymbol{\sigma}_\epsilon^2$ is representative of the variance of the likelihood and thus gives an idea of the global convergence of the Gibbs sampler.

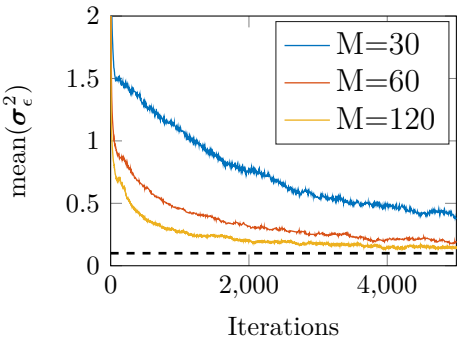

Figure D.1: Chains of the mean additive noise for different numbers M of sensors. The dashed line indicate the target value.

D.2.2 Effect of the frequency on the chain convergence

The convergence speed of each parameter can differ from one to another depending on the data to fit. To illustrate this fact, the data set is simulated at a frequency four times higher than the original one, that is 152 Hz instead of 38 Hz. This induces a correlation length four times smaller than the original one, that is $L_{c_x} = 0.5\overline{\boldsymbol{\delta x}}$. The chains for different parameters of the model are given in Fig. D.2, which shows that the TBL parameters converge slower than for the simulation at lower frequency.

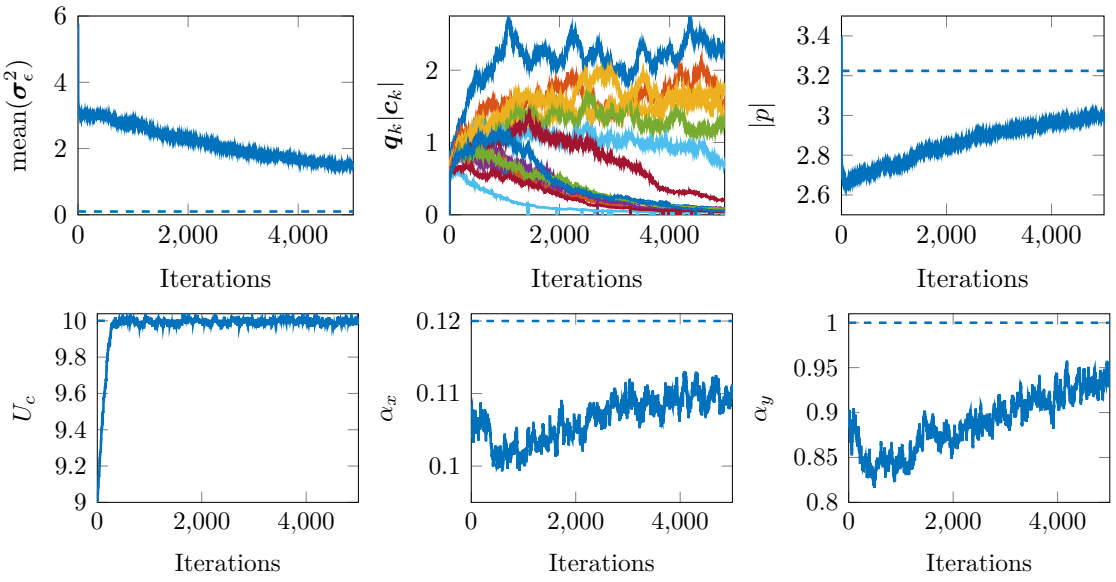

Figure D.2: Chains of several inferred parameters, from FA-Corr applied at a frequency of 152 Hz, which is four times higher than the original simulation. The Corcos parameters are sampled and the dashed lines indicate the target values.

E

Appendix for the chapter 4

E.1 Inflight measurements – Eigenvalues of the acoustic part

The five highest eigenvalues are plotted in Fig. E.1 as a function of the frequency for three CSMs:

- the raw measurements in cruise configuration,
- the acoustic part identified by the FA approach,
- the acoustic part identified by the FA-Corr approach.

For the three CSMs, the number of significant eigenvalues (defined as higher than 1% of the greatest eigenvalue) is also plotted in Fig. E.2.

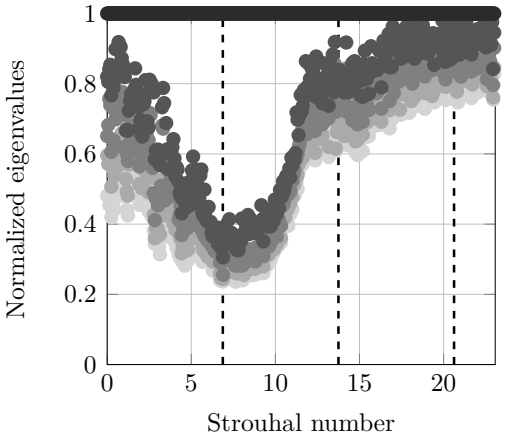

(a) Measurements (AT)

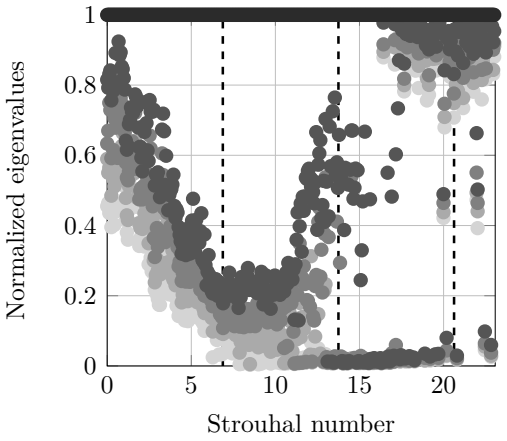

(b) Identified with FA-MCMC

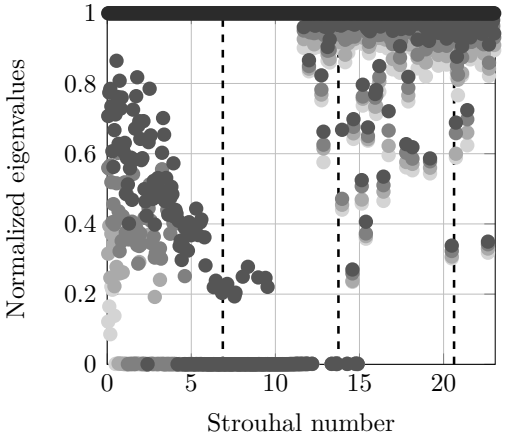

(c) Identified with FA-Corr

Figure E.1: Five highest normalized eigenvalues of the acoustic CSM for each frequency. Vertical lines (**- - -**) indicate the blade passing frequencies.

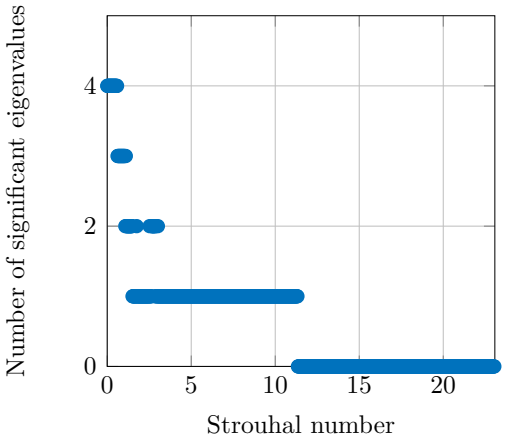

(a) Measurements (AT)

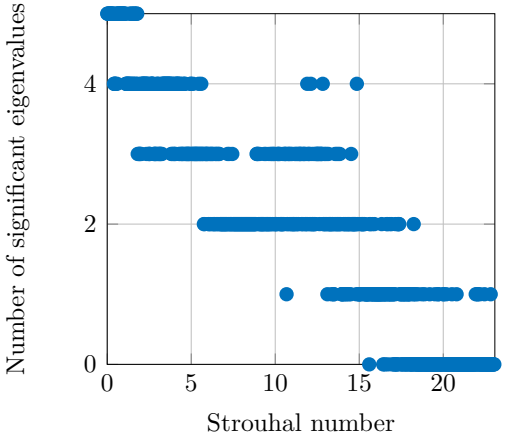

(b) Identified with FA-MCMC

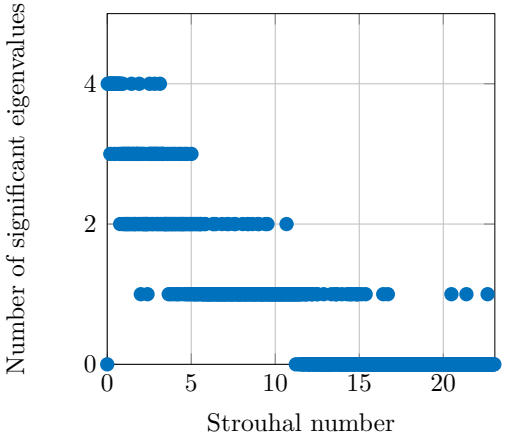

(c) Identified with FA-Corr

Figure E.2: Number of significant eigenvalues the acoustic CSM at each frequency.

Bibliography

Abraham, B. M. and **Keith, W. L.** Direct measurements of turbulent boundary layer wall pressure wavenumber-frequency spectra. *Journal of Fluids Engineering*, 120:29–39, March 1998.

Ahrendt, P. The multivariate gaussian probabilitydistribution. Technical report, IMM, Technical University of Denmark, 2005.

Akaike, H. A new look at the statistical model identification. *IEEE transactions on automatic control*, 19(6):716–723, 1974.

Allen, C. and **Soderman, P.** Aeroacoustic probe design for microphone to reduce flow-induced self-noise. In *15th Aeroacoustics Conference*, page 4343, 1993.

Amailland, S. *Caractérisation de sources acoustiques par imagerie en écoulement d'eau confiné*. PhD thesis, Le Mans Université, 2017.

Amailland, S., **Thomas, J.-H.**, **Pézerat, C.**, and **Boucheron, R.** Boundary layer noise subtraction in hydrodynamic tunnel using robust principal component analysis. *The Journal of the Acoustical Society of America*, 143(4):2152–2163, 2018.

Ando, T. *Bayesian Model Selection and Statistical Modeling*. CRC Press, 2010.

Antoni, J. and **Schoukens, J.** Optimal settings for measuring frequency response functions with weighted overlapped segment averaging. *IEEE transactions on instrumentation and measurement*, 58(9):3276–3287, 2009.

Antoni, J., **Vanwynsberghe, C.**, **Le Magueresse, T.**, **Bouley, S.**, and **Gilquin, L.** Mapping uncertainties involved in sound source reconstruction with a cross-spectral-matrix-based Gibbs sampler. *The Journal of the Acoustical Society of America*, 146(6):4947–4961, 2019.

Arguillat, B., **Ricot, D.**, **Bailly, C.**, and **Robert, G.** Measured wavenumber: Frequency spectrum associated with acoustic and aerodynamic wall pressure fluctuations. *The Journal of the Acoustical Society of America*, 128(4):1647–1655, 2010.

Bahr, C. J. and **Horne, W. C.** Subspace-based background subtraction applied to aeroacoustic wind tunnel testing. *International Journal of Aeroacoustics*, 16 (4-5):299–325, 2017.

Bartholomew, D. J., **Knott, M.**, and **Moustaki, I.** *Latent variable models and factor analysis: A unified approach*, volume 904. John Wiley & Sons, 2011.

Behrens, R. T. and **Scharf, L. L.** Signal processing applications of oblique projection operators. *IEEE Transactions on Signal Processing*, 42(6):1413–1424, 1994.

Bendat, J. and **Piersol, A.** *Engineering applications of correlation and spectral analysis*. Wiley-Interscience, New York, 1980.

Berouti, M., **Schwartz, R.**, and **Makhoul, J.** Enhancement of speech corrupted by acoustic noise. In *ICASSP'79. IEEE International Conference on Acoustics, Speech, and Signal Processing*, volume 4, pages 208–211. IEEE, 1979.

Berton, M. *Modélisation de la réponse vibro-acoustique d'une structure excitée par une couche limite turbulente en présence d'un gradient de pression statique*. PhD thesis, 2014.

Bishop, C. M. Bayesian PCA. In *Advances in neural information processing systems*, pages 382–388, 1999.

Bishop, C. M. *Pattern recognition and machine learning*. Springer, 2006.

Blacodon, D. and **Bulté, J.** Reverberation cancellation in a closed test section of a wind tunnel using a multi-microphone cesptral method. *Journal of Sound and Vibration*, 333(9):2669–2687, 2014.

Blake, W. K. and **Chase, D. M.** Wavenumber-frequency spectra of turbulent boundary layer pressure measured by microphone arrays. *The Journal of the Acoustical Society of America*, 47(1A):92–92, 1970.

Boll, S. Suppression of acoustic noise in speech using spectral subtraction. *IEEE Transactions on Acoustics, Speech, and Signal Processing*, 27(2):113–120, Apr 1979.

Bouveyron, C., **Latouche, P.**, and **Mattei, P.-A.** Exact dimensionality selection for bayesian pca. *Scandinavian Journal of Statistics*, 47(1):196–211, 2019.

Bouwmans, T., **Aybat, N. S.**, and **Zahzah, E.-h.** *Handbook of robust low-rank and sparse matrix decomposition: Applications in image and video processing*. Chapman and Hall/CRC, 2016.

Brooks, S., **Gelman, A.**, **Jones, G. L.**, and **Meng, X.-L.** *Handbook of Markov Chain Monte Carlo*. 2011.

Brooks, T. and **Humphreys, Jr, W.** Effect of directional array size on the measurement of airframe noise components. In *5th AIAA/CEAS Aeroacoustics Conference and Exhibit*, page 1958, 1999.

Brown, D. A., **McMahan, C. S.**, and **Watson Self, S.** Sampling strategies for fast updating of gaussian markov random fields. *The American Statistician*, pages 1–24, 2019.

Bull, M. Wall-pressure fluctuations beneath turbulent boundary layers: some reflections on forty years of research. *Journal of Sound and vibration*, 190(3): 299–315, 1996.

Bulté, J. Acoustic array measurements in aerodynamic wind tunnels: a subspace approach for noise suppression. In *13th AIAA/CEAS aeroacoustics conference, Rome, Italy*, pages 21–23, 2007.

Candès, E. J., **Li, X.**, **Ma, Y.**, and **Wright, J.** Robust principal component analysis? *J. ACM*, 58(3):11:1–11:37, June 2011.

Capon, J. High-resolution frequency-wavenumber spectrum analysis. *Proceedings of the IEEE*, 57(8): p. 1408–1418, 1969.

Champagnat, F., **Goussard, Y.**, and **Idier, J.** Unsupervised deconvolution of sparse spike trains using stochastic approximation. *IEEE Transactions on Signal Processing*, 44(12):2988–2998, 1996.

Chase, D. M. Modeling the wavevector-frequency spectrum of turbulent boundary layer wall pressure. *Journal of sound and Vibration*, 70(1):29–67, 1980.

Christensen, J. and **Hald, J.** Technical review no. 1 2004. *Brüel & Kjaer, ISSN*, pages 0007–2621, 2004.

Corcos, G. M. Resolution of pressure in turbulence. *The Journal of the Acoustical Society of America*, 35(2):192–199, 1963.

Dang, H.-P. *Approches bayésiennes non paramétriques et apprentissage de dictionnaire pour les problèmes inverses en traitement d'image.* PhD thesis, Centrale Lille, 2016.

Dinsenmeyer, A., **Antoni, J.**, **Leclère, Q.**, and **Pereira, A.** On the denoising of cross-spectral matrices for (aero) acoustic applications. In *7th Berlin beamforming conference*, 2018.

Dinsenmeyer, A., **Leclère, Q.**, **Antoni, J.**, and **Julliard, E.** Comparison of microphone array denoising techniques and application to flight test measurements. In *25th AIAA/CEAS Aeroacoustics Conference*, page 2744, 2019.

Dinsenmeyer, A., **Antoni, J.**, **Leclère, Q.**, and **Pereira, A.** A probabilistic approach for cross-spectral matrix denoising: Benchmarking with some recent methods. *The Journal of the Acoustical Society of America*, 147(5):3108–3123, 2020.

Dougherty, R. Cross spectral matrix diagonal optimization. In *6th Berlin Beamforming Conference*, February 2016.

Dougherty, R. P. *Beamforming In Acoustic Testing.* Springer Berlin Heidelberg, 2002.

Dougherty, R. P. Functional beamforming for aeroacoustic source distributions. *AIAA paper*, 3066:2014, 2014.

Druault, P., **Hekmati, A.**, and **Ricot, D.** Discrimination of acoustic and turbulent components from aeroacoustic wall pressure field. *Journal of Sound and Vibration*, 332(26):7257 – 7278, 2013.

Ehrenfried, K. and **Koop, L.** Experimental study of pressure fluctuations beneath a compressible turbulent boundary layer. In *14th AIAA/CEAS Aeroacoustics Conference (29th AIAA Aeroacoustics Conference)*, May 2008. Vancouver.

Ehrenfried, K., **Koop, L.**, **Henning, A.**, and **Kaepernick, K.** Effects of wind-tunnel noise on array measurements in closed test sections. In *Proceedings of BeBeC-2006, Berlin, Germany*, 2006.

Eltoft, T., **Kim, T.**, and **Lee, T.-W.** On the multivariate laplace distribution. *IEEE Signal Processing Letters*, 13(5):300–303, 2006.

Farabee, T. M. and **Casarella, M. J.** Measurements of Fluctuating Wall Pressure for Separated/Reattached Boundary Layer Flows. *Journal of Vibration, Acoustics, Stress, and Reliability in Design*, 108(3):301–307, 07 1986.

Farabee, T. M. and **Casarella, M. J.** Spectral features of wall pressure fluctuations beneath turbulent boundary layers. *Physics of Fluids A: Fluid Dynamics*, 3(10):2410–2420, 1991.

Faure, C. *Approches bayésiennes appliqués à l'identification d'efforts vibratoire par la méthode de Résolution Inverse*. PhD thesis, Ph. D. thesis, Université du Maine, Le Mans, France, 2017.

Fenech, B. A. *Accurate aeroacoustic measurements in closed-section hard-walled wind tunnels*. PhD thesis, University of Southampton, June 2009.

Finez, A., **Pereira, A. A.**, and **Leclère, Q.** Broadband mode decomposition of ducted fan noise using cross-spectral matrix denoising. In *Fan Noise 2015*, Proceedings of Fan Noise 2015, Lyon, France, 2015.

Fleury, V., **Coste, L.**, **Davy, R.**, **Mignosi, A.**, **Cariou, C.**, and **Prosper, J.-M.** Optimization of microphone array wall mountings in closed-section wind tunnels. *AIAA journal*, 50(11):2325–2335, 2012.

Ge, D., **Idier, J.**, and **Le Carpentier, E.** Enhanced sampling schemes for mcmc based blind bernoulli–gaussian deconvolution. *Signal Processing*, 91(4):759–772, 2011.

Gelman, A., **Carlin, J. B.**, **Stern, H. S.**, **Dunson, D. B.**, **Vehtari, A.**, and **Rubin, D. B.** *Bayesian data analysis*. Chapman and Hall/CRC, 2014.

Gerstoft, P., **Menon, R.**, **Hodgkiss, W. S.**, and **Mecklenbräuker, C. F.** Eigenvalues of the sample covariance matrix for a towed array. *The Journal of the Acoustical Society of America*, 132(4):2388–2396, 2012.

Graham, W. R. A comparison of models for the wavenumber–frequency spectrum of turbulent boundary layer pressures. *Journal of sound and vibration*, 206(4): 541–565, 1997.

Grant, M. and **Boyd, S.** Graph implementations for nonsmooth convex programs. In *Recent Advances in Learning and Control*, Lecture Notes in Control and Information Sciences, pages 95 –110. Springer-Verlag Limited, 2008.

Grant, M. and **Boyd, S.** CVX: Matlab software for disciplined convex programming, version 2.1. http://cvxr.com/cvx, March 2014. Last viewed March 31,2020.

Hald, J. Removal of incoherent noise from an averaged cross-spectral matrix. *The Journal of the Acoustical Society of America*, 142(2):846–854, 2017.

Hald, J. Denoising of cross-spectral matrices using canonical coherence. *The Journal of the Acoustical Society of America*, 146(1):399–408, 2019.

Harper-Bourne, M. and **Fisher, M. J. F.** The noise from shock waves in supersonic jets-noise mechanism. In *Agard Conference on Noise Mechanisms*, number 131, 1973.

Haxter, S. and **Spehr, C.** Comparison of model predictions for coherence length to in-flight measurements at cruise conditions. *Journal of Sound and Vibration*, 390:86–117, 2017.

Haxter, S. and **Spehr, C.** Wavenumber characterization of surfacepressure fluctuations on the fuselage duringcruise flight. In *Flinovia-Flow Induced Noise and Vibration Issues and Aspects*. Springer, 2019. (In press).

Helffer, E. From external to internal noise on airbus A350. In *25th International Conference on Sound and Vibrations*, July 2018.

Howe, M. Surface pressures and sound produced by turbulent flow over smooth and rough walls. *The Journal of the Acoustical Society of America*, 90(2):1041–1047, 1991.

Huang, X., **Bai, L.**, **Vinogradov, I.**, and **Peers, E.** Adaptive beamforming for array signal processing in aeroacoustic measurements. *The Journal of the Acoustical Society of America*, 131(3):2152–2161, 2012.

Huber, J., **Britchford, K.**, **Laurendeau, E.**, **Fleury, V.**, **Bulté, J.**, **Sylla, A.**, and **Long, D.** Understanding and reduction of cruise jet noise at model and full scale. In *15th AIAA/CEAS Aeroacoustics Conference (30th AIAA Aeroacoustics Conference)*, page 3382, 2009.

Hwang, Y. F., **Bonness, W. K.**, and **Hambric, S. A.** Comparison of semi-empirical models for turbulent boundary layer wall pressure spectra. *Journal of Sound and Vibration*, 319(1-2):199–217, 2009.

Hwang, Y., **Bonness, W.**, and **Hambric, S.** On modeling structural excitations by low speed turbulent boundary layer flows. Technical report, Pennsylvania State Univ State College Applied Reserach Lab, 2003.

Jaeger, S., **Horne, W.**, and **Allen, C.** Effect of surface treatment on array microphone self-noise. In *6th AIAA/CEAS Aeroacoustics Conference*, page 1937, 2000.

Jiang, G., **Sun, C.**, and **Liu, X.** Diagonal denoising for conventional beamforming via sparsity optimization. *IEEE Access*, 8:11416–11425, 2020.

Jolliffe, I. T. *Principal Component Analysis*, volume 2nd ed. New York: Springer-Verlag, 2002.

Ko, S. H. and **Schloemer, H. H.** Flow noise reduction techniques for a planar array of hydrophones. *The Journal of the Acoustical Society of America*, 90(4): 2285–2285, 1991.

Koop, L. and **Ehrenfried, K.** Microphone-array processing for wind-tunnel measurements with strong background noise. In *14th AIAA/CEAS Aeroacoustics Conference (29th AIAA Aeroacoustics Conference)*, page 2907, 2008.

Leclère, Q., **Aujogue, N.**, **Dinsenmeyer, A.**, **Antoni, J.**, and **Julliard, E.** Characterization of engine jet noise in flight conditions using advanced acoustic imaging methods. In *8th Berlin beamforming conference*, 2020.

Leclère, Q., **Totaro, N.**, **Pézerat, C.**, **Chevillotte, F.**, and **Souchotte, P.** Extraction of the acoustic part of a turbulent boundary layer from wall pressure and vibration measurements. In *Proceedings of the International Congress on Noise and Vibration Emerging Methods*, page 49046, April 2015.

Leclère, Q., **Dinsenmeyer, A.**, **Salze, E.**, and **Antoni, J.** A comparison between different wall pressure measurement devices for the separation and analysis of TBL and acoustic contributions. In *Flinovia-Flow Induced Noise and Vibration Issues and Aspects*. Springer, 2021. (In press).

Lecoq, D., **Pézerat, C.**, **Thomas, J.-H.**, and **Bi, W.** Extraction of the acoustic component of a turbulent flow exciting a plate by inverting the vibration problem. *Journal of Sound and Vibration*, 333(12):2505 – 2519, 2014.

Lee, J. B., **Woodyatt, A. S.**, and **Berman, M.** Enhancement of high spectral resolution remote-sensing data by a noise-adjusted principal components transform. *IEEE Transactions on Geoscience and Remote Sensing*, 28(3):295–304, 1990.

Long, D. Acoustic source location in wind tunnel tests via subspace beamforming. In *41st Aerospace Sciences Meeting and Exhibit*, page 369, 2003.

Lopes, H. F. and **West, M.** Bayesian model assessment in factor analysis. *Statistica Sinica*, pages 41–67, 2004.

Lu, H. An empirical model for prediction of coaxial jet noise in ambient flow. In *10th Aeroacoustics Conference*, page 1912, 1986.

Marčenko, V. and **Pastur, L.** Distributions of eigenvalues of some sets of random matrices. *Math. USSR-Sb*, 1:507–536, 1967.

Maury, C., **Gardonio, P.**, and **Elliott, S.** A wavenumber approach to modelling the response of a randomly excited panel, part II: Application to aircraft panels excited by a turbulent boundary layer. *Journal of Sound and Vibration*, 252(1): 115–139, 2002.

McLachlan, G. J. and **Krishnan, T.** *The EM algorithm and extensions*, volume 382. John Wiley & Sons, 2007.

Mehta, R. and **Rana, K.** A review on matrix factorization techniques in recommender systems. In *2017 2nd International Conference on Communication Systems, Computing and IT Applications (CSCITA)*, pages 269–274. IEEE, 2017.

Mellen, R. H. On modeling convective turbulence. *The journal of the Acoustical Society of America*, 88(6):2891–2893, 1990.

Merino-Martínez, R., **Snellen, M.**, and **Simons, D. G.** Functional beamforming applied to imaging of flyover noise on landing aircraft. *Journal of Aircraft*, 53 (6):1830–1843, 2016.

Minka, T. P. Automatic choice of dimensionality for pca. In *Advances in neural information processing systems*, pages 598–604, 2001.

Mueller, T. J. *Aeroacoustic measurements*. Springer, 2002.

Neal, R. M. Mcmc using hamiltonian dynamics. In *Handbook of Markov Chain Monte Carlo*, pages 383–397. Chapman and Hall/CRC, 2011.

Palumbo, D. Determining correlation and coherence lengths in turbulent boundary layer flight data. *Journal of Sound and Vibration*, 331(16):3721–3737, 2012.

Park, T. and **Van Dyk, D. A.** Partially collapsed gibbs samplers: Illustrations and applications. *Journal of Computational and Graphical Statistics*, 18(2): 283–305, 2009.

Petersen, K. B. and **Pedersen, M. S.** The matrix cookbook, 2008. version: November 15, 2012, http://www.math.uwaterloo.ca/~hwolkowi/matrixcookbook.pdf (last viewed 3/31/2020).

Pisarenko, V. F. The retrieval of harmonics from a covariance function. *Geophysical Journal International*, 33(3):347–366, 1973.

Preacher, K. J., **Zhang, G.**, **Kim, C.**, and **Mels, G.** Choosing the optimal number of factors in exploratory factor analysis: A model selection perspective. *Multivariate Behavioral Research*, 48(1):28–56, 2013.

Prigent, S. L., **Salze, É.**, and **Bailly, C.** Deconvolution of wave-number-frequency spectra of wall pressure fluctuations. *AIAA Journal*, 58(1):164–173, 2019.

Roberts, G. O. and **Rosenthal, J. S.** Optimal scaling of discrete approximations to langevin diffusions. *Journal of The Royal Statistical Society Series B-statistical Methodology*, 60:255–268, 1998.

Sarradj, E. A fast signal subspace approach for the determination of absolute levels from phased microphone array measurements. *Journal of Sound and Vibration*, 329(9):1553–1569, 2010.

Sarradj, E., **Herold, G.**, **Sijtsma, P.**, **Merino-Martinez, R.**, **Malgoezar, A.**, **Snellen, M.**, **Geyer, T.**, **Bahr, C.**, **Porteous, R.**, **Moreau, D.**, and **Doolan, C.** A microphone array method benchmarking exercise using synthesized input data. In *23rd AIAA/CEAS Aeroacoustics Conference*, June 2017.

Schloemer, H. H. Effects of pressure gradients on turbulent boundary-layer wall-pressure fluctuations. *The Journal of the Acoustical Society of America*, 40 (5):1254–1254, 1966.

Schmidt, R. . Multiple emitter location and signal parameter estimation. *IEEE Transactions on antennas and propagation*, AP-34(3): p. 276–280, 1986.

Sijtsma, P. Experimental techniques for identification and characterisation of noise sources. In *Advances in Aeronautics & Applications, VKI Lecture Series*. National Aerospace Laboratory NLR, 2004.

Sijtsma, P. Clean based on spatial source coherence. *International journal of aeroacoustics*, 6(4):357–374, 2007.

Sijtsma, P., **Dinsenmeyer, A.**, **Antoni, J.**, and **Leclère, Q.** Beamforming and other methods for denoising microphone array data. In *25th AIAA/CEAS Aeroacoustics Conference*, page 2653, 2019.

Singer, B. A. Turbulent wall-pressure fluctuations: New model for off-axis cross-spectral density. *NASA Contractor Report 198297*, 1996.

Smith, M. J. T. *Aircraft noise*. Cambridge University Press, 1989.

Smol'Yakov, A., **Tkachenko, V.**, and **Wood, J.** Model of a field of pseudosonic turbulent wall pressures and experimental data. *Soviet physics. Acoustics*, 37(6): 627–631, 1991.

Sobral, A. LRSLibrary. https://github.com/andrewssobral/lrslibrary/. Last viewed March 31, 2020.

Sobral, A., **Bouwmans, T.**, and **Zahzah, E.-h.** LRSLibrary: Low-rank and sparse tools for background modeling and subtraction in videos. In *Robust Low-Rank and Sparse Matrix Decomposition: Applications in Image and Video Processing*. CRC Press, Taylor and Francis Group., 2015.

Starck, J.-L., **Murtagh, F.**, and **Fadili, J. M.** *Sparse image and signal processing: wavelets, curvelets, morphological diversity*. Cambridge university press, 2010.

Suzuki, T. Generalized inverse beam-forming algorithm resolving coherent/incoherent, distributed and multipole sources. *Journal of Sound and Vibration*, 330:5835–5851, November 2011.

Tam, C. K. W. Supersonic jet noise. *Annual Review of Fluid Mechanics*, 27(1): 17–43, 1995.

Tam, C. K., **Pastouchenko, N. N.**, and **Viswanathan, K.** Broadband shock-cell noise from dual stream jets. *Journal of Sound and Vibration*, 324(3-5):861–891, 2009.

Tipping, M. E. and **Bishop, C. M.** Probabilistic principal component analysis. *Journal of the Royal Statistical Society: Series B (Statistical Methodology)*, 61(3): 611–622, 1999.

Tütüncü, R. H., **Toh, K.-C.**, and **Todd, M. J.** Solving semidefinite-quadratic-linear programs using sdpt3. *Mathematical programming*, 95(2):189–217, 2003.

van Dyk, D. A. and **Park, T.** Partially collapsed gibbs sampling and path-adaptive metropolis-hastings in high-energy astrophysics. In *Handbook of Markov Chain Monte Carlo*, pages 383–397. Chapman and Hall/CRC, 2011.

Veit, T., **Idier, J.**, and **Moussaoui, S.** Rééchantillonnage de l'échelle dans les algorithmes mcmc pour les problèmes inverses bilinéaires. *Traitement du Signal*, 25(4/5):3–34329, 2008.

Wang, H. and **Kaveh, M.** Coherent signal-subspace processing for the detection and estimation of angles of arrival of multiple wide-band sources. *IEEE Transactions on Acoustics, Speech, and Signal Processing*, 33(4):823–831, 1985.

Wax, M. and **Kailath, T.** Detection of signals by information theoretic criteria. *IEEE Transactions on Acoustics, Speech, and Signal Processing*, 33(2):387–392, 1985.

Welch, P. The use of fast fourier transform for the estimation of power spectra: a method based on time averaging over short, modified periodograms. *IEEE Transactions on audio and electroacoustics*, 15(2):70–73, 1967.

Witten, D. M., **Tibshirani, R.**, and **Hastie, T. J.** A penalized matrix decomposition, with applications to sparse principal components and canonical correlation analysis. *Biostatistics*, 10 3:515–34, 2009.

Wright, J., **Ganesh, A.**, **Rao, S.**, and **Ma, Y.** Robust principal component analysis: Exact recovery of corrupted low-rank matrices, 2009. arXiv:0905.0233.

Xia, H.-J., **Ma, Y.-L.**, and **Liu, Y.-X.** Principle and application of diagonal reducing method in the complex noise fields. *Acta physica sinica*, 66(1):014304, 2017.

Zhou, M., **Chen, H.**, **Paisley, J.**, **Ren, L.**, **Li, L.**, **Xing, Z.**, **Dunson, D.**, **Sapiro, G.**, and **Carin, L.** Nonparametric bayesian dictionary learning for analysis of noisy and incomplete images. *IEEE Transactions on Image Processing*, 21(1):130–144, 2011.

Zou, H. and **Xue, L.** A selective overview of sparse principal component analysis. *Proceedings of the IEEE*, 106:1311–1320, 2018.

List of Figures

Probabilistic approach for the separation of the acoustic and aerodynamic wall pressure fluctuations

Abstract

With the emergence of MEMS and the overall decrease in the cost of sensors, the acquisitions multichannel are becoming more widespread, particularly in the field of acoustic source identification. The quality of source localization and quantification can be degraded by the presence of ambient or electronic noise. In particular, in the case of in flow measurements, the turbulent boundary layer that develops over the measuring system can induce pressure fluctuations that are much greater than those of acoustic sources. It then becomes necessary to process the acquisitions to extract each component of the measured field. For this purpose, it is proposed in this thesis to decompose the measured spectral matrix into the sum of a matrix associated with the acoustic contribution and a matrix for aerodynamic noise. This decomposition exploits the statistical properties of each pressure field. Assuming that the acoustic contribution is highly correlated on the sensors, the rank of the corresponding cross-spectral matrix is limited to the number of equivalent uncorrelated sources. Concerning the aerodynamic noise matrix, two statistical models are proposed. A first model assumes a totally uncorrelated field on the sensors, and a second is based on a pre-existing physical model. This separation problem is solved by a Bayesian optimization approach, which takes into account the uncertainties on each component of the model. The performance of this method is first evaluated on wind tunnel measurements and then on particularly noisy industrial measurement, coming from microphones flushmounted on the fuselage of an inflight large aircraft.

Approche probabiliste pour la séparation des composantes acoustique et aérodynamique dans les champs de pression pariétale

Résumé

Avec l'apparition des MEMS et la diminution globale du coût des capteurs, les acquisitions multivoies se généralisent, notamment dans le domaine de l'identification de sources acoustiques. La qualité de la localisation et de la quantification des sources peut être dégradée par la présence de bruit de mesure ambiant ou induit par le système d'acquisition. En particulier, dans le cas de mesures en présence d'un écoulement, la couche limite turbulente qui se développe sur le système de mesure peut induire des fluctuations de pression de niveau bien supérieur à celles des sources acoustiques. Il devient alors nécessaire de traiter les acquisitions pour extraire chaque composante du champ mesuré. Pour cela, on propose de décomposer la matrice spectrale mesurée en la somme d'une matrice associée à la contribution acoustique et d'une matrice pour le bruit aérodynamique. Cette décomposition exploite les propriétés statistiques de chaque champ de pression. En supposant que la contribution acoustique est fortement corrélée sur les capteurs, le rang de la matrice interspectrale associée se limite au nombre de sources décorrélées équivalentes. Concernant la matrice du bruit aérodynamique, deux modèles statistiques sont proposés. Un premier modèle fait l'hypothèse d'un champ totalement décorrélé sur les capteurs, et un second repose sur un modèle physique préexistant. Ce problème de séparation est résolu par une approche d'optimisation bayésienne, qui permet de prendre en compte les incertitudes sur chaque composante du modèle. Les performances de cette méthode sont d'abord évaluées sur des mesures en soufflerie puis sur des données industrielles particulièrement bruitées, provenant de mesures microphoniques effectuées sur le fuselage d'un avion de ligne en vol.

UNIVERSITÉ DE LYON

INSA

FOLIO ADMINISTRATIF

THÈSE DE L'UNIVERSITÉ DE LYON OPÉRÉE AU SEIN DE L'INSA LYON

NOM : Dinsenmeyer

DATE de SOUTENANCE : 12/10/2020

Prénoms : Alice

TITRE : Probabilistic approach for the separation of the acoustic and aerodynamic wall pressure fluctuations

NATURE : Doctorat

Numéro d'ordre : 2020LYSEI087

École doctorale : Mécanique, énergétique, Génie Civil, Acoustique (MEGA)

Spécialité :Acoustique

RÉSUMÉ :
Avec l'apparition des MEMS et la diminution globale du coût des capteurs, les acquisitions multivoies se généralisent, notamment dans le domaine de l'identification de sources acoustiques. La qualité de la localisation et de la quantification des sources peut être dégradée par la présence de bruit de mesure ambiant ou induit par le système d'acquisition. En particulier, dans le cas de mesures en présence d'un écoulement, la couche limite turbulente qui se développe sur le système de mesure peut induire des fluctuations de pression de niveau bien supérieur à celles des sources acoustiques. Il devient alors nécessaire de traiter les acquisitions pour extraire chaque composante du champ mesuré. Pour cela, on propose de décomposer la matrice spectrale mesurée en la somme d'une matrice associée à la contribution acoustique et d'une matrice pour le bruit aérodynamique. Cette décomposition exploite les propriétés statistiques de ces deux matrices. En supposant que la contribution acoustique est fortement corrélée sur les capteurs, le rang de la matrice spectrale associée se limite au nombre de sources décorrélées équivalentes. Concernant la matrice du bruit aérodynamique, deux modèles statistiques sont proposés. Un premier modèle fait l'hypothèse d'un champ totalement décorrélé sur les capteurs, et un second repose sur un modèle physique pré-existant. Ce problème de séparation est résolu par une approche d'optimisation bayésienne, qui permet de prendre en compte les incertitudes sur chaque composante du modèle. Les performances de cette méthode sont d'abord évaluées sur des mesures en soufflerie puis sur des données industrielles particulièrement bruitées, provenant de mesures microphoniques effectuées sur le fuselage d'un avion de ligne en vol.

MOTS-CLÉS :
Problème inverse, Couche limite turbulente, Inférence bayésienne, Matrice de covariance structurée, Méthode de Monte-Carlo par chaînes de Markov, Mesures en soufflerie, Mesures en vol.

Laboratoire (s) de recherche : Laboratoire de vibration et acoustique (LVA) et Laboratoire de Mécanique des Fluide et d'Acoustique (LMFA)

Directeur de thèse: Jérôme Antoni

Président de jury :

Composition du jury :
Valeau, Vincent (rapporteur), Pézerat, Charles (rapporteur), Lopez Arteaga, Ines (examinatrice), Piot, Estelle (Examinatrice), Gabart, Gwénaël (examinateur), Antoni, Jérôme (directeur de thèse), Bailly, Christophe (co-encadrant), Leclère, Quentin (co-encadrant), Julliard, Emmanuel (invité), Sijtsma, Pieter (invité), Picard, Christophe (invité).